Characterizing mass transport in hydrogels using Nuclear Magnetic Resonance

Malgorzata Anna Wisniewska-Dale

Thesis for the degree of Philosophiae Doctor (PhD)
University of Bergen, Norway
2019

UNIVERSITY OF BERGEN

Characterizing mass transport in hydrogels using Nuclear Magnetic Resonance

Malgorzata Anna Wisniewska-Dale

Thesis for the degree of Philosophiae Doctor (PhD)
at the University of Bergen

Date of defense: 08.11.2019

Year: 2019

Title: Characterizing mass transport in hydrogels using Nuclear Magnetic Resonance

Name: Malgorzata Anna Wisniewska-Dale

Print: Skipnes Kommunikasjon / University of Bergen

Preface

This dissertation is submitted as part of fulfillment for the degree of Philosophiae Doctor at the University of Bergen. The research presented in this dissertation has been conducted at the Department of Chemistry at the University of Bergen, in the period 2015-2019, under the supervision of Associate Professor John Georg Seland and the co-supervision of Associate Professor Kristine Spildo.

The main focus of this thesis has been to study the mass transport properties of hydrogels using Nuclear Magnetic Resonance (NMR) spectroscopy and Magnetic Resonance Imaging (MRI). This thesis is divided into two parts. The first part consists of an introduction outlining the background for the project as well as the aims, and chapters summarizing theoretical aspects of hydrogels (Chapter 2), NMR (Chapter 3), and diffusion (Chapter 4). Chapter 5 gives a description of the materials and main experimental techniques used in this project. Main results are summarized in Chapter 6. The thesis proceeds with concluding remarks (Chapter 7). The second part of this dissertation consists of three research papers included at the end of the thesis.

Acknowledgment

I wish to express my sincere gratitude to my supervisor **John Georg Seland** for introducing me to the exciting field of NMR. Thank you for your patience, motivation and support during my PhD study. Thank you for encouraging me to attend the ENC conference.

I would also like to thank my co-supervisor **Kristine Spildo** for encouraging my research. Kristine supported me not only by providing valuable insight into this project but also academically and emotionally through the rough road to finish this thesis.

Through these years I was proud to be a member of the NMR group at the Department of Chemistry. **Olav-Audun Bjørkelund** deserves my special thanks for helping me with the diffusion probe and for keeping up the spirit.

I would like to thank my colleagues at the Department of Chemistry. **Reidun Myklebust** and **Marit Bøe Vaage** - it was a pleasure working with you on the lab courses.

Last but not least, I would like to thank **Louise Bergsjø** and **Eirin Alme** with whom I was lucky to share office.

List of papers

1. Malgorzata Anna Wisniewska, John Georg Seland, Wei Wang, *Determining the scaling of gel mesh size with changing crosslinker concentration using dynamic swelling, rheometry, and PGSE NMR spectroscopy*, Journal of Applied Polymer Science **135**, 45, 2018, 46695.

2. Malgorzata Anna Wisniewska, John Georg Seland, *Investigating structure-dependent diffusion in hydrogels using spatially resolved NMR spectroscopy*, Journal of Colloid and Interface Science **533**, 2019, 671.

3. Malgorzata Anna Wisniewska, Kristine Spildo, John Georg Seland, *MRI and MRS study of poly(N-isopopylacrylamide) hydrogel volume phase transition and release of β-cyclodextrins*, Manuscript.

Abbreviations

AAc	Acrylic Acid
APS	Ammonium Persulfate
βCD	β-Cyclodextrin
CD	Cyclodextrin
CMC	Critical Micelle Concentration
CSI	Chemical Shift Imaging
DAT	*N,N'*-Diallyl L-tartardiamide
DDS	Drug Delivery System
DTI	Diffusion Tensor Imaging
EPI	Echo Planar Imaging
FID	Free Induction Decay
FOV	Field of View
FT	Fourier Transform
LCST	Lower Critical Solution Temperature
MRI	Magnetic Resonance Imaging
MSD	Mean-Squared Displacement
NIPAM	*N*-isopropylacrylamide
NMR	Nuclear Magnetic Resonance
P(NIPAM-co-AAc)	Poly(*N*-isopropylacrylamide-*co*-acrylic acid)
PFG	Pulsed Field Gradient
PFGSE	Pulsed Field Gradient Spin Echo
PFGSTE	Pulsed Field Gradient Stimulated Echo
P(NIPAM)	Poly(*N*-isopropylacrylamide)
RF	Radio Frequency
STEAM	STimulated Echo Acquisition Mode
TE	Echo Time (in MRI)
TEMED	*N,N,N',N'*-Tetramethylethylenediamine
TR	Repetition Time (in MRI)
VOI	Volume of Interest
VPT	Volume Phase Transition
VPTT	Volume Phase Transition Temperature

Greek symbols

α	linear expansion factor of the hydrogel network (in Equation 2.9)
α	time-independent scaling constant (in Equation 4.9)
γ	gyromagnetic ratio
ΔG_{total}	Gibbs free energy
ΔG_{mixing}	Gibbs free energy of mixing
$\Delta G_{elastic}$	Gibbs free energy of elastic deformation
$\Delta\mu_{total}$	chemical potential
ΔH_{mixing}	enthalpy of mixing
ΔS_{mixing}	entropy of mixing
Δ	diffusion time
δ	chemical shift (in Equation 3.16)
δ	gradient pulse length
∇c	concentration gradient
∇^2	Laplace operator
ζ	restriction effect
η	solvent viscosity
λ	boundary condition parameter
μ_1	chemical potential of the solvent in the hydrogel
$\mu_{1,0}$	chemical potential of the pure solvent
$\vec{\mu}$	magnetic moment
ν_1	volume fraction of water
ν_{2s}	volume fraction of the polymer
ν_{ref}	frequency of the reference peak
ξ	mesh size of the hydrogel
ρ	polymer density
ρ_{pol}	density of the hydrogel
ρ_{solv}	density of the solvent
σ	shielding constant
θ	rotation angle
τ	time interval following the RF pulse

χ	polymer-solvent interaction parameter
Ω	offset in the rotating frame
$\vec{\omega}_L$	Larmor frequency
$\vec{\omega}$	angular frequency
ω_z	spatially dependent Larmor frequency

Latin symbols

A	structure factor (type of polymer network)
A_0	integration constant in Equation 3.13
a	sphere radius
$\vec{B}_0$	static magnetic field
B_{local}	local magnetic field
$\vec{B}_1$	magnetic part of the electromagnetic radiation pulse
B_z	magnetic field along the z-axis
BW	pulse bandwidth
b	diffusion weighing factor
C_{cl}	crosslinker concentration
C_p	polymer concentration
C^*	overlapping concentration
D_s	self-diffusion coefficient
D_0	self-diffusion coefficient at infinite dilution
D_m	mutual diffusion coefficient
D_s^{gel}	self-diffusion coefficient of solute in the hydrogel
D_s^0	self-diffusion coefficient of solute in solution
d_w	random walk dimension
E	echo intensity
f	functionality of the crosslinks
f	friction coefficient (in Equations 2.17 and 4.1)
G	magnetic field gradient
G_z	magnetic field gradient pulse applied in the z-direction
G_x	frequency-encoding gradient

G_y	phase-encoding gradient
G'	elastic modulus
$\mathbf{J}(\mathbf{r},t)$	flux of a particle
k_B	Boltzmann constant
l	bond length along the polymer backbone
L	sample or RF coil length
M_c	number average chain molecular weight
M_n	number average molecular weight before crosslinking
$\vec{M}$	magnetization vector
M_0	magnetization at thermal equilibrium
Q_m	mass swelling ratio
V_1	molar volume of the solvent
M_r	molecular weight of the repeat monomer units
v_e	number of effective polymer chains
n_2	number of free polymer molecules
n_1	number of water molecules in the swollen gel
$P(\mathbf{r}_0,\mathbf{r}_1,t)$	diffusion propagator
$\mathbf{r}$	position vector
r_0	position at t_0
r_1	position after time t
R	gass constant
R_h	hydrodynamic radius
$\langle R^2 \rangle$	mean-squared displacement
$\sqrt{\langle \bar{r_0}^2 \rangle}$	root-mean-square end-to-end distance of the polymer chains between crosslinks in an unperturbed state
S_z	signal resulting from the slice-selective experiment
S_0	signal in the absence of spatial selection
$\bar{v}$	specific volume of the polymer
t_p	duration of the RF field pulse
t_E	echo time
t	time
t_d	diffusion time

T_1	spin-lattice relaxation time
T_2	transverse relaxation time
$T_2^\star$	apparent transverse relaxation time
$T_2^\dagger$	inhomogeneous contributions to transverse magnetization
T	temperature
v	Flory exponent
V_0	volume of the unswolen polymer
W_s	weight of the swollen hydrogel
W_d	weight of the dry hydrogel

Contents

Chapter 1

Introduction

During the past six decades, drug delivery has become a major research topic in the pharmaceutical field. Conventionally, the therapeutic concentration of a drug in the blood is achieved by repeated administrations in the form of pills or injections. This strategy leads to an unstable drug concentration in the blood as it peaks shortly after the administration and rapidly declines afterwards. A Drug Delivery System (DDS) delivers a pharmaceutical compound in a controlled manner with respect to time period and release rate, and maintains the drug level in the organism within the therapeutic window (Figure 1.1) [1, 2].

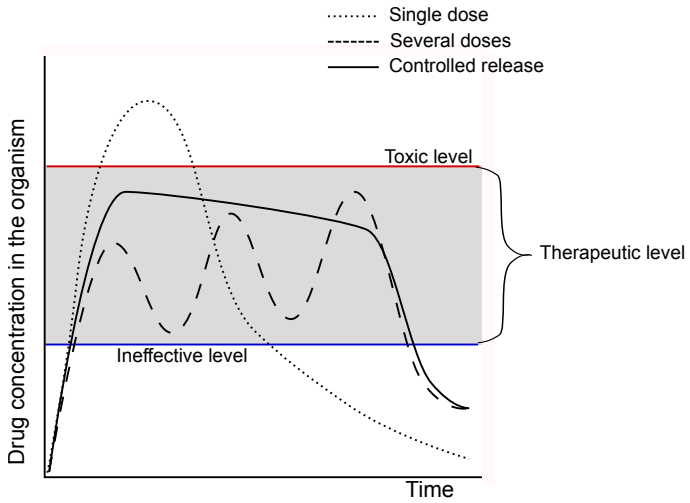

Figure 1.1: A schematic illustration of the drug concentration in the organism when using different administration methods. Single dose of a drug in a form of a pill leads to the abrupt rise of the drug concentration above the toxic level. After a short period of time, the drug concentration drops below the effective level. Periodic dosages can cause the drug concentration to go above the toxic level and below the effective level. Adapted from [2].

Hydrogels have drawn widespread interest as potential candidates for applications in areas such as DDS, tissue engineering scaffolds, contact lenses and wound dressings, owing to their adjustable porous structure [3, 4]. Ideally, the release of a drug from a DDS should be correlated with changes in physiological environment such as pH or temperature [5]. A prominent example of such stimuli-responsive DDS are hydrogels composed of Poly(*N*-isopropylacrylamide) (P(NIPAM)), which show a reversible phase transition at temperatures above 34° C at which the hydrogel network collapses [6, 7]. Stimuli-responsive hydrogels may be combined with a vehicle such as surfactant micelles or cyclodextrins (CD) that allow the inclusion of hydrophobic drugs [8].

Due to their non-invasive character, Nuclear Magnetic Resonance (NMR) spectroscopy and Magnetic Resonance Imaging (MRI) techniques have been increasingly used to study DDS by monitoring swelling and molecular mass transport in the form of molecular diffusion and flow [9–11]. NMR has proven to be useful in characterizing the molecular dynamics of hydrogels through measurements of longitudinal (T_1) and transverse (T_2) relaxation times, as well as self-diffusion coefficients (D_s) [12–14]. In addition, MRI methods are commonly used in the study of the ingress of water into solid oral dosage forms, such as tablets and capsules, and the subsequent hydration, swelling and erosion of such polymer matrices [9, 10].

Conventionally, the analysis of DDS is usually performed by a combination of gravimetric studies of water uptake and the kinetics of drug release measured using ultraviolet–visible spectroscopy [15]. However, such studies do not provide information about the distribution of the diffusing drug in the sample, or the mobility of the drug and solvent prior to and during the drug release. In addition to providing the same information as that obtained using conventional methods, NMR and MRI methods give insight into local transport processes during drug release in one experimental procedure [16].
The aims of this dissertation were as follows:

1. To establish a reliable methodology for determining the structural properties of hydrogels.

2. To investigate the effect of hydrogel structural properties on diffusional processes in the model DDS.

3. To examine how NMR and MRI techniques can be used in order to improve existing experimental procedures to characterize drug release from hydrogels.

[Introduction]

Chapter 2

Hydrogels

Since the pioneering work of Wichterle and Lim published in Nature in 1960 [17], the fields of drug delivery and hydrogels have evolved significantly. The highly porous structure makes hydrogels an ideal DDS, as it allows loading of drugs into the hydrogel and subsequent controlled release. Thus, local drug concentration is maintained through the whole release time. Hydrogels are three-dimensional crosslinked networks composed of hydrophilic polymer which are biocompatible due to the capability to absorb large amount of water (up to 99% of total weight). On the other hand, hydrogels are insoluble in water as their network structure is maintained by crosslinks. There are two main categories of crosslinks: chemical and physical. Chemical crosslinking results from the formation of covalent bonds between polymer chains, and produces permanent hydrogels. Typically, chemical crosslinking methods involve addition of small molecules that form chemical bonds between polymer chains [18, 19]. Physical crosslinking is a result of intermolecular reversible interactions between polymer chains, such as ionic interactions, polymerized entanglements or hydrogen bonds [19, 20]. The main types of crosslinks are presented in Figure 2.1. The crosslinking method plays a large role in determining the hydrogel's network structure, which in turn plays a critical factor in controlling the rate of the drug release from hydrogels. In this study, only free radical polymerization is used to prepare hydrogels.

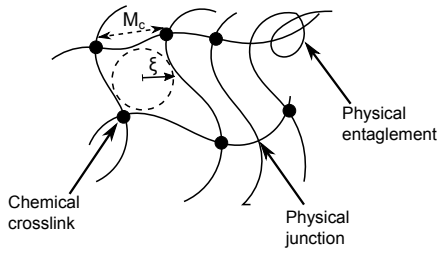

Figure 2.1: Schematic structure of the hydrogel polymer network. Mesh size, ξ and the average molecular weight between the crosslinking points, M_c are defined. Adapted from [19].

As shown in Figure 2.2, hydrogels can be classified in terms of the physical properties, ionic charges, methods of preparation, rate of biodegradation, and crosslinking methods [21].

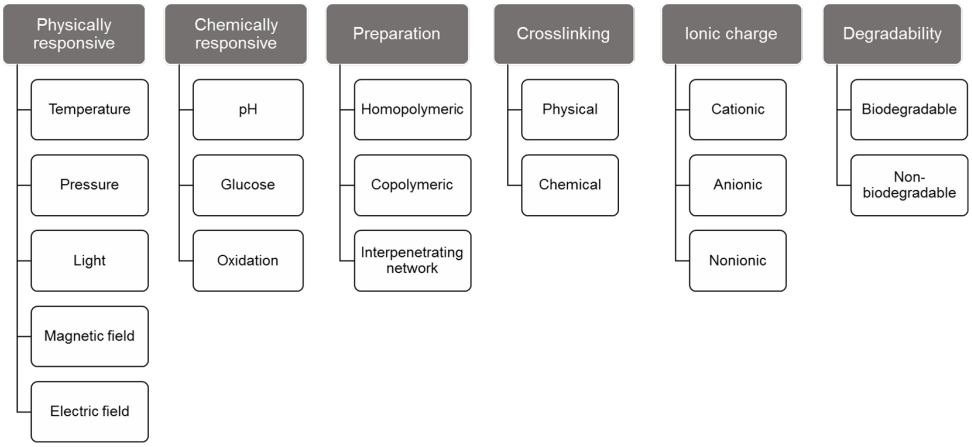

Figure 2.2: Classification of hydrogels based on the different properties. Adapted from [21].

Figure 2.3 presents the monomers used in this work. The composition of the hydrogel can affect bioadhesion, an important feature of adhering to biological surfaces, which has to be taken into account while designing a drug delivery system. Bioadhesion can be used as a method of targeting drugs to a specific site, and it allows longer residence times on the application site [22]. Neutral hydrogels, as those prepared from polymerized *N*-isopropylacrylamide (NIPAM) (Figure 2.3), are nonadhesive to cells and proteins. The addition of an ionic polymer, such as polymerized Acrylic Acid (AAc) containing carboxyl or hydroxyl groups (Figure 2.3) can promote bioadhesion [3].

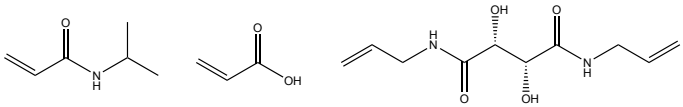

Figure 2.3: Structure of the monomers, *N*-isopropylacrylamide (NIPAM) and Acrylic Acid (AAc), and crosslinker, *N,N'*-Diallyl L-tartardiamide (DAT), used for the synthesis of the P(NIPAM)-based hydrogels.

Loading and releasing of the hydrophobic drugs into hydrogels is rather inefficient. Thus, the use of hydrogels is limited to delivery of the hydrophilic drugs. Strategies to improve the delivery of the hydrophobic drugs by means of hydrogels are proposed in Section 2.2.

2.1 Properties of hydrogels

2.1.1 Swelling theory

For nonionic hydrogels, polymer chains are constrained by crosslinks that serve as elastic junctions. According to the Flory-Rehner theory, when a nonionic hydrogel is placed in an excess solvent, the polymer chains begin to absorb solvent and swell. This thermodynamic force of mixing is opposed by a retractive force of the polymer chains [23]. When these two forces are equal, a state of equilibrium is reached. Equation 2.1 describes this physical situation in terms of the Gibbs free energy (ΔG_{total}):

$$\Delta G_{total} = \Delta G_{mixing} + \Delta G_{elastic} \tag{2.1}$$

Here, ΔG_{mixing} represents the change in free energy due to polymer mixing between the solvent and the polymer chains, which is a measure of the compatibility of the polymer with the solvent molecules [3]. $\Delta G_{elastic}$ is the change in free energy due to elastically effective crosslinks in the hydrogel network.

Equation 2.1 can be differentiated with respect to the number of solvent molecules, keeping temperature and pressure constant. The corresponding change of the chemical potential ($\Delta\mu_{total}$) is then:

$$\Delta\mu_{total} = \Delta\mu_{mixing} + \Delta\mu_{elastic} = \mu_1 - \mu_{1,0} \tag{2.2}$$

Where μ_1 is the chemical potential of the solvent in the hydrogel, and $\mu_{1,0}$ is the chemical potential of the pure solvent (outside the hydrogel) [3, 24]. When the hydrogel is in equilibrium with solvent, $\mu_1 = \mu_{1,0}$. Thus, $\Delta\mu_{mixing}$ and $\Delta\mu_{elastic}$ must balance each other.

ΔG_{mixing} from Equation 2.1 can be expressed using the enthalpy of mixing (ΔH_{mixing}) and the entropy of mixing (ΔS_{mixing}) :

$$\Delta G_{mixing} = \Delta H_{mixing} - T\Delta S_{mixing} \tag{2.3}$$

Where T is the temperature. Furthermore, the ΔH_{mixing} term is:

$$\Delta H_{mixing} = k_B T n_1 \chi \nu_{2s} \tag{2.4}$$

Where k_B is the Boltzmann constant, n_1 is the number of water molecules in the swollen gel, χ is the polymer-solvent interaction parameter, and ν_{2s} is the polymer volume fraction in the swollen gel. The ΔS_{mixing} term is:

$$\Delta S_{mixing} = -k_B(n_1 ln\nu_1 + n_2 ln\nu_{2s}) \tag{2.5}$$

Where ν_1 is the volume fraction of water and n_2 is the number of free polymer molecules. Assuming that $n_2 = 0$, the ΔG_{mixing} becomes:

$$\Delta G_{mixing} = k_B T(n_1 ln\nu_1 + \chi n_1 ln\nu_{2s}) \tag{2.6}$$

The differentiation of ΔG_{mixing} with respect to the number of solvent molecules leads to:

$$\Delta\mu_{mixing} = k_B T \times [ln(1-\nu_{2s}) + \nu_{2s} + \chi + \nu_{2s}^2] \tag{2.7}$$

The chemical potential difference per mole is obtained by multiplying Equation 2.7 with Avogadro's constant:

$$\Delta\mu_{mixing} = RT \times [ln(1-\nu_{2s}) + \nu_{2s} + \chi + \nu_{2s}^2] \tag{2.8}$$

The change of chemical potential due to the elastic retractive forces of the polymer chains can be determined from the theory of rubber elasticity [3, 25, 26]. $\Delta G_{elastic}$ depends on the number

of effective chains (excluding free ends), v_e and the linear expansion factor of the network, α:

$$\Delta G_{elastic} = \frac{RTv_e}{2} \times (3\alpha^2 - 3 - ln\alpha^3) \tag{2.9}$$

The corresponding change of chemical potential due to the elastic retractive force is:

$$\Delta\mu_{elastic} = (\frac{\partial G_{elastic}}{\partial n_1})_{T,P} = RTV_1 \frac{v_e}{V_0} \times (v_{2s}^{\frac{1}{3}} - \frac{v_{2s}}{2}) \tag{2.10}$$

V_0 represents the volume of the unswollen polymer and V_1 the molar volume of the solvent. The total change of the chemical potential is the sum of two contributions and when the state of equilibrium swelling is reached, it equals zero:

$$\Delta\mu = \Delta\mu_{mixing} + \Delta\mu_{elastic} = 0 \tag{2.11}$$

Based on the condition expressed in Equation 2.11 Flory derived a formula for calculation of the number average chain molecular weight (M_c) value from the swelling ratio obtained in the equilibrium swelling experiment:

$$\frac{1}{M_c} = \frac{2}{M_n} - \frac{\frac{\bar{v}}{V_1}[ln(1-v_{2s}) + v_{2s} + \chi + v_{2s}^2]}{v_{2s}^{\frac{1}{3}} - \frac{v_{2s}}{2}} \tag{2.12}$$

In Equation 2.12, M_n represents the number average molecular weight before crosslinking, $\bar{v}$ is the specific volume of the polymer. The root-mean-square end-to-end distance of the polymer chains between crosslinks in an unperturbed state ($\sqrt{\langle \bar{r_0}^2 \rangle}$) depends on the number average molecular mass of the chains between crosslinks:

$$\sqrt{\langle \bar{r_0}^2 \rangle} = l\sqrt{\frac{2C_N M_c}{M_r}} \tag{2.13}$$

where l is the bond length along the polymer backbone (0.154 nm for vinyl polymers), C_N is the Flory characteristic ratio, and M_r is the molecular weight of the repeat units.

2.1.2 Mesh size

Mesh size of the hydrogel (ξ) is defined as the linear distance between two adjacent crosslinks

[3]. The mesh-size of the network is related to the swelling factor of the hydrogel, v_{2s}:

$$\xi = \sqrt{\langle \bar{r_0}^2 \rangle} \times v_{2s}^{-\frac{1}{3}} \tag{2.14}$$

v_{2s} can be experimentally determined by measuring the mass swelling ratio (Q_m):

$$v_{2s} = \frac{\frac{1}{\rho_{pol}}}{\frac{Q_m}{\rho_{solv}} + \frac{1}{\rho_{pol}}} \tag{2.15}$$

where ρ_{pol} is the density of the hydrogel and ρ_{solv} is the density of the solvent. Q_m is calculated based on:

$$Q_m = \frac{W_s}{W_d} \tag{2.16}$$

where W_s is the weight of the swollen hydrogel and W_d is the weight of the dry hydrogel.

Figure 2.4 summarizes the swelling process of hydrogel accompanied with the change in polymer network structure. Hydrogel mesh size can be adjusted by varying polymer con-

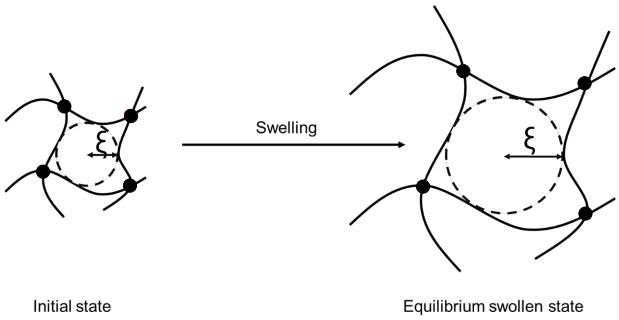

Figure 2.4: Swelling of the initial hydrogel in the presence of water. The filled circles represent chemical crosslinks, ξ represents the mesh size.

centration, crosslinking density, introduction of ionic polymers or changing conditions of the polymerization reaction (i.e. type of solvent, temperature, pH) [3]. As shown in Figure 2.5, drug release from hydrogels strongly depends on the drug to mesh size ratio [27].

When the mesh size is much larger than the drug (Figure 2.5-Fast diffusion), the drug release process is dominated by diffusion. Small drug molecules migrate freely through the network. The self-diffusion is similar to the one in solution (D_0) and depends on the radius of the drug molecule and the viscosity of the solution [27, 28], as expressed by the Stokes-Einstein equation:

$$D_0 = \frac{k_B T}{f} \tag{2.17}$$

where f is the friction coefficient which is dependent on the solvent viscosity and the geometry of the diffusing particle [29] .

When the mesh size matches the drug size (Figure 2.5-Slow diffusion), the effect of steric hindrance on drug diffusion becomes significant. The polymer chains induce frictional drag on diffusing drugs, and since the meshes in certain regions of the hydrogel network are smaller than the drugs, the path length for drug transport increases [27, 30]. The overall effect is slow drug diffusion, which allows for slow release.

For a very small mesh size combined with very large drug molecules (Figure 2.5-Immobilization), strong steric hindrance immobilizes the drugs. Drugs remain physically entrapped inside the network and can be release only after a combined degradation and diffusion process [27, 31].

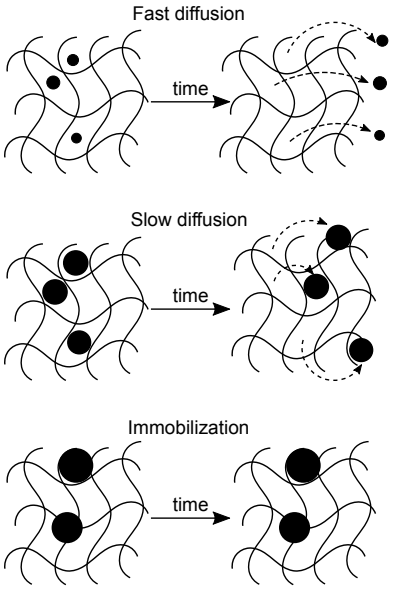

Figure 2.5: The dependence of the drug to mesh size ratio on the drug diffusion. Fast diffusion occurs when the mesh size is much larger than the drug molecule. Slow diffusion occurs when the size of drug approaches the mesh size. Drugs larger than a mesh size are physically entrapped (immobilized) inside the network. Adapted from [27].

There are many methods available for determining hydrogel mesh size, the most frequently used methods are listed in Table 2.1.

Table 2.1: Summary of methods used for characterizing the mesh size of hydrogels

Method	References
Equilibrium swelling	[23, 32, 33]
Rheology	[33–35]
NMR	[33, 36]
Small-angle X-ray scattering	[37]
Small angle neutron scattering	[38]

2.1.3 Elastic behavior of hydrogels

According to Flory's theory, the equilibrium shear elastic modulus corresponds to the frequency-independent elastic modulus (G') for a hydrogel network of Gaussian chains [25]:

$$G' = A\frac{\rho}{M_c}RT \tag{2.18}$$

where A is the structure factor, ρ is the polymer density, M_c is the number average chain molecular weight, R is the universal gas constant, T is the temperature. The structure factor A is determined by the assumed type of network. For an affine network, the crosslinks are embedded in the network and do not fluctuate. Thus, only the network chains contribute to the decrease of entropy of the network upon deformation (A = 1) [23]. For a phantom network, the crosslinks do fluctuate over time without being hindered by the neighboring polymer chains (A = 1-$\frac{2}{f}$, f being the functionality of the crosslinks) [39, 40].

Equation 2.18 can be developed to express the hydrogel mesh size, assuming that the mesh is either of cubical [41] or spherical [42] shape. Assuming cubical shape, the mesh size is defined as:

$$\xi_c^{rheo} = \left(\frac{RT}{G'N_A}\right)^{1/3} \tag{2.19}$$

where N_A is the Avogadro's number.

The following equation describes the mesh size for the spherical shape:

$$\frac{4}{3}\pi(\xi_s^{rheo}) = \frac{RT}{G'N_A} \tag{2.20}$$

2.1.4 Stimuli-responsive behavior

Stimuli-responsive hydrogels have over many years gained researchers' attention. Such hydrogels respond to external stimuli such as temperature or pH by changing their properties

drastically (dimension, structure, viscosity) [43]. Of special interest are thermoresponsive hydrogels in which only a small temperature change around a Lower Critical Solution Temperature (LCST) induces collapse of polymer chains and Volume Phase Transition (VPT). Since the earliest report of the LCST of P(NIPAM) in water by Scarpa et al. in 1967 [44], P(NIPAM) has become one of the most investigated thermosensitive polymers. Aqueous solutions of P(NIPAM) exhibits a LCST at 32° C, independent of polymer molecular weight and concentration [45]. P(NIPAM) hydrogel swollen in H_2O undergoes VPT at 34° C [6, 7]. The Volume Phase Transition Temperature (VPTT) is 1° C higher for the P(NIPAM) hydrogel swollen in D_2O. [7] This shift in VPTT can be explained by the slightly lower dielectric constant of D_2O (ε_{D_2O} = 78.06 at 25° C) compared to H_2O (ε_{H_2O} = 78.37 at 25° C) [46].

Figure 2.6 schematically summarizes the VPT phenomenon. P(NIPAM) hydrogels are swollen below VPTT, due to the strong hydrogen bonds formed between water and the amide or carbonyl groups of P(NIPAM). When the temperature is elevated, this hydrogen bonding is weakened and subsequently breaks above LCST. The hydrogel aggregates are formed through polymer-polymer hydrogen bonding, expelling water from the network [47]. The phase transition is initiated by dehydration of the isopropyl groups and the main polymer chain, followed by the dehydration of the amide groups [48].

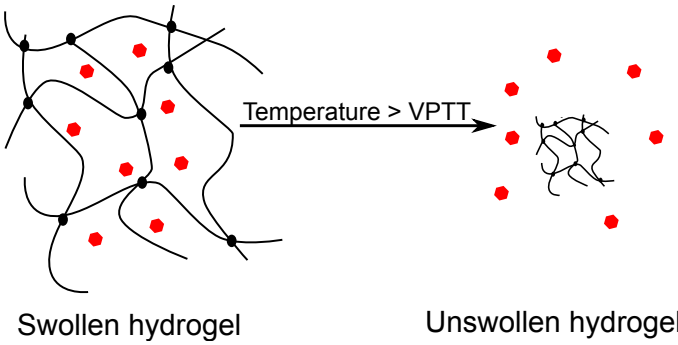

Figure 2.6: Schematic illustration of volume phase transition of temperature-responsive hydrogels. In response to the temperature increase over the VPTT, a temperature-responsive hydrogel in a swollen state, carrying a hydrophilic drug (shown as red hexagons) undergoes volume phase transition and becomes shrunk after expelling the solvent and drug.

2.2 Hydrogels as complex drug delivery systems

The use of hydrogels has been limited to delivery of hydrophilic compounds. However, it is estimated that more than 40% of marketed drugs and 60% of the drugs in the research phase, are hydrophobic [49]. One of the main approaches to improve the compatibility of hydrogels with hydrophobic compounds is the introduction of the molecules capable of forming inclusion complexes with hydrophobic molecules, such as micelles or cyclodextrins.

Surfactant micelles

Surfactants are amphiphilic molecules consisting of a hydrophilic head group and an alkyl hydrophobic tail (Figure 2.7). One of the fundamental properties of surfactants is that monomers in solution tend to form aggregates, so-called micelles. Micellization is a mechanism for removing hydrophobic groups from contact with water, thereby reducing the free energy of the system [50]. The concentration where micelles start to form is called the Critical Micelle Concentration (CMC). In a micelle, the surfactant hydrophobic group is directed towards the interior of the cluster and the hydrophilic head group is directed towards the solvent. Thus, micelles can be successfully used as carriers of hydrophobic compounds which can be physically entrapped in the core of the micelles.

Surfactants are classified according to their hydrophilic head group and thus can be nonionic, anionic or cationic. In this work, only cationic surfactant was used. Cationic surfactants are mainly based on amine-containing hydrophilic head group. They are frequently used as antibacterial agents, which may be advantageous also in certain drug delivery applications [51].

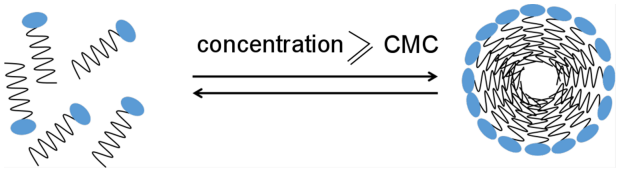

Figure 2.7: Schematic illustration of a reversible surfactant micellization. The surfactant head groups are marked in blue. The black curved lines represent the surfactant hydrophobic tail groups. Hydrophilic compounds can only be adsorbed within the micelle head-group compartment; while hydrophobic compounds can only be incorporated in the micelle core compartment.

β-cyclodextrins

Cyclodextrins (CDs) are a family of cyclic oligosaccharides with a hydrophilic outer surface and a hydrophobic central cavity. β-Cyclodextrin (βCD) consists of 7 α-D-glucopyranoside units (Figure 2.8a). The general structure of cyclodextrin can be described as a truncated hollow cone with primary and secondary hydroxyl groups oriented outward (Figure 2.8b). CDs possess an unique ability to act as molecular containers by entrapping guest molecules in their internal cavity. Drug - CD complex formation occurs through a non-covalent interaction between the drug and the CD cavity [52, 53]. Drug complexation by CDs is a dynamic process where the drug molecule continuously associates and dissociates from the CD [54].

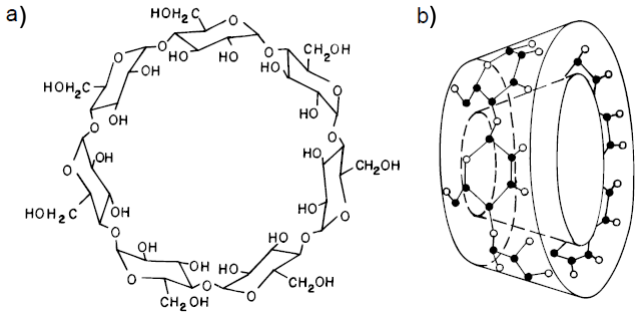

Figure 2.8: The chemical structure (a) and the truncated hollow cone of the βCD molecule (b). Taken from [53].

Because of the limited solubility of the βCD molecules, they are often incorporated to polymers by chemical modifications [55, 56]. βCDs can act as a crosslinker for the formation of a hydrogel [57, 58].

Drug delivery systems based on hydrogels containing moities such as micelles or CDs have been shown to successfully encapsulate and provide controlled release of the hydrophobic compounds [59, 60]. In this dissertation we chose to study the thermosensitive hydrogel system composed of P(NIPAM)-based polymer with embedded surfactant micelles and βCDs in order to gain detailed knowledge in transport of such molecules within and from these hydrogel systems.

[Hydrogels]

Chapter 3

NMR theory

In 1946, two independent research groups of Felix Bloch and Edward Purcell described NMR for condensed matter [61, 62]. The importance of the discovery was recognized by the Nobel Prize in Physics awarded to Bloch and Purcell in 1952. Since then, NMR has developed into a broad research field with applications in physics, chemistry and medicine. This chapter is written based on the books by Keeler [63] and Günther [64].

3.1 NMR signal

The spin of a nucleus can be considered as a magnetic moment ($\vec{\mu}$). When $\vec{\mu}$ is placed in a static magnetic field ($\vec{B}_0$) directed along the z axis (Figure 3.1), the time dependence of $\vec{\mu}$ is given by:

$$\frac{d\vec{\mu}}{dt} = \vec{\mu} \times \gamma \vec{B}_0 \tag{3.1}$$

The proportionality constant in Equation 3.1 (γ) is called a gyromagnetic ratio and depends on the nucleus.

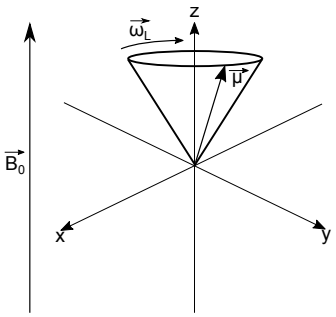

Figure 3.1: Precession of a magnetic moment ($\vec{\mu}$) in a static magnetic field ($\vec{B}_0$) with Larmor frequency ($\vec{\omega}_L$). Here, $\vec{\mu}$ could be replaced by the magnetization vector ($\vec{M}$).

Equation 3.1 can be solved in the rotating frame of reference, where the xy-plane is rotating with an angular frequency ($\vec{\omega}$).
In the rotating frame of reference, Equation 3.1 transforms to:

$$\frac{d\vec{\mu}}{dt} = \vec{\mu} \times (\gamma \vec{B}_0 + \vec{\omega}) \tag{3.2}$$

When $\vec{\omega} = -\gamma \vec{B}_0$, $\frac{d\vec{\mu}}{dt} = 0$, and the solution is given by $\vec{\mu}$ = constant, meaning that $\vec{\mu}$ is static in the rotating frame of reference, and further that $\vec{\mu}$ is precessing around $\vec{B}_0$ in the laboratory frame with the Larmor frequency ($\vec{\omega}_L$):

$$\vec{\omega}_L = -\gamma \vec{B}_0 \tag{3.3}$$

3.2 RF-pulse

The magnetization has to be rotated to the xy-plane in order to be measured. An oscillating electromagnetic pulse is used to excite all the spins. The magnetic part of the electromagnetic radiation is called $\vec{B}_1$. This weak magnetic field oscillating for a short time interval along the x-direction is called a Radio Frequency (RF) pulse. As shown in Figure 3.2, the $\vec{B}_1$ pulse is applied perpendicular to the static magnetic field; in the xy-plane. The most commonly used flip angles are 90° ($\frac{\pi}{2}$) and 180° (π).

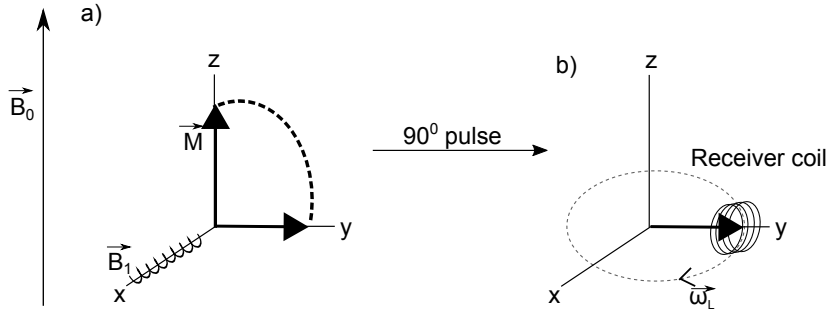

Figure 3.2: (a) If the radiofrequency field is applied for a certain time, the magnetization vector ($\vec{M}$) is rotated into the xy-plane. (b) To an external stationary observer (coil), the $\vec{M}$ is rotating at the Larmor frequency ($\vec{\omega}_L$) and can induce a signal in the coil.

The magnetic part of the RF field can be expressed as two vectors rotating in opposite directions in the xy-plane [63]. In the following section only one vector is taken into account (Figure 3.3).

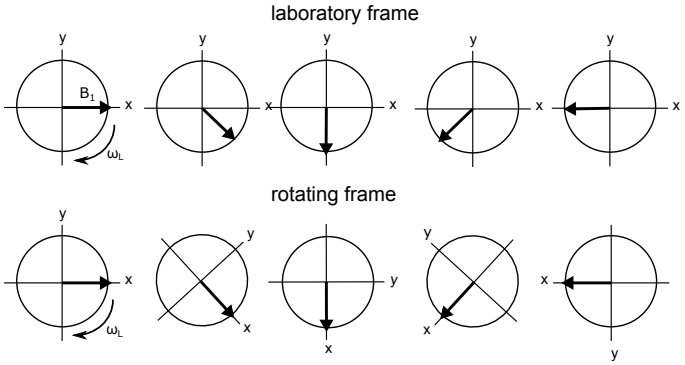

Figure 3.3: The motion of the field $\vec{B}_1$ viewed in a fixed axis system (laboratory frame, top row). The bottom row presents the motion of the $\vec{B}_1$ field in a rotating axis frame, which is rotating at $\vec{\omega}_L$ about the z-axis. The other vector will be rotating counterclockwise, and does not have to be taken into account. Adapted from [63].

Given the resonance condition in the rotating frame of reference $\vec{B}_1$ is static, and the time dependence of $\vec{\mu}$ is given by:

$$\frac{d\vec{\mu}}{dt} = \vec{\mu} \times \gamma\vec{B}_1 \tag{3.4}$$

It can be shown that this corresponds to a rotation of $\vec{\mu}$ around $\vec{B}_1$ in the yz-plane with an angular frequency $\vec{\omega}_1 = \gamma\vec{B}_1$.

The rotation angle is given by $\theta = \gamma B_1 t_p$, where t_p is the duration of the RF field pulse.

A summation over all $\vec{\mu}$s will give the total magnetization vector ($\vec{M}$):

$$\vec{M} = \sum \vec{\mu} \tag{3.5}$$

$\frac{d\vec{M}}{dt} = 0$ in the rotating frame of reference, where $\vec{M}$ will be statically aligned along the z-axis ($\vec{B}_0$), but will have no components in the x'y'-plane since the individual $\vec{\mu}$ vectors are out of phase with each other and the sum of the x'y'-components will be zero.

When a RF field is applied, phase coherence is created between the $\vec{\mu}$ vectors and the time dependence of $\vec{M}$ is given by:

$$\frac{d\vec{M}}{dt} = \vec{M} \times \gamma B_1 \tag{3.6}$$

When the RF field is turned off, relaxation processes can be introduced according to the well known Bloch-equations:

$$\frac{dM'_x}{dt} = -\frac{dM'_x}{T_2} \tag{3.7}$$

In Equation 3.7, T_2 is the transverse relaxation time.

$$\frac{dM'_y}{dt} = -\frac{dM'_y}{T_2} \tag{3.8}$$

$$\frac{dM_z}{dt} = -\frac{M_0 - M_z}{T_1} \tag{3.9}$$

In Equation 3.9, M_0 is the magnetization at thermal equilibrium, and T_1 represents the spin-lattice relaxation time.

Defining $M_x + iM_y = M_{xy}$, the solution from M_{xy} is given by:

$$M_{xy} = M_0 e^{-t/T_2} \tag{3.10}$$

where M_0 is the value of the xy-magnetization at t = 0.

In an inhomogeneous magnetic field, Equation 3.10 changes to [65]:

$$M_{xy} = M_0 e^{(-t/T_2^\star)} \tag{3.11}$$

where the time constant apparent transverse relaxation time ($T_2^\star$) defines the overall decay rate

due to both homogeneous (T_2) and inhomogeneous contributions ($T_2^{\dagger}$):

$$\frac{1}{T_2^{\star}} = \frac{1}{T_2} + \frac{1}{T_2^{\dagger}} \tag{3.12}$$

The solution for the z-magnetization is given by:

$$M_z = M_0(1 - A_0 e^{-t/T_1}) \tag{3.13}$$

A_0 is an integration constant that depends on the initial conditions. For $M_z(0) = 0$, A_0 = 1 (after a 90° pulse). For $M_z(0) = -M_0$, A_0 = 2 (after a 180° pulse).

3.2.1 Shaped RF pulses

Figure 3.4 presents the three most common types of RF pulses used in modern NMR experiments. Rectangular pulses, also called hard pulses, excite the whole range of chemical shifts and are applied when no spatial or spectral selection is necessary. The duration of a rectangular pulse is on the order of microseconds. The frequency profile corresponding to the rectangular pulse is *sinc* (Figure 3.4a) [66]. When spatial selectivity is required, the *sinc* or gaussian pulses are applied (Figure 3.4b-c). The frequency profile produced by the sinc pulse is a rectangle. However, this profile is only an ideal approximation since a *sinc* pulse have a finite duration and is obtained by truncating the pulse envelope [66, 67]. A gaussian pulse produces the frequency profile in a gaussian form.

Sinc or gaussian-shaped RF pulses are reduced in intensity and increased duration (hundreds of microseconds to milliseconds) comparing to hard pulses [68].

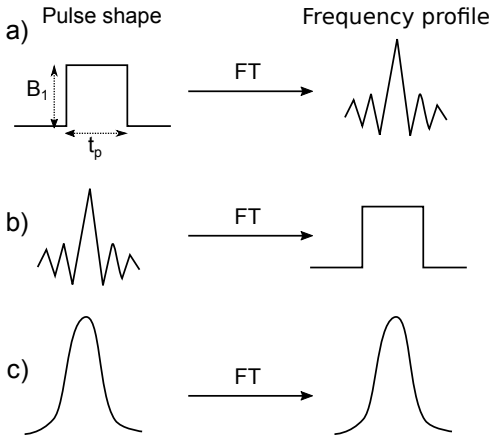

Figure 3.4: RF pulses shapes and corresponding frequency profiles; (a) rectangular RF pulse with amplitude, B_1 and duration, t_p produces a sinc-shaped frequency profile; (b) sinc RF pulse and rectangular frequency profile; (c) gaussian RF pulse and frequency profile. Frequency profiles can be calculated by Fourier transformation (FT). Adapted from [68].

3.3 NMR spectrum

A Fourier Transform (FT) of the Free Induction Decay (FID) gives a spectrum with peaks corresponding to the resonance frequencies of the spins in the sample. With an applied $\vec{B_0}$, the resonances of a molecule appear at $\nu_0 \pm \Delta\nu$. The local magnetic field (B_{local}) is influenced by the chemical environment of a nucleus of the molecule. The magnitude of B_{local} is given by:

$$B_{local} = B_0(1-\sigma) \tag{3.14}$$

where σ is known as shielding constant of the particular proton.

The corresponding signal frequency is:

$$\nu = \frac{\gamma B_0(1-\sigma)}{2\pi} \tag{3.15}$$

According to Equation 3.15, the signal frequency varies with $\vec{B_0}$. As NMR spectrometers operate at different $\vec{B_0}$ fields, the comparison of the signal frequencies between spectrometers operating at different field strengths is difficult. Therefore, the position of a peak in the spectrum is specified by measuring its frequency separation from the reference peak ν_{ref}, and dividing this difference by the frequency of the reference peak. The chemical shift (in Equation

3.16) (δ) is defined as follows:

$$\delta = 10^6 \times \frac{\nu - \nu_{ref}}{\nu_{ref}} \tag{3.16}$$

The δ values are quoted in 'parts per million' (ppm).

3.4 Spin echo

Due to small local inhomogeneities in the $\vec{B}_0$, the Larmor precession frequencies of the spins varies throughout the sample. As shown in Equations 3.11 - 3.12, the FID decay after applying a RF pulse is faster than due to T_2- relaxation effects alone [69]. The pulse sequence discovered in 1950 by Edward Hahn [70] refocuses any decay due to the magnetic field inhomogeneities. Therefore, the Hahn spin echo pulse sequence shown in Figure 3.5 is a fundamental component of many modern NMR experiments. In this pulse sequence, the initial $90°_x$ pulse aligns the magnetization vector along the -y axis. During the first time interval following the RF pulse (τ)-delay, the magnetization vector precesses freely from -y to x-axis and rotates in the x-y plane at a rate, Ω. The angle through which the vector rotates is $\Omega\tau$. The $180°_x$ pulse flips the magnetization vector to a mirror image position. The angle is $\Omega\tau$ with respect to y-axis, and $\pi - \Omega\tau$ with respect to -y-axis. During the second τ-delay the vector continues to evolve freely acquiring the $\Omega\tau$ phase. At the end of the sequence, the total phase is $(\pi - \Omega\tau) + \Omega\tau = \pi$ and the magnetization vector is aligned along the y-axis. Thus, the final magnetization vector is independent on the offset Ω.

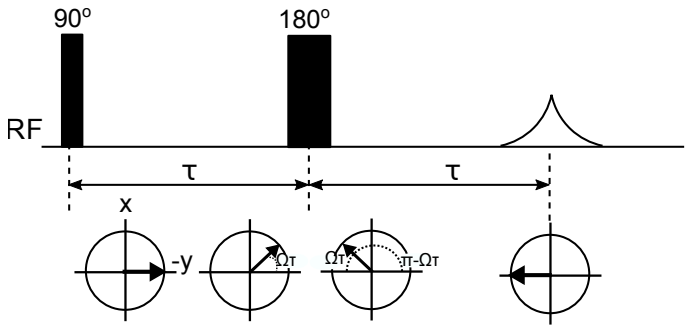

Figure 3.5: The Hahn spin echo experiment. After the first 90° pulse the NMR signal decays because of the field inhomogeneities. The 180° pulse applied after τ-delay inverts the magnetization vector. During the second τ-delay, the magnetization vector is refocused and a spin echo is produced after 2τ.

3.5 Pulsed Field Gradient (PFG) NMR

3.5.1 Magnetic Field Gradient

The magnetic field can intentionally be made inhomogeneous for a short period of time. This effect can be accomplished by applying a magnetic field along the z-axis (B_z) (Figure 3.6). B_z varies linearly with the z-axis. The magnetic field, due to the combination of the gradient and the B_0 becomes [63]:

$$B_z = B_0 + G_z \tag{3.17}$$

where G_z is the magnetic field gradient (T m^{-1} or G cm^{-1}) in the z - direction. Since the effective magnetic field varies by $B_0 + \Delta B_z$, the Larmor frequencies of nuclei at different positions vary by $\omega_L + \Delta\omega_z$.

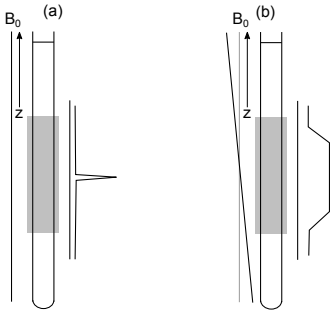

Figure 3.6: The effect of a magnetic field gradient on the NMR spectrum. The sensitive volume of the sample is shown by the gray rectangle (a) NMR sample in a homogeneous magnetic field, $\vec{B}_0$. The spectrum is expected to have the narrow line. (b) The gradient is applied, and B_z varies with z. Spins in different parts of the sample have different Larmor frequencies. The spectrum is expected to have a broad line. Adapted from [63].

3.5.2 Pulsed Field Gradient Spin Echo (PFGSE)

Almost all NMR diffusion experiments are based on different forms of spin echoes (Figure 3.5) [70]. In 1965 Stejskal and Tanner introduced the Pulsed Field Gradient (PFG) NMR technique for measuring self-diffusion [71].

The PFG NMR method is a well-established technique for studying molecular motion without disturbing the investigated system. The PFGSE pulse sequence is based on the Hahn spin echo as shown in Figure 3.7. A gradient pulse, G_z located after the first 90° RF pulse,

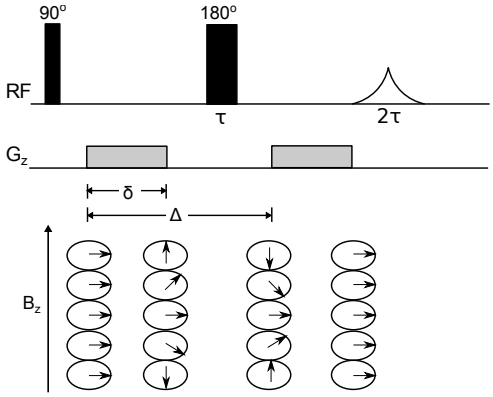

Figure 3.7: The Pulsed Field Gradient Spin Echo (PFGSE) experiment. The upper part presents the schematic diagram of a pulse sequence. The bottom part shows the phase evolution of the spins at different locations along the gradient direction [71].

induces a position-dependent increase of the Larmor precession of the spins, which leads to a defocussing process for the transverse magnetization. During the diffusion time (Δ), a number of spins change their position on the z-axis. A 180° RF pulse in the middle between the 90° RF pulse and the signal acquisition forms a spin echo and refocuses any chemical shift evolution at the start of acquisition. The signal decay is governed by T_2. The amplitude of Stejskal and Tanner signal is given by:

$$S(g,2\tau) = M_0 exp\left(-\frac{2\tau}{T_2}\right) exp\left[-\gamma^2\delta^2G^2\left(\Delta-\frac{\delta}{3}\right)D_s\right] \tag{3.18}$$

Equation 3.18 can be normalized with respect to the echo intensity (E) obtained at G=0:

$$E(g,\Delta) = E(g,2\tau) = \frac{S(g,2\tau)}{S(g=0,2\tau)} = exp\left[-\gamma^2\delta^2G^2\left(\Delta-\frac{\delta}{3}\right)D_s\right] = exp(-bD_s) \tag{3.19}$$

where b is known as the diffusion weighting factor and is defined by $-\gamma^2\delta^2G^2(\Delta-\frac{\delta}{3})$. The normalized signal amplitude, $\frac{E}{E_0}$ decreases exponentially with increasing gradient strength, G (Figure 3.8a). The D_s may be obtained from the slope of a linear plot of $ln(\frac{E}{E_0})$ against b as shown in Figure 3.8b.

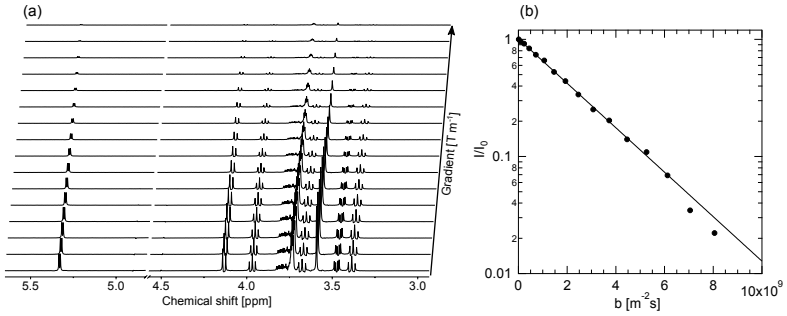

Figure 3.8: Diffusion of sucrose (10 mM) in the solution recorded as calibration of the diffusion probe. (a) Echo attenuation. (b) Fitting of Equation 3.19 results in self-diffusion coefficient (D_s) equal to $4.37 \pm 0.05 \times 10^{-10}$ m^2 s^{-1}.

3.6 Magnetic Resonance Imaging (MRI)

Magnetic Resonance Imaging (MRI) developed from the application of NMR to radiological imaging with the goal to correlate NMR signals with spatial locations [72]. This can be accomplished by applying a spatially changing magnetic field across the sample. Three magnetic field gradients are used in MRI experiments, G_x, G_y and G_z. The result is a 2D or 3D image.

3.6.1 Slice selection

In MRI, slice selection is the first step in signal localization. Inhomogeneous and phase-separated samples can be characterized by means of slice-selective NMR to obtain localized information about the chemical environment. As shown in Figure 3.9, application of the magnetic field gradient pulse applied in the z-direction (G_z) leads to a transverse slice of the sample.

When a magnetic gradient is applied in the z-direction, the Larmor frequency expressed in Equation 3.3 becomes spatially dependent ω_z [63]:

$$\omega_z = -\gamma B_z = -\gamma(B_0 + G_z z) \tag{3.20}$$

According to Section 3.5.1, G_z in Equation 3.20 may be defined as:

$$G_z = \frac{\partial B_0}{\partial z} \tag{3.21}$$

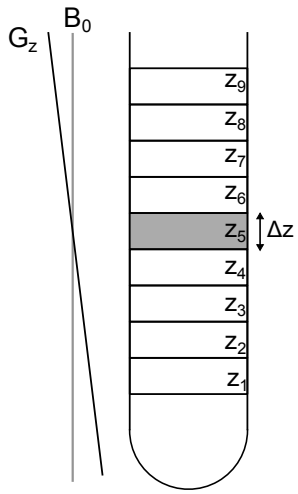

Figure 3.9: Example of the slice selection. The selected slice (z_5) of thickness Δz is highlighted in gray. Only ^{1}H for the selected slice will contribute to the signal.

Keeping in mind that the Larmor frequency in B_0, ω_L, is expressed by Equation 3.3, the frequency at position z is:

$$\omega_z = \omega_L - \gamma G_z z \tag{3.22}$$

To excite a slice of a certain thickness given by Δz, centered at z_0 the RF pulse should have a frequency profile ($\Delta\omega_z$) extending from $\left(-\gamma G_z z_0 + \gamma G_z \frac{\Delta z}{2}\right)$ to $\left(-\gamma G_z z_0 - \gamma G_z \frac{\Delta z}{2}\right)$ [72].
By setting the bandwidth of the RF pulse (BW) equal to $\Delta\omega_z$ one obtains:

$$BW = \Delta\omega_z = \left(-\gamma G_z z_0 + \gamma G_z \frac{\Delta z}{2}\right) - \left(-\gamma G_z z_0 - \gamma G_z \frac{\Delta z}{2}\right) = -\gamma G_z \Delta z \tag{3.23}$$

Slice selection can be achieved by applying a selective RF pulse (Figure 3.4b-c) and a magnetic field gradient simultaneously (Figure 3.10) [73]. The slice thickness can be adjusted by varying the BW, and G_z:

$$\Delta z = \frac{BW}{|\gamma G_z|} \tag{3.24}$$

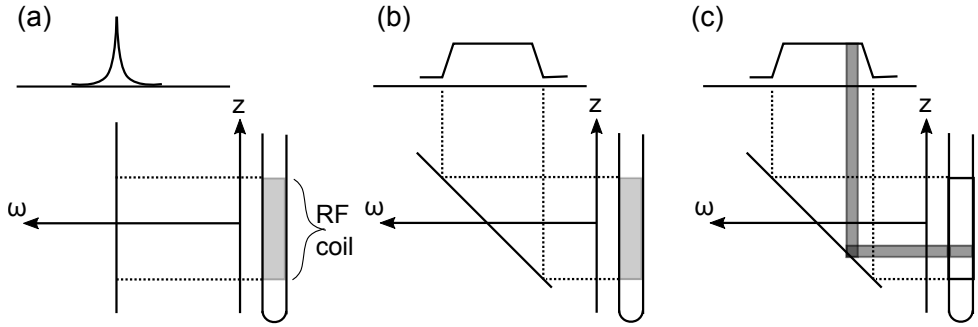

Figure 3.10: The effect of magnetic gradient and slice selective pulse on the frequency spectrum. (a) Frequency spectrum in the absence of magnetic field gradient. (b) The frequency spectrum in the presence of the magnetic field gradient. The spatial profile presented in here corresponds to the RF coil region. (c) Application of a selective pulse bandwidth (BW) together with a magnetic field gradient. A slice of thickness proportional to BW is selected. Adapted from [73].

Because the signal arises only from a discrete slice of the sample, the sensitivity of the spatially-selective NMR experiment is reduced by:

$$\frac{S_z}{S_0} \sim \frac{\Delta z}{L} = \frac{BW}{\gamma G L} \tag{3.25}$$

where S_z is the signal resulting from the slice-selective experiment, S_0 is the signal in the absence of spatial selection, L is the length of the sample or the RF coil and Δz is the slice thickness [73].

The local spin density, ρ_z for spins within the volume element dV is ρ_zdV. The NMR signal from this element may be written as:

$$dS(G_z,t) = \rho_z exp[i\omega_z t]dz \tag{3.26}$$

Inserting Equation 3.20 into Equation 3.26 results in:

$$dS(G_z,t) = \rho_z exp[i(\gamma B_0 + \gamma G_z z)t]dz \tag{3.27}$$

Here, relaxation effects are neglected. A transformation into the rotating frame of reference followed by explicit integration over all space allows to write Equation 3.27 in terms of the observed signal S as function of time and therefore becomes:

$$S(t) = \iiint \rho_z exp[i\gamma G_z z t]dz \tag{3.28}$$

where symbol dz represents integration over all space. Mansfield and Grannel [74] simplified the meaning of Equation 3.28 by introducing the concept of k-space which is defined by:

$$k = \frac{\gamma}{2\pi} \int_0^t G(t)dt \tag{3.29}$$

where γ for ^{1}H is 2.675 $\times$ 10^8 rad s^{-1} T^{-1}. Here, G represents the maximum strength of the magnetic field gradient. The k-space vector units are in reciprocal space units: m^{-1}.

3.6.2 Spatial encoding

The next steps in the image formation are defined as space encoding of the image [75]. After a slice has been selected, the positions of the ^{1}H signals within the slice need to be localized. The signals are differentiated by applying two additional gradients, frequency-encoding (G_x) and phase-encoding (G_y) gradients.

When the frequency-encoding gradient (G_x) is applied, the frequencies along the x-axis are changed spatially. The time integrals of the applied G_x control the sampling of the k-space (k_x) as follows:

$$k_x = \frac{\gamma}{2\pi} \int_0^t G_x(t)dt \tag{3.30}$$

G_x is applied during the signal acquisition.

When a phase-encoding gradient (G_y) is applied, the frequencies along the y-axis are changed spatially. G_y is applied before the acquisition of the signal. The corresponding k-space (k_y) is defined as:

$$k_y = \frac{\gamma}{2\pi} \int_0^t G_y(t)dt \tag{3.31}$$

The combination of the frequency-encoding and phase-encoding gradients provides the basis for the application of the inverse two-dimensional Fourier transform. The signal of the 2D image is defined as [76]:

$$M(k_x, k_y) = \int_x \int_y m\ (x,\ y)\, e^{-i2\pi[k_x x + k_y y]} dxdy \tag{3.32}$$

Figure 3.11 presents an example of a sequence for a spin echo 2D imaging with a 180° pulse, and phase and frequency encoding. Starting at $k_x = 0$ and $k_y = 0$, the gradient pulse applied along the x-axis (G_x) moves the position in k-space to $k_{x,max}$. The 180° pulse moves the position in k-space to the left side of the k-space diagram ($-k_{x,max}$). The position in k-space is moved to a specific position along k_y in the diagram using a positive phase-encoding gradient (G_y). The line is sampled by using G_x along to the x-axis direction until all of k-space is covered. The value of G_y is varied in a steplike fashion allowing to gather information from the whole k-space during different repetitions.

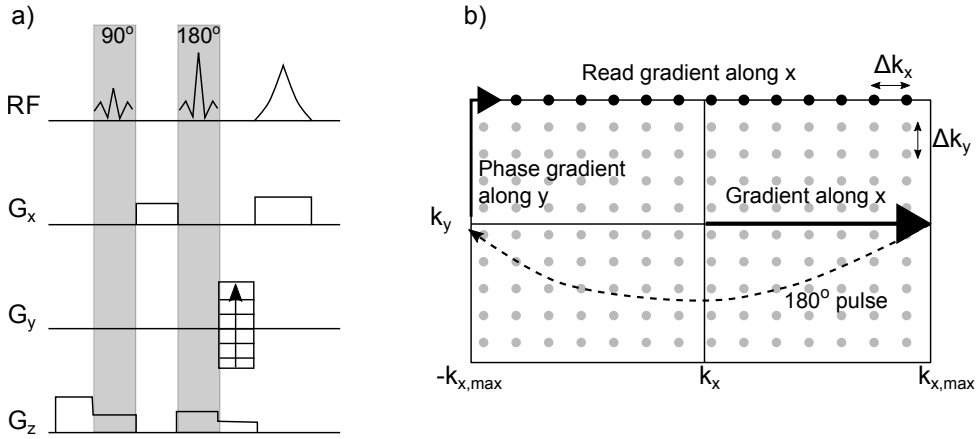

Figure 3.11: The pulse sequence (a) and the k-space coverage (b) for a 2D MRI experiment using a standard spin-echo sequence with phase and frequency encoding. Starting at $k_x = 0$ and $k_y = 0$, the gradient pulse applied along the x-axis (G_x) moves the position in k-space to $k_{x,max}$. The dashed line represents the action of the 180° pulse which changes $k_{x,max}$ to $-k_{x,max}$. Applying a positive phase-encoding gradient (G_y) moves the position in k-space to the highest line ($-k_{x,max}$ and $k_{y,max}$). G_y is pictured as a series of horizontal lines to denote that it is being stepped regularly through varying values during different repetitions. The line is sampled (black dots) by using G_x parallel to the x-axis direction. Subsequently, the position returns to $k_x = 0$ and $k_y = 0$ and new lines are sampled at different k_y positions (gray dots).

The separation between points in k-space shown in Figure 3.11 (Δk_x and Δk_y) is proportional to the inverse of the Field of View (FOV) in image space [76]:

$$\Delta k_i = \left(\frac{1}{FOV_i}\right) \tag{3.33}$$

where i represents the spatial dimensions x or y. The spatial resolution Δi in the resultant

image is determined by the highest value of the sampled k-space ($k_{i,max}$):

$$\Delta i = \frac{2}{k_{i,max}} \tag{3.34}$$

where Δi is the spatial resolution in direction i.

3.6.3 1D Chemical Shift Imaging (CSI)

The 1D Chemical Shift Imaging (CSI) NMR method, based on a well-known MRI experiment, can be used to study the transport processes in colloidal systems [77–82]. NMR signals are phase-encoded for position by applying rectangular magnetic field gradients of varying strength. The pulse sequence for a 1D CSI experiment is shown in Figure 3.12.

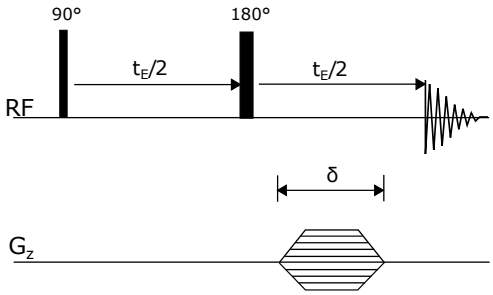

Figure 3.12: 1D Chemical Shift Imaging (CSI) pulse sequence. Application of the 90° RF pulse and the refocusing 180° RF pulse results in an echo at time t_E. The magnetic field gradient pulse encoding the signal for position, is applied along the z-axis (G_z). δ indicates the duration of the G_z pulse [16].

For the 1D CSI experiment, only phase encoding is used and k_y is varied along the $k_x = 0$ axis.

3.6.4 Solvent suppression

In a ^{1}H NMR single pulse spectrum, the area of a signal is directly proportional to the number of ^{1}H nuclei contributing to this signal. Consequently, intensities of the solvent signals are much larger than the resonances of interest. One can avoid this issue by using deuterated solvents. However, protons in some chemical groups such as -NH or -OH, are exchangeable with deuterium ions and thus 'disappear' from the ^{1}H NMR spectrum. Moreover, deuterated solvents are much more expensive than protonated ones, thus their usage may be limited when

large amounts of solvent are required for sample preparation. Alternatively, the solvent signal can be suppressed by saturation with a low-power selective RF pulse applied on the solvent resonance [83]. Many other solvent suppression techniques have been developed, and the most common methods are summarized in the review by Zheng and Price (2010) [84].

3.6.5 Localized spectroscopy

Application of the magnetic field gradients described in Sections 3.6.1 - 3.6.2 allows for selective excitation of a Volume of Interest (VOI) in the sample [77, 85–87]. The two most widely used methods for excitation of VOI use three orthogonal spatially-selective pulses: 90°-180°-180° as in Point Resolved Spectroscopy (PRESS) [85] or 90°-90°-90° as in the STimulated Echo Acquisition Mode (STEAM) pulse sequence [86]. In this dissertation, the STEAM pulse sequence was used to obtain spectra from selected VOIs.

[NMR theory]

Chapter 4

Diffusion

The term diffusion refers to the random translational incoherent motion of molecules. There are two common forms of diffusion: self-diffusion and mutual diffusion (Figure 4.1). Although having the same units (length^2 time^{-1}), the physical origins of these phenomena are different. Self-diffusion, denoted by the self-diffusion coefficient (D_s) is the random Brownian motion of molecules in pure or uniform solution resulting from the internal kinetic energy [29, 88]. Self-diffusion is the most fundamental form of transport involved in all chemical reactions, since the reacting species must collide before they can react [29, 89]. At infinite dilution, D_s of a molecule relates to its molecular size and is sensitive to molecular interactions and temperature [90, 91].

For a particle at infinite dilution, the self-diffusion coefficient is denoted by D_0 and relates to the hydrodynamic size through the Stokes-Einstein relation (Equation 2.17). For a sphere with an effective hydrodynamic radius (R_h), in a solvent viscosity (η), the friction coefficient in Equation 2.17 is given by:

$$f = f_{sphere} = \lambda \pi \eta R_h \tag{4.1}$$

where the λ parameter depends on the boundary conditions. When the particle interacts strongly with the solvent molecules such that the solvent layer closest to the surface moves at the same velocity as the particle (the so-called stick boundary condition), the λ parameter is equal to 6 [29].

Mutual diffusion (also known as inter diffusion or concentration diffusion) is caused by the gradient of the chemical potential, and is characterized by a mutual diffusion coefficient (D_m). A concentration inhomogeneity of any component in a system results in mass fluxes to

achieve thermodynamic equilibrium. In a volume-fixed reference frame there is only one D_m.

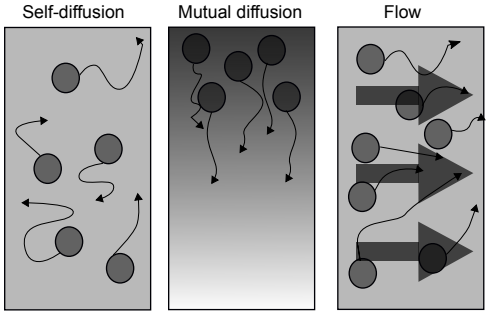

Figure 4.1: A scheme representing the difference between self-diffusion, mutual diffusion, and flow. For self-diffusion, the uniform background indicates the uniform concentration of the molecules. For mutual diffusion, the gradient color of the background reflects a concentration gradient in the sample. In the illustration of flow, the large arrows indicate the direction bulk fluid movement. Adapted from [92].

There are many methods for measuring diffusion, the most common ones are summarized in Table 4.1. Numerous non-NMR methods exist for measuring diffusion such as light scattering, neutron scattering, fluorescence studies, but their application can be limited by a concentration range, complex sample preparation or are invasive in nature [91, 93].

Table 4.1: Summary of methods used for measuring diffusion and the type of diffusion measured.

Method	Type of Diffusion	References
Rayleigh scattering	Self	[94]
Taylor dispersion	Mutual	[95]
Small-angle neutron scattering	Self	[96]
Fluorescence correlation spectroscopy (FCS)	Self and mutual	[97, 98]
Fluorescence recovery after photobleaching (FRAP)	Self	[99]
Dynamic light spectroscopy	Mutual	[100]
NMR/MRI diffusion	Self and Mutual	[16, 101, 102]

4.1 Propagation

For isotropic diffusion in three dimensions, the flux of a particle ($\mathbf{J}(\mathbf{r},t)$) is given by Fick's first law of diffusion [29, 88, 103]:

$$\mathbf{J}(\mathbf{r},t) = -D_m \nabla c(\mathbf{r},t) \tag{4.2}$$

where $\mathbf{r}$ is the position vector, ∇c is a concentration gradient and t is time. The minus sign indicates that the direction of flow is from higher to lower concentration [29, 88, 103]. Since the number of diffusing particles is conserved, the continuity theorem applies and the diffusion equation can be written as:

$$\frac{\partial c(\mathbf{r},t)}{\partial t} = -\nabla \times \mathbf{J}(\mathbf{r},t) \tag{4.3}$$

Equation 4.3 describes the accumulation or loss of particles from the point located at $\mathbf{r}$. Combining Equations 4.2 and 4.3, Fick's second law of diffusion can be derived:

$$\frac{\partial c(\mathbf{r},t)}{\partial t} = D_m \nabla^2 c(\mathbf{r},t) \tag{4.4}$$

where ∇^2 is the Laplace operator.

4.2 Self-diffusion equation

A diffusion propagator ($P(\mathbf{r}_0,\mathbf{r}_1,t)$) describes the conditional probability of finding a particle initially at a position r_0, at a position r_1 after a time t [29, 89]. Contrary to mutual diffusion, there is no concentration gradient in self-diffusion. Therefore, the concentration terms in the diffusion equations are replaced with the diffusion propagator P($\mathbf{R},t$), which describes the probability for a molecule to move a distance $\mathbf{R}$ = $\mathbf{r}_1$ - $\mathbf{r}_0$. If the term $c(\mathbf{r},t)$ is replaced with $P(\mathbf{r}_0,\mathbf{r}_1,t)$in Equation 4.2, $\mathbf{J}$ becomes the conditional probability flux. Thus, the same substitution in Equation 4.4 leads to:

$$\frac{\partial P(\mathbf{r}_0,\mathbf{r}_1,t)}{\partial t} = D_s \nabla^2 P(\mathbf{r}_0,\mathbf{r}_1,t) \tag{4.5}$$

where D_s is the self-diffusion coefficient. Equation 4.5 is the Einstein diffusion equation.

For three dimensional diffusion in an isotropic and homogeneous medium (where P$\rightarrow$ 0 and r$_1$ $\rightarrow$ 1), the propagator $P(\mathbf{r}_0,\mathbf{r}_1,t)$ is determined from Equation 4.5 using Fourier transforms and is given by a Gaussian function [29, 89]:

$$P(\mathbf{r}_0,\mathbf{r}_1,t) = (4\pi D_s t)^{-3/2} exp\left(-\frac{(\mathbf{r}_1-\mathbf{r}_0)^2}{4D_s t}\right) \tag{4.6}$$

For isotropic diffusion, D_s can be determined by the mean-squared displacement (MSD), $\langle R^2 \rangle$, by:

$$\langle R^2 \rangle = nD_s t_d \tag{4.7}$$

where t_d is the diffusion time, and n is the dimensionality of the system. As shown by Equation 4.7, MSD varies linearly with time for free diffusion and such diffusion is said to be 'Fickian'.

For real systems (e.g. polymer networks [30]), the diffusion will be anisotropic as a result of the physical arrangement or obstructions [29, 89]. As $\langle R^2 \rangle$ will be influenced by any boundaries, D_s can provide information about the restricting geometry. Thus, for restricted or obstructed diffusion, the D_s is time-dependent and dependent on the geometry of the confined space [91]. When taking place in confined geometries, MSD is not a linear function of time. In a sphere of radius a the restriction effect (ζ) on diffusion can be described as:

$$\zeta = \frac{D_s t_d}{a^2} \tag{4.8}$$

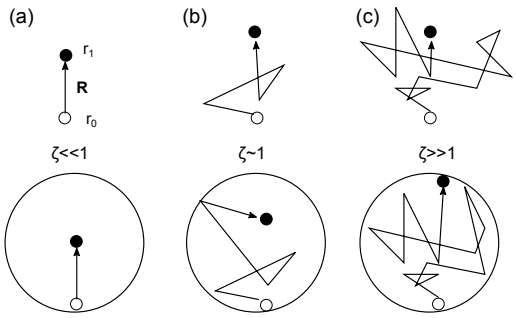

Figure 4.2: The effect of measurement timescale when measuring free diffusion (top) with diffusion in a restricted geometry (bottom). The molecule's displacement occurs along the z-direction. The starting position (at t = 0) is denoted as an open circle ($\mathbf{r}_0$), while the final position (at t=t_d) is presented as a closed circle ($\mathbf{r}_0$). **R** is the displacement between the initial and the final positions. Adapted from [29].

The effects of the restrictions are often described for three timescales:

a) a short-time limit ($\zeta \ll 1$) where the diffusion is unrestricted as the diffusing molecules do not reach the boundaries of the restriction. MSD is given by Equation 4.7.

b) intermediate times ($\zeta \sim 1$) where the sampled MSD approaches the length scale of the restricting geometry. MSD will not scale linearly with t_d:

$$\langle R^2 \rangle = \alpha D_s t_d^{2/d_w} \tag{4.9}$$

where α is a time-independent scaling constant and d_w is the random walk dimension [29].
c) a long-time limit ($\zeta \gg 1$) where MSD depends only on the shape, dimensions and orientation of the restricting geometry and is independent of the t_d.

4.3 Diffusion in hydrogels

Solute diffusion in hydrogels depends on intermolecular interactions between the solute and the polymer network [104]. Solute self-diffusion decreases in the presence of hydrogen bonding or hydrophobic interactions with the hydrogel [105, 106]. Many models have been developed to describe relationships between hydrogel structure and transport properties [30, 102, 107].

In the absence of intermolecular interactions, the self-diffusion coefficient of solute in the hydrogel (D_s^{gel}) decreases due to hydrodynamic interactions with the polymer network [104, 108, 109]:

$$D_s^{gel} = D_s^0 \times exp\left(-\frac{R_h}{\xi}\right) \tag{4.10}$$

where D_s^0 represents self-diffusion coefficient of solute in solution, R_h is a hydrodynamic ratio of a diffusing solute and ξ is a hydrogels mesh size. Transport of a molecule/particle in hydrogels takes place within the water-filled voids in the space between the polymer chains [30]. Thus, any reduction in the size of these spaces will directly influence the transport properties.

[Diffusion]

Chapter 5

Materials and Methods

5.1 Hydrogel synthesis

The polymer network systems studied here was based on the Poly(*N*-isopropylacrylamide-*co*-acrylic acid) (P(NIPAM-co-AAc)) polymer (Paper I) and Poly(*N*-isopropylacrylamide) (P(NIPAM)) (Papers II and III). Hydrogels were prepared by the free radical crosslinking polymerization procedure using *N*-isopropylacrylamide (NIPAM) (Papers I, II and III) or NIPAM and Acrylic Acid (AAc) (Paper I) as monomers, *N,N'*-Diallyl L-tartardiamide (DAT) as a crosslinker, the activator *N,N,N',N'*-Tetramethylethylenediamine (TEMED), the initiator Ammonium Persulfate (APS), and distilled water as a solvent. The monomers, the crosslinker and the initiator were dissolved in distilled water. The total concentration of the monomers was 0.7 mol L^{-1}. In Paper I, the molar ratio of NIPAM to AAc was 0.95 to 0.05, and the concentration of DAT was varied between 0.006 and 0.143 mol L^{-1} . In Papers II and III, only NIPAM was used as a monomer, and the concentration of DAT was 0.024 mol L^{-1} (Paper II) and 0.048 mol L^{-1} (Paper III). After deoxygenating the solutions by sonication in ultrasonic bath and nitrogen bubbling, the polymerization reaction was started by adding the activator. The free radical polymerization reactions for P(NIPAM-co-AAc)-based hydrogel is presented in Figure 5.1.

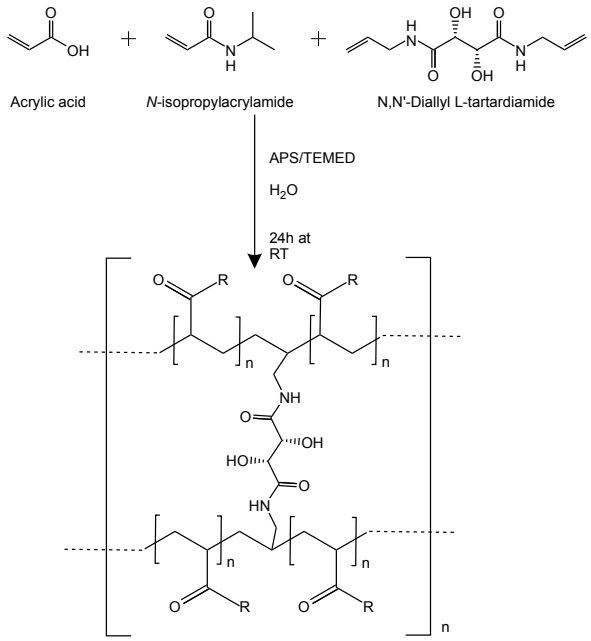

Figure 5.1: Synthetic scheme for the preparation of P(NIPAM-*co*-AAc) hydrogels studied in Paper I by free radical copolymerization. R represents the hydroxyl group in acrylic acid or -NH-CH-$(CH_3)_2$ groups in *N*-isopropylacrylamide.

5.2 NMR experiments

All the NMR experiments in Papers I and II were performed on a Bruker Ascend 500 WB MHz NMR spectrometer equipped with a Bruker DiffBB broadband gradient probe capable of delivering gradients of strength 17 T m^{-1} in the z-direction. All the MRI experiments in Paper III were performed on a Bruker Ascend 500 WB MHz NMR spectrometer equipped with a commercial Bruker MicWB40 micro imaging probe head in combination with the Micro 2.5 gradient system capable of producing magnetic field gradient pulses up to 1.5 T m^{-1}.

5.2.1 Temperature control

In the NMR experiments, the temperature was maintained at 25°C using a Bruker Variable Temperature Unit. In the MRI experiments, the temperature was maintained at 31°C or at 40°C with a Bruker BCU20 cooling device. A calibration curve for the temperature was prepared using the standard Bruker reference sample containing 80% glycol in DMSO-d6 (Figure 5.2a). Due to the time delay between BCU20 unit and the sample, a temperature - time calibration

curve was prepared (Figure 5.2b) and employed for the study.

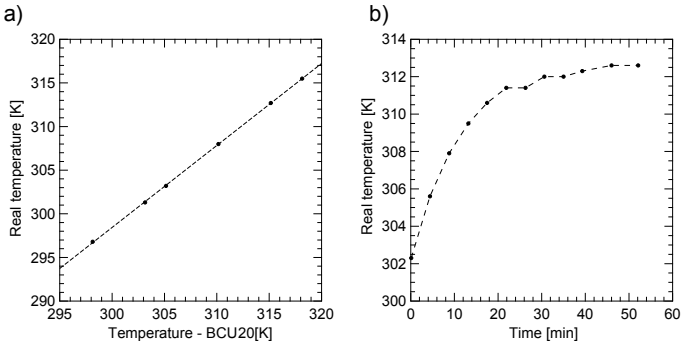

Figure 5.2: (a) The temperature calibration curve used in the MRI experiments. The fitting of a linear function to the experimental data yields real temperature = temperature (BCU20) $\times$ 0.94 + 16. (b) The temperature - time correlation curve. The real temperature term refers to the calibrated temperature in the sample.

5.2.2 Pulsed Field Gradient Stimulated Echo (PFGSTE)

During the Stejskal-Tanner Pulsed Field Gradient Stimulated Echo (PFGSTE) sequence the information on spin phases is stored in the longitudinal direction during diffusion time, Δ which is limited by T_1. Magnetic susceptibility of some samples, such as porous materials or colloidal suspensions, can be heterogeneous. Thus, a distribution of magnetic field gradients will be associated with nonuniform sample magnetization. Such background gradients may lead to a decrease in the observed T_2 through the effect of translational diffusion of nuclear spins [110, 111]. To reduce the effects of the background gradients, two 180° pulses are introduced in the PFGSTE sequence. For the self-diffusion measurements in Paper I, the 2D stimulated echo (diffSteBp) pulse sequence was used [111]. As shown in Figure 5.3, two gradient pulses with opposite signs enclose a 180° pulse. This sequence is used to remove the effect of internal gradients in the sample. The dephasing resulting from internal static gradients is removed by means of the 180° pulse. The effect of the applied gradient is kept by reversing the gradient after the 180° pulse. The gradient pulses are centered in the gaps between the RF pulses. The delay between the first two 90° pulses is called τ. δ defines the effective length of the gradient pulses describing the phase encoding strength of the two gradient pulses. The distance between the two 180° pulses, which are the effective centers of the two gradient pulse pairs, is called the diffusion time(Δ). A spoiler gradient, $G_{spoiler}$ is used to get rid of coherent magnetization during the evolution period.

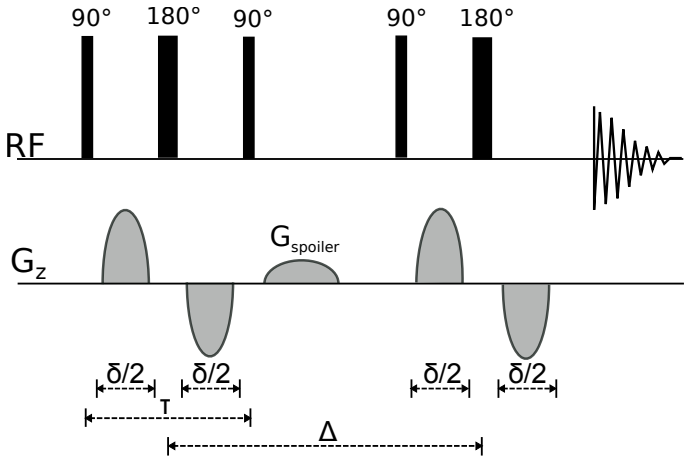

Figure 5.3: Schematic illustration of the diffSteBp pulse program [111].

5.2.3 Slice-selective NMR

In Paper II the slice-selective NMR experiment (diffSe) was used to probe the penetration of the surfactant molecules into the poly(NIPAM) hydrogel. The experimental details are presented in [16]. The pulse sequence and the experimental setup dimensions are shown in Figure 5.4. In the slice-selective diffSe pulse sequence, the 180° pulse is sine shaped and has duration of 500 μs. The two G_1 gradients are for diffusion weighting, whereas the G_2 gradient is used for spatial encoding [112].

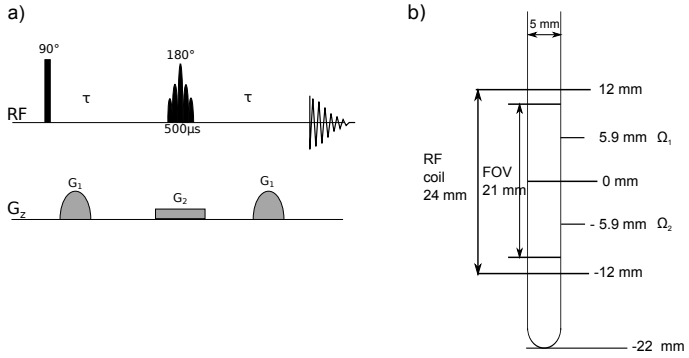

Figure 5.4: Schematic illustration of slice-selective diffusion experiment; (a) diffSe pulse sequence (b) experimental setup with dimensions. Ω_1 and Ω_2 represent the position of the slices at which the self-diffusion spectra were obtained.

Because of the RF coil shape, the self-diffusion coefficients from various z-positions (Ω_1 and Ω_2) obtained using the slice-selective diffSe NMR experiment were normalized to the

center of the RF coil, Ω_0 by using the following relationship:

$$D_s(\Omega_{1,2}) = D_s(\Omega_0) \times 1.09 \tag{5.1}$$

The above mentioned relationship was determined experimentally by measuring the D_s coefficient of sucrose in 10 mM solution as a function of z-position as shown in Figure 5.5.

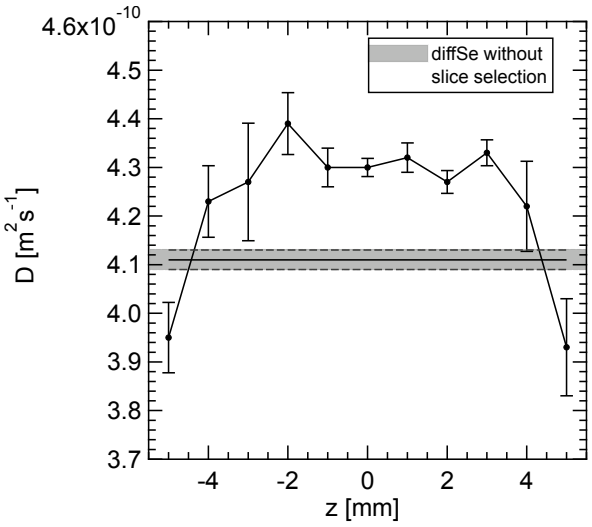

Figure 5.5: Self-diffusion coefficients as a function of the slice position. The gray rectangle symbolizes the self-diffusion coefficient measured using the same pulse sequence (diffSe) without the slice selection.

5.2.4 1D Chemical Shift Imaging (CSI)

In Paper II, the 1D Chemical Shift Imaging (CSI) experiment was used to follow the penetration of the surfactant molecules into P(NIPAM) hydrogel. The 1D chemical shift profiles were recorded using the pulse sequence presented in Figure 3.12 and the experimental setup shown in Figure 5.4b. Figure 5.6 shows an example of the chemical shift profiles of sucrose in 10 mM solution. Due to the shape of the RF coil, the signal decreases in intensity in the edges of the chemical shift profile. At the positions 10 mm > z > 8 mm and -10 mm < z < -8 mm the intensity of the signal is 0 because the measured volume is outside of the RF coil.

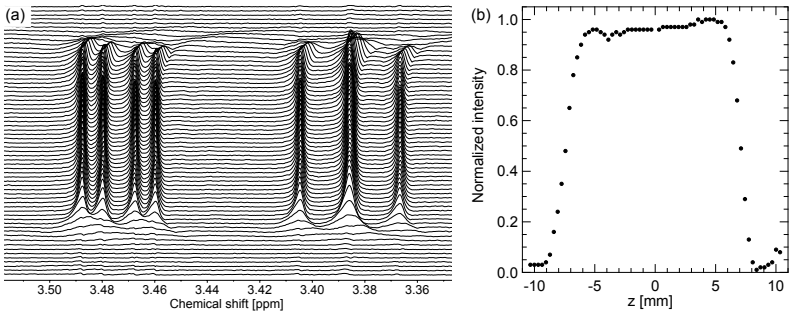

Figure 5.6: (a) Chemical shift image of 10 mM sucrose solution. (b) Chemical shift profile - normalized intensity plotted as a function of z-position.

5.3 MRI experiments

5.3.1 Multi-slice multi-echo (MSME)

In Paper III, the MSME sequence shown in Figure 5.7 was used to follow the effect of the elevated temperature on the structure of the P(NIPAM) hydrogel. A standard MSME protocol with 2.91 ms echo time (TE) and 700 ms repetition time (TR) was used to acquire multislice images. Image slice thickness was 2 mm and field of view (FOV) was 25×15 mm^2. 5 saggital slices were collected. The image pixel size was 64×64 giving the corresponding resolution of 391×234 μm. For obtaining the T_1-weighted images using MSME only the first echo is used as shown in Figure 3.11. The intensity of this echo will be T_1-weighted since TR has an intermediate value and TE is short.

T_2 relaxation time values were also measured using the MSME sequence with TR of 3631 ms and TE of 3 ms. The number of echo images was 100, and one repetition was used. The FOV was 12×12 mm^2 and with an acquisition matrix of 64×64 this provided a resolution of 188×188 μm. 12 axial slices were collected. For obtaining a series of T_2-weighted images using the MSME sequence multiple echoes are used together with a corresponding sampling of k-space. The echoes will be T_2-weighted with increasing echoes, as indicated in Figure 5.7, while TR is relatively long.

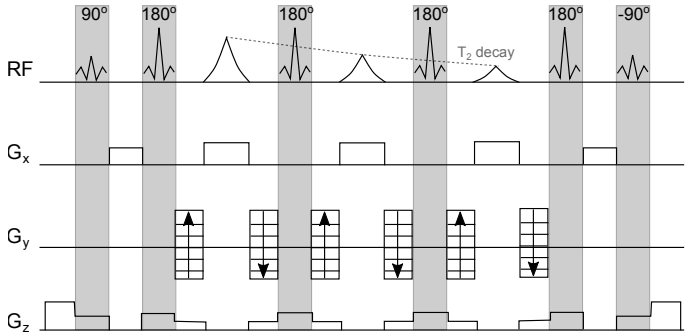

Figure 5.7: Pulse sequence of MSME.

5.3.2 Diffusion Tensor Imaging (DTI) with Echo Planar Imaging (EPI)

Diffusion Tensor Imaging (DTI) with Echo Planar Imaging (EPI) method combines the diffusion measurement with EPI to allow fast acquisition of diffusion data. In EPI, multiple lines of imaging data are acquired after a single RF excitation. As in a conventional spin echo sequence (Section 3.4), an DTI EPI sequence begins with 90° and 180° RF pulses. As shown in Figure 5.8 after the 180° RF pulse, the frequency-encoding G_x oscillates rapidly from a positive to a negative value, forming a train of gradient echoes [113]. Each echo is phase encoded differently by the phase-encoding G_y gradient pulses.

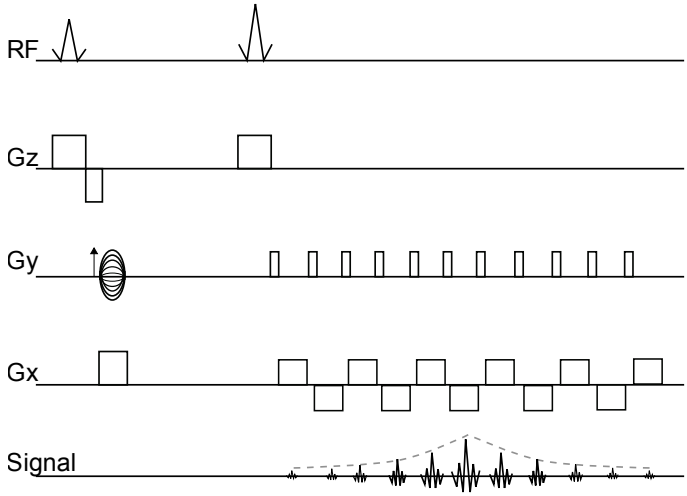

Figure 5.8: A pulse sequence for the DTI with EPI MRI experiment. Adapted from [113].

The DTI-EPI sequence was used with TE of 22 ms and TR of 3200 ms. The gradient pulses were applied with duration time (δ) of 3 ms and gradient separation (Δ) of 8.6 ms. A spatial

resolution of 63 $\times$ 133 μm was achieved by using a 12 $\times$ 12 mm^2 FOV and 192 $\times$ 90 image size. 12 axial slices were collected.

5.3.3 STimulated Echo Acquisition Mode (STEAM)

In Paper III, the localized spectra from rectangular voxels were obtained by using the STEAM pulse sequence shown in Figure 5.9 [86, 114, 115]. In STEAM method, three 90° RF pulses generate a simulated echo after the last 90° pulse with an identical delay to that between the first two 90° pulses. With the applied gradients, only signals undergoing three slice-selective pulses are refocused to create a desired stimulated echo from the voxel.

The STEAM pulse sequence was used to select two 6.5 $\times$ 6.5 $\times$ 1 mm^3 voxels located in the release medium and one 3 $\times$ 3 $\times$ 3 mm^3 voxel located in the hydrogel. Using the nomenclature of Paper III, the STEAM pulse sequence was applied with the following parameters: TE = 3 ms, TR = 4000 ms. The STEAM sequence was combined with variable power and optimized relaxation delay (VAPOR) water suppression.

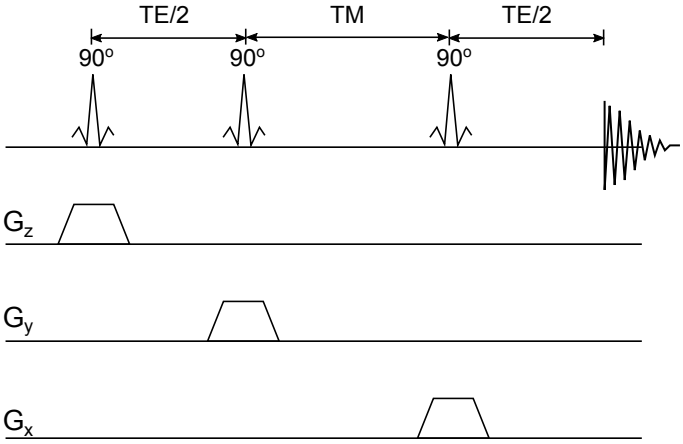

Figure 5.9: A schematic illustration of a STEAM pulse sequence. TE refers to the echo time and TM is the mixing time.

[Materials and Methods]

Chapter 6

Main results and discussion

The aims of this thesis were to (i) set up a reliable methodology for characterizing the mesh size of P(NIPAM)-based hydrogels, (ii) to investigate in detail mass transport processes in such hydrogels, and (iii) to establish new methods for measuring the release and penetration of secondary drug carriers from and into the model hydrogels. The results are presented in three scientific papers, labeled I to III.

Paper I reports a detailed comparison of the scaling of the mesh size (ξ) of chemically crosslinked P(NIPAM-co-AAc) hydrogels with crosslinker concentration (C_{cl}) determined by using three experimental methods: dynamic swelling, rheometry, and NMR self-diffusion of probe embedded in the hydrogels. The mesh sizes were found to exhibit strong power-law decay with increasing crosslinker concentration for all of the studied methods. The scaling function $\xi = kC_{cl}^{n}$ was introduced to describe the variation of mesh size with crosslinker concentration.

Paper II presents a novel NMR protocol to measure the transport of surfactant molecules in the model hydrogel, at microscopic and macroscopic scales, by combining 1D Chemical Shift Imaging (CSI) with slice-selective diffusion experiments. By applying our experimental protocol we were able to determine the mutual and self-diffusion coefficients of the surfactant in the non-equilibrium hydrogel-based system within the same short time frame. Furthermore, it was shown that the results obtained gave insight into structure-dependent diffusional behavior of surfactant molecules.

Paper III is dedicated to a MRI study of the temperature-induced shrinking of the P(NIPAM) hydrogel at 31°C and 40°C. The study revealed that the rate of hydrogel shrinking, reduction in water mobility, and the release of incorporated βCDs due to the volume phase

transition (VPT) are controlled by the destination temperature and the rate of heating of the model system.

6.1 Correlating the hydrogel mesh size with the crosslinker concentration (Paper I)

Several studies, listed in Table 6.1, investigated the effect of the crosslinker concentration on various properties of hydrogels. For all hydrogels in Table 6.1 an increase in crosslinker content resulted in decreased swelling ratio.

Table 6.1: Summary of studies of the effect of crosslinker concentration on hydrogel structural properties. The results obtained from equilibrium swelling experiments were recalculated using Equation 2.16.

Hydrogel type	Crosslinker	Crosslinker concentration [mM]	Method	Swelling degree	Reference
Poly(acrylamide-*co*-acrylic acid)	BIS*	0.011-0.024	Swelling	287.4-9.6	[116]
Poly(dimethyl acrylamide-co-stearyl acrylate)	BIS*	1.3-19.5	Rheology		[117]
			Swelling	1.5-1.4	
Poly(acrylic acid-co-methyl methacrylate)	BIS*	32.4-259.4	Swelling	0.9-0.7	[118]
			Rheology		
Polyethylene oxide	PETRA†	28.4-284.0	Swelling	6.0-1.3	[119]
Polyacrylamide	BIS*	0.1-1.3	Swelling	19.4-14.8	[120]
			Probe diffusion		
Carboxymethyl-cellulose and sodium alginate	BIS*	0.005-0.01	Swelling	70-35	[121]

* BIS = *N,N'*-Methylenebisacrylamide, † PETRA = Pentaerythritol tetraacrylate

There are a number of methods commonly used to characterize the influence of crosslinker concentration on hydrogel structure, among which the equilibrium swelling is the most widely used. However, the equilibrium swelling method is only helpful in determining the water content in the hydrogel, from which the mesh size can be calculated from Equations 2.14-2.16. However, it does not provide any information about other important parameters such as

crosslinking efficiency or homogeneity of the hydrogel.

As explained in Section 2.1.2, the mesh size of the hydrogels is directly proportional to the swelling degree, and thus decreases with increasing crosslinker concentration even though the polymer concentration is kept constant [116–121]. The classical theory relates the mesh size to polymer concentration in physical gels [122]:

$$\xi \approx \sqrt{\langle \bar{r_0}^2 \rangle} \left(\frac{C_p}{C^*} \right)^{-v/(3v-1)} \tag{6.1}$$

where C_p represents polymer concentration, C^* is the overlapping concentration, and v is the Flory exponent. The dependence of the hydrogel mesh size on the crosslinker content is not demonstrated in Equation 6.1. Thus, in Paper I we aimed to address the following research questions:

1. To what extent is determination of hydrogel mesh size dependent on the applied method?

2. How does the mesh size of the hydrogel scale with crosslinker concentration?

Three experimental methods were employed to characterize the effect of the crosslinker concentration (C_{cl}) on the hydrogels mesh size (ξ). These methods were: probe diffusion studied by PGSE NMR, dynamic swelling, and rheometry. The hydrogel mesh size calculated by using the aforementioned methods was found to be strongly model dependent, and decreases with increasing crosslinker concentration for all the methods applied. The mesh sizes were determined for hydrogels in two different states of hydration (swelling), namely the initial and equilibrium states. Hydrogel is in the initial swelling state just after crosslinking, before dialysis. The water content is the same as in the monomer blend before crosslinking. The hydrogel is in the equilibrium state after it has been incubated in excess solvent, and when the polymer-solvent interaction is balanced by the elastic retractive force of the polymer chains as explained in Section 2.1.1. The mesh size of the hydrogel in the initial state was measured using rheometry and dynamic swelling. The equilibrium swelling and probe diffusion experiments were conducted using hydrogel in equilibrium with solvent.

The scaling formula in Equation 6.2 was used to describe the differences in mesh sizes determined by the three methods.

$$\xi = k(C_{cl})^n \tag{6.2}$$

where C_{cl} is the crosslinker concentration. The resulting values of n for the dynamic swelling experiments, probe diffusion and rheology measurements are summarized in Table 6.2.

Table 6.2: The scaling component, n determined for swelling, rheology and probe diffusion methods at different hydration states of the hydrogel

Method	Scaling exponent, n	State
Swelling	-0.73 $\pm$ 0.05	Equilibrium
Swelling	-0.48 $\pm$ 0.05	Initial
Rheology	-0.18 $\pm$ 0.02	Initial
Rheology	-0.27 $\pm$ 0.02	Equilibrium *
Probe diffusion	-1.01. $\pm$ 0.30	Equilibrium

* Calculated with Equation 6.3.

Figure 6.1 shows the dependence of the hydrogel mesh size on the crosslinker concentration in the equilibrium state. For the two lowest crosslinker concentrations, the mesh sizes obtained from the probe diffusion and dynamic swelling experimens show the highest values, while the mesh sizes calculated from the rheology data are smaller. However, for the most crosslinked hydrogels, the results obtained using rheometry are larger than those calculated using probe diffusion and dynamic swelling. A detailed description of mesh size determination using dynamic swelling, rheometry and probe diffusion will be given in the following sections.

6.1.1 Swelling

As the basis for our studies the dependency of the hydrogel Q_m on the crosslinker concentration was investigated. The mesh size was calculated by measuring the Q_m factor (Equation 2.14-2.16) for both the initial and equilibrium states. The results are shown in Figure 6.2. Clearly, the mesh size of the hydrogel in the equilibrium state decreases from 65 nm to 7 nm as a result of a lower swelling degree with increasing crosslinker concentration. The difference between the mesh sizes obtained in the initial state and in the equilibrium state decreases at higher crosslinker concentration. The values of the scaling exponent were n = -0.73 $\pm$ 0.05 and n = -0.48 $\pm$ 0.05 for equilibrium and initial state, respectively.

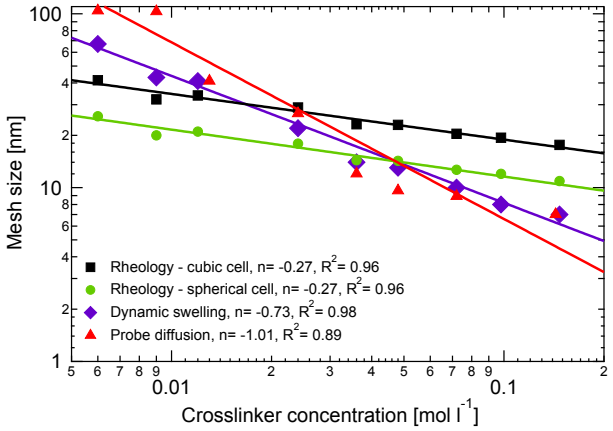

Figure 6.1: Comparison of the mesh sizes at equilibrium obtained using dynamic swelling, rheometry and probe diffusion PGSE NMR experiments. The function expressed in Equation 6.2 is fitted to the data [33].

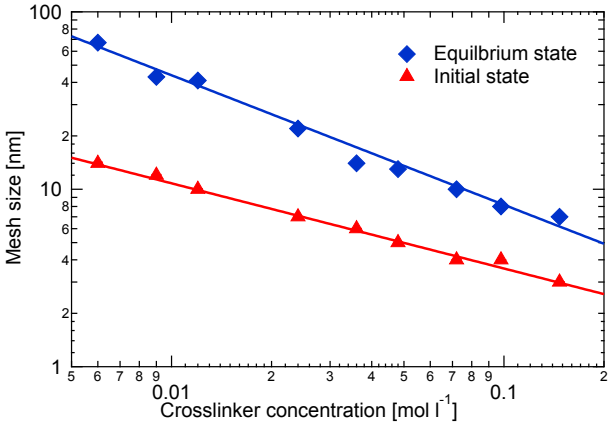

Figure 6.2: Mesh size of P(NIPAM-co-AAc) determined by swelling method as function of crosslinker concentration in the equilibrium state and in the initial state. The function expressed in Equation 6.2 is fitted to the data, which yields exponent (n) values of n = -0.73 $\pm$ 0.05 for the equilibrium state, and n = -0.48 $\pm$ 0.05 for the initial state [33].

6.1.2 Rheology

In the rheology measurement, the hydrogels were studied using frequency sweep measurements just after crosslinking (initial state). The plateau values of the G' were used to calculate the mesh sizes of the hydrogels. The G' values, which can serve as indicator of the structure rigidity, increase with crosslinker concentration. The mesh sizes were determined by using the

expressions in Equations 2.18 - 2.20 for cubic and sphere models. Figure 6.3 shows the dependence of mesh size on the crosslinker concentration determined using cubic and spherical models. The n exponent, obtained by fitting the results from the initial state of hydration to Equation 6.2, was -0.18 $\pm$ 0.02.

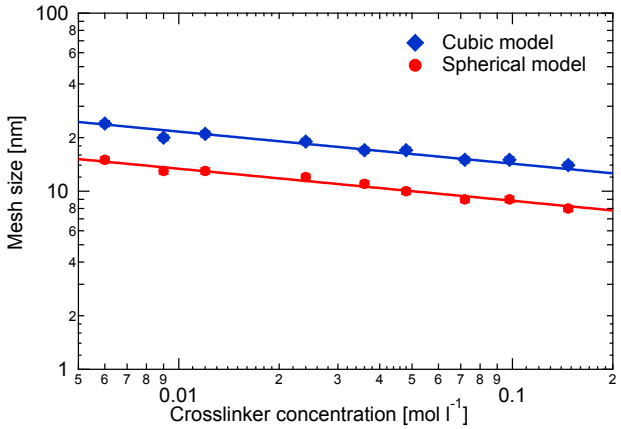

Figure 6.3: Mesh sizes obtained by the rheological measurements applying cubic and spherical models, are presented as a function of crosslinker concentration in the initial state. The function expressed in Equation 6.2 is fitted to the data, which yields exponent (n) values of n = -0.18 $\pm$ 0.02 [33].

As the hydrogel network expands isotropically during the swelling process, the values of G' in the initial state could be related to G' at the solvent equilibrium using the the following relation [26]:

$$G'_{eq} = \nu_{2s}^{\frac{1}{3}} G'_i \tag{6.3}$$

In Equation 6.3, G'_i is the elastic modulus in the initial state and G'_{eq} is the modulus in the equilibrium state. ν_{2s} holds the same meaning as in Equation 2.14. The fitting of the mesh sizes at equilibrium calculated from the rheology measurements using Equation 6.3 yields n = -0.27 $\pm$ 0.02.

6.1.3 Probe diffusion

In this part of the study, four dextrans with different molecular weights were used as probes. First, the probe diffusion in pure solvent (D_s^0) was determined in order to estimate its hydro-

dynamic radius (R_h) by Equation 2.17.

Figure 6.4 presents the dependence of the D_s^0 coefficient values on the molecular weight of the dextran.

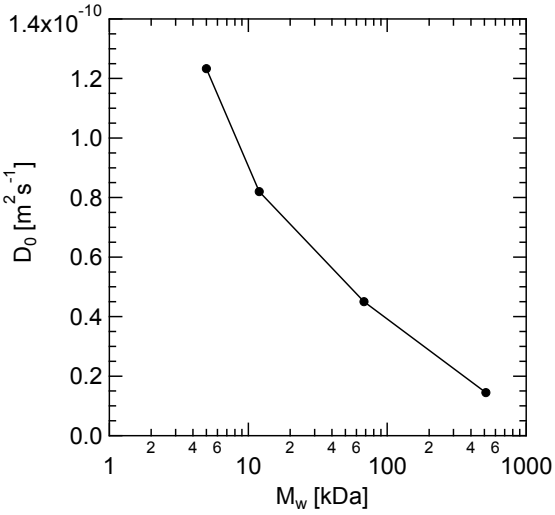

Figure 6.4: D_s^0 coefficients of dextrans used in aqueous solutions obtained by fitting Equation 3.19.

After determining the hydrodynamic radii of the dextrans, the probe diffusion in the hydrogel (D_s^{gel}) in the equilibrium state was studied. The diffusion of probe in hydrogels occurs within the water-filled regions in the space limited by the polymer chains. The mesh size of a hydrogel can be indirectly obtained by comparing the D_s^{gel} to the D_s^0. The restricted diffusivity of the probe can be expressed as the diffusion quotient ($\frac{D_s^{gel}}{D_s^0}$). In our study, the least restricted diffusion was detected for the smallest dextran molecule (M_w = 5 kDa) diffusing in the 0.012 mol L^{-1} crosslinked hydrogel. The corresponding $\frac{D_s^{gel}}{D_s^0}$ ratio was 0.98 indicating that the diffusion is almost free (as in Figure 4.2a). On the other hand, the most restricted diffusion was measured using the largest dextran molecules (M_w = 513 kDa) in the 0.036 mol L^{-1} crosslinked hydrogel. The respective diffusion quotient was 0.36. There are many models relating the restricted diffusion of the probes in the hydrogel with the mesh size [30]. In this study, the mesh size of the hydrogel was calculated by Equation 4.10. The results are presented in Figure 6.5. The fitting of the mesh sizes obtained from the probe diffusion experiment by the function expressed in Equation 6.2 yields n values of n = -1.01 $\pm$ 0.30.

Probe diffusion experiments were found to be very sensitive to the size of the diffusing

molecules [123] which can lead to the overestimation of the mesh size. The study revealed that the ratio between the R_h of the probe and the ξ of the hydrogel is critical for the validity of the mesh size determination by the diffusion NMR.

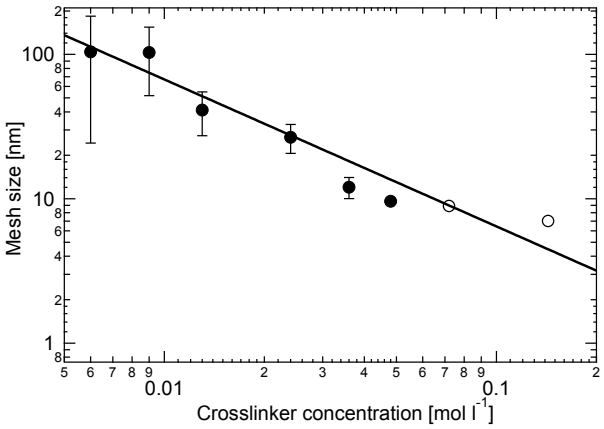

Figure 6.5: Mesh sizes obtained from the PGSE NMR experiments using dextrans with different molecular weight as probes. The function expressed in Equation 6.2 is fitted to the data, which yields exponent (n) values of n = -1.01 $\pm$ 0.30. The last two data points marked by hollow circles were not used for the fitting of the power law function [33].

6.2 Investigating structure-dependent diffusion in hydrogels (Paper II)

The study in Paper I revealed a strong dependence between the hydrogel mesh size (controlled by the crosslinker concentration) and the self-diffusion of the embedded probe. We decided to continue the investigation of the diffusion processes using the model system from Paper I with some alterations:

1. One crosslinker concentration (0.024 M DAT) was chosen based on the results obtained in Paper I. The mesh size of the hydrogel prepared with 0.024 M DAT was 22 nm. The probe diffusion experiment conducted in Paper I revealed that the mesh size of this hydrogel is appropriate for studying diffusion of the probes with the R_h from 1 to 14 nm.

2. The model dextran molecules used as probes were replaced with surfactant. In this case, surfactant micelles can act as drug carriers as they can solubilize poorly soluble drugs and thus increase their bioavailability. Optimally, a surfactant used in this

study would be non-ionic. The CMC of the non-ionic surfactants are in the range of μM. Since one of the main motivations of the Paper II was to detect changes in the concentration-dependent surfactant structure, non-ionic surfactant were not considered since their CMC values may be too low to be detected using NMR methodology. Therefore, a cationic surfactant (C_{14}TAB) with CMC of 3.8 mM was chosen as its CMC is high enough to detect changes in concentration-dependent structures using diffusion NMR.

3. To simplify the model system, acrylic acid was excluded in the following investigation. The swelling test prepared prior to this study shown, as expected, that the mesh size of the P(NIPAM) hydrogel is smaller than in the case of the P(NIPAM-co-AAc) with the same crosslinker concentration. The following subsection explains the effect of acrylic acid on the mesh size.

Effect on acrylic acid addition on the mesh size

In Paper I the studied hydrogel consisted of 95 mol% P(NIPAM) and 5 mol% P(AAc). In the following papers P(AAc) was not added to the hydrogel blend. In this section the effect of adding 5 mol% P(AAc) on hydrogel swelling will be discussed.

As shown in Table 6.3, P(NIPAM)-based hydrogel swelling was improved by incorporation of AAc. Comparing to the samples prepared with only P(NIPAM), the equilibrium mass swelling ratios of the hydrogels containing 5 mol% AAc were 17, 10 and 8 times higher for the hydrogels crosslinked with 0.012 M, 0.024 M and 0.048 M crosslinker, respectively.

Table 6.3: Equilibrium mass swelling ratios, Q_m and respective mesh sizes, ξ^{SW} determined for hydrogels consisting of P(NIPAM-*co*-AAc) and P(NIPAM) prepared with different crosslinker concentrations, $C_{crosslinker}$. The hydrogels were swollen in distilled H_2O.

$C_{crosslinker}$ [mol L^{-1}]	Q_m (P(NIPAM-*co*-AAc)) [a.u.]	ξ^{SW} (P(NIPAM-*co*-AAc)) [nm]	Q_m (P(NIPAM)) [a.u.]	ξ^{SW}(P(NIPAM)) [nm]
0.012	932	40	54	16
0.024	429	22	43	11
0.048	217	13	27	7

The addition of the ionizable groups of AAc into the polymer structure lead to the increased swelling capacity of the hydrogel. Carboxylic groups of AAc are ionized above the pKa value

(4.35 [124]) initiating ionic repulsion between negative COO^- groups, resulting in polymer network expansion and increased solvent absorption. Similar phenomenon was described by Zhang et al. [125] and Cuggino et al. [124].

Experimental design

Kwak et al. [101] described the differences between the release and the penetration experiments with large and small reservoirs measured by PFGSE NMR and 1D ^{31}P NMR imaging. Based on these results, we decided to use the simplified penetration experiment with confined reservoir as shown in Figure 6.6. The surfactant-free P(NIPAM) hydrogel crosslinked with 0.024 M DAT was placed in the bottom of the 5 mm o.d. NMR tube. The same amount of the 50 mM C_{14}TAB solution was added on top of the hydrogel.

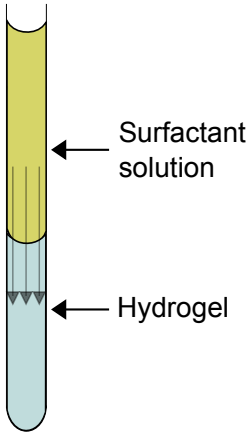

Figure 6.6: Illustration of the experimental setup. The gray arrows indicate the direction of the diffusion of the surfactant molecules.

1D CSI pulse sequence described in Section 3.6.3 was used together with slice-selective diffusion (diffSe) pulse sequence described in Section 5.2.3 to monitor the penetration of the surfactant molecules in the P(NIPAM) hydrogel. The detailed information about the dimensions of the RF coil and the FOV are presented in Figure 5.4.

The evolution of the intensity of the surfactant and hydrogel signals was followed with 1D chemical shift images as shown in Figure 6.7. Results presented in Figure 6.7a indicate swelling of the hydrogel due to the interaction with the surfactant molecules. The development of the surfactant signal shown in Figure 6.7b reveals the diffusion from the solution to the hydrogel. This time- and position-dependence of the surfactant molecules were used for the

calculations of the D_m by:

$$\frac{C_{gel}}{C_0} = erfc\frac{z}{2\sqrt{D_m t}} \tag{6.4}$$

In Equation 6.4, C_{gel} refers to the surfactant concentration in the hydrogel, C_0 is the initial concentration of the surfactant in the solution (50 mM), z is the position in the NMR tube, and t is time.

The calculated D_m for this system was $7.7 \pm 0.5 \times 10^{-11}$ m^2s^{-1}.

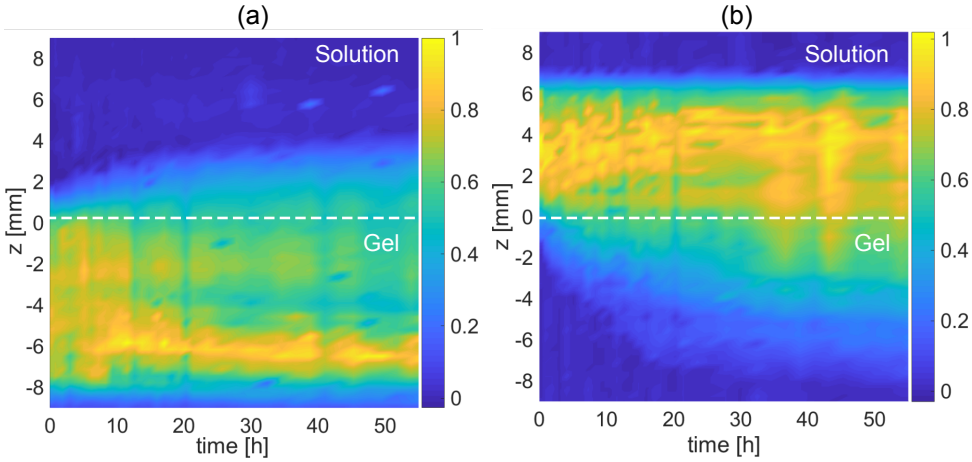

Figure 6.7: (a) Polymer and (b) surfactant peak areas obtained via integration, plotted as functions of the vertical position in the NMR tube. The dashed line indicated the position of the initial interface. The color scale shows the intensity [16].

The self-diffusion of the surfactant molecules was measured at two positions, in the solution and in the hydrogel. The time-dependent evolution of the surfactant self-diffusion coefficients is presented in Figure 6.8. The surfactant self-diffusion coefficient measured in the solution (D_s^{sln}) remained constant during the entire experiment at $6.7 \pm 0.3 \times 10^{-11}$ m^2s^{-1}. In the hydrogel, the self-diffusion coefficient (D_s^{gel}) decreased with time reaching a plateau after 45h at $6.6 \pm 0.5 \times 10^{-11}$ m^2s^{-1}.

Combining the results obtained from 1D CSI experiments with the self-diffusion of the surfactant in the solution and in the hydrogel in Figure 6.9, one can gain a valuable insight into the structure-dependent transport properties. Knowing that the CMC of the C_{14}TAB surfactant is 3.8 mM, it is easy to relate the surfactant self-diffusion to the structure of the surfactant. Thus, it was found that in the beginning of the experiment, the surfactant diffused into the hydrogel in the form of the monomers, and after reaching the CMC in the hydrogel, self-assembles into the micelles [126]. Furthermore, the R_h sizes of the monomers and micelles were estimated

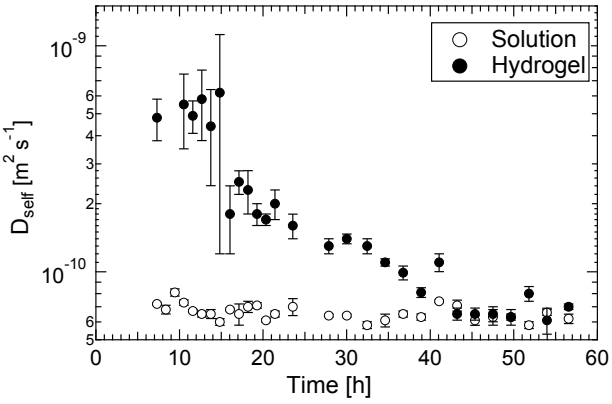

Figure 6.8: The time-dependent evolution of the diffusion coefficient of the surfactant in solution and in hydrogel [16].

using Equations 2.17 and 4.1 to be 0.4 $\pm$ 0.1 nm and 3.0 $\pm$ 0.2 nm, respectively. Similarly to the results obtained in Paper 1, the diffusion quotient of $\frac{D_s^{gel}}{D_s^{sln}}$ reflects the obstruction of the diffusion path originating from the hydrogel network.

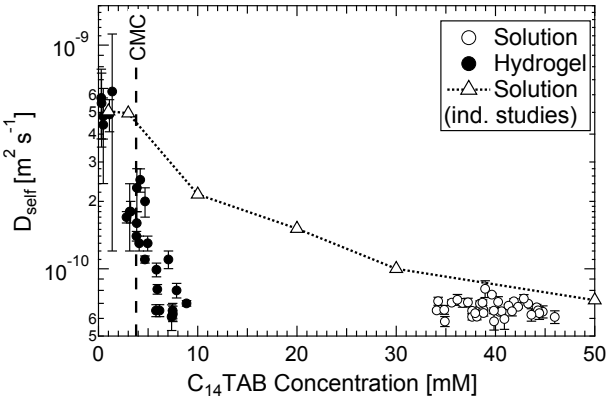

Figure 6.9: Combination of the 1D CSI experiment with slice selective self-diffusion measurement. The self-diffusion coefficient of the surfactant in the solution and in the hydrogel shown as a function of the surfactant concentration [16].

It was found that the slice-selective self-diffusion experiments alone provided a more detailed picture of the release process than the 1D CSI, allowing the identification of surfactant forms. Moreover, the interactions within the hydrogel network were also identified using the slice-selective self-diffusion experiments.

6.3 Investigating volume phase transition in hydrogel using MRI (Paper III)

As described in Section 2.1.4, P(NIPAM) hydrogels swollen in H_2O undergoes VPT at 34°C [6, 7]. Due to this property, P(NIPAM) hydrogels find application in drug delivery systems, as the VPTT is close to the body temperature of 37°C. Therefore, we decided to investigate the changes in water mobility in the P(NIPAM) hydrogel as a function of the temperature as well as the release of the βCDs from the hydrogel.

The model hydrogel was chosen to be of the same type as used in Paper II. However, some alterations listed here were performed.

1. In order to simplify the experiment, the surfactant molecules, which show concentration-dependent structure alterations, were replaced by βCDs. The estimated R_h of the βCDs is of 0.8 nm.

2. Since the mesh size of the hydrogel used in Paper II (crosslinked with 0.024 M DAT) was 11 nm, the ratio between the hydrogel ξ and the R_h of βCD molecules could be too large to detect any hindrance of the βCD mobility due to the polymer network. Therefore, we chose to use a hydrogel with smaller mesh size. Thus, the P(NIPAM) hydrogel studied in Paper III was crosslinked with 0.048M DAT (ξ = 7 nm).

3. Initial test were performed using the diffBB probe (as in Papers I and II). However, due to the construction of the probe, it was impossible to follow the changes in hydrogel structure. Thus, the study was performed using the micro imaging probe.

4. In order to mimic the release measurements performed conventionally, a release experiment was performed instead of the penetration experiment in Paper II.

Experimental setup

In Paper III the hydrogel containing βCD molecules was placed at the bottom of the NMR tube as shown in Figure 6.10, followed by the addition of the βCD-free water on top of the hydrogel. The temperature was elevated to 31°C or 40°C by immediate temperature-jump (T-jump) or slow heating with a rate of 1°C per 4 minutes. In the T-jump experiments the sample was inserted into the the thermally equilibrated microimaging probe.

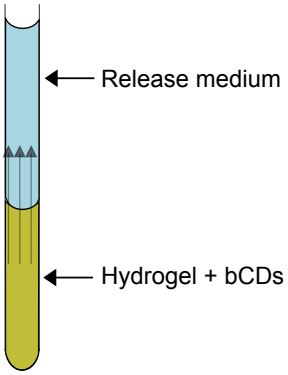

Figure 6.10: Illustration of the experimental setup. The gray arrows indicate the direction of the diffusion of the βCD molecules.

The structure of the hydrogel was monitored using images obtained using the MSME pulse program (Section 5.3.1). The hydrogel shrinking ratio is defined as an area of the hydrogel measured at various sampling times (A) divided by the initial area of the hydrogel (A_0). The A/A_0 ratio as a function of time is shown in Figure 6.11. As expected, the P(NIPAM) hydrogels shrink moderately at 31°C. However, as the temperature is below the VPTT of this polymer network, the hydrogel does not collapse. When the temperature is elevated to 40°C, the hydrogel collapses as its A/A_0 ratio decreases to approximately 20 % of the initial value. Interestingly, at 40°C a difference in the shrinking rate between the T-jump (Figure 6.11a) and the slow heating (Figure 6.11b) can be observed.

As shown in Figure 6.12, the structure of the hydrogel also affects the water T_2 relaxation. The data show that T_2 decreases with decreasing A/A_0 ratio.

The release of βCD molecules from the P(NIPAM) hydrogels was also found to be temperature-dependent (Figure 6.13). The fastest release of the βCD molecules was measured at 40°C after the T-jump, while the slowest release followed the T-jump to 31°C. The results correlate well with the kinetics of the hydrogel shrinking presented in Figure 6.11. It was found that the hydrogel with the fastest shrinking rate releases the highest amount of βCD molecules.

Water diffusion in the hydrogel was also measured. However, this measurement did not exhibit the same level of sensitivity to changes in hydrogel structure as T_2 relaxation and βCD release.

To conclude, at temperatures above the VPTT of the P(NIPAM) hydrogel, the release of βCD molecules from the hydrogel was found to correlate well with the shrinking kinetics.

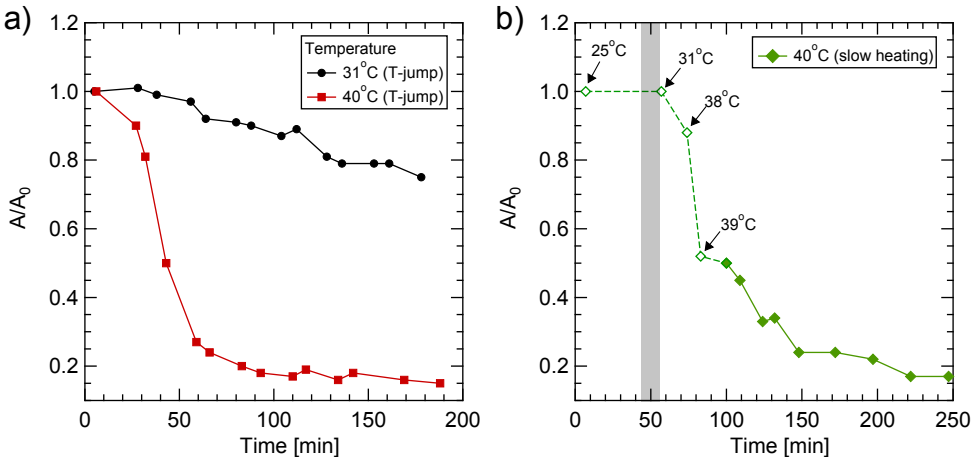

Figure 6.11: Time-dependence of the A/A_0 ratio of the hydrogels in water at (a) 31°C and 40°C obtained by the T-jump, (b) 40°C obtained by the slow heating. In (b) empty symbols refer to the data points recorded during the heating of the hydrogel (transition temperatures). The transition temperatures are indicated with arrows. The gray rectangle represents the change of the temperature of the BCU20 cooling device.

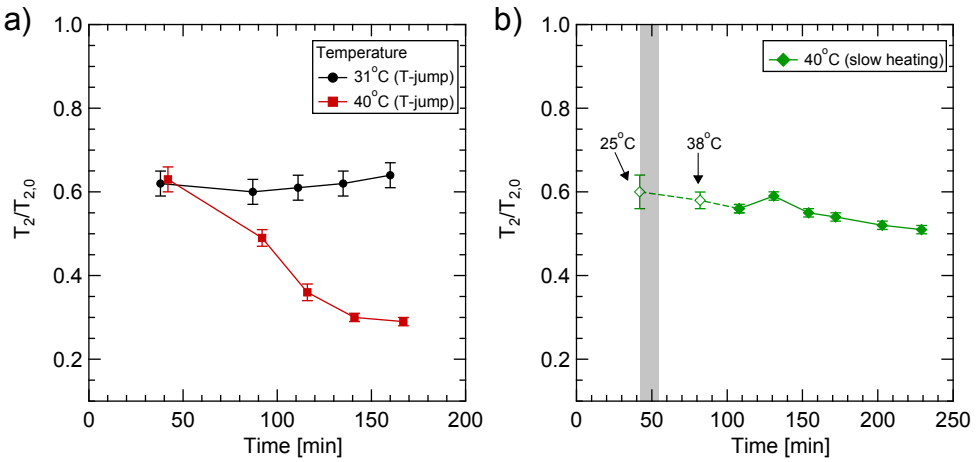

Figure 6.12: Time-dependence of the water T_2 relaxation times measured in hydrogel at (a) 31°C and 40°C obtained by the T-jump, (b) 40°C obtained by the slow heating. In (b) empty symbols refer to the data points recorded during the heating of the hydrogel (transition temperatures). The transition temperatures are indicated with arrows. The gray rectangle represents the change of the temperature of the BCU20 cooling device.

For the experiment performed at temperature below the VPTT, the release of βCD molecules increased linearly. Water T_2 relaxation was found to be strongly dependent on the shrinking degree of the hydrogel. The results presented in Paper III provide valuable insight into temperature-dependent behavior of the P(NIPAM) hydrogel with βCD moieties in terms of

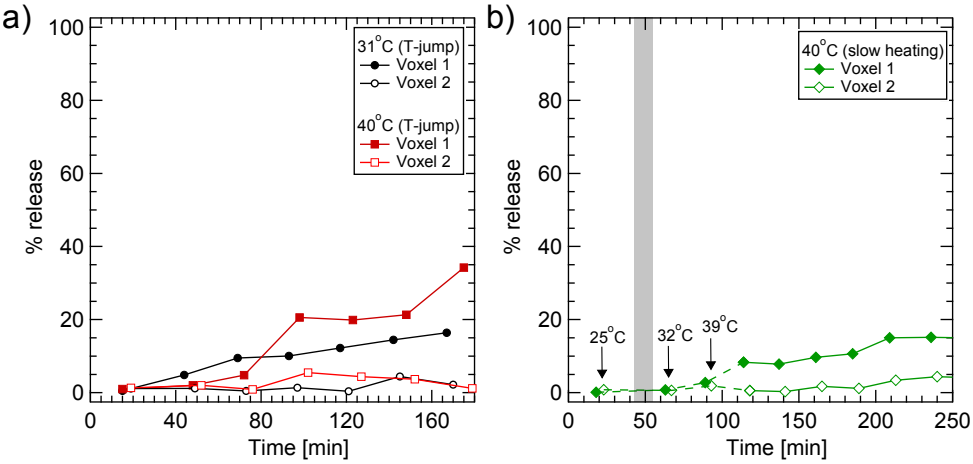

Figure 6.13: Thermally induced βCD release from the P(NIPAM) hydrogel measured in release medium in voxel 1 and 2. All the values are normalized against the initial βCD concentration determined in the hydrogel. Graph (a) refers to 31°C and 40°C obtained by the T-jump, graph (b) represents the data measured at 40°C obtained by the slow heating. In (b) the dashed lines refer to the data points recorded at the transition temperatures, between 25°C and 40°C. The transition temperatures are indicated with arrows. The gray rectangle represents the change of the temperature of the BCU20 controlling device.

water T_2 relaxation and release of embedded βCD molecules.

[Main results and discussion]

Chapter 7

Concluding remarks

NMR spectroscopy and MRI are powerful methods in determining molecular mobility in model hydrogel systems. In this dissertation, various NMR methods provided information about probe mobility in hydrogels in equilibrium (Paper I) and non-equilibrium (Papers II and III) states, revealing information about the microscopic structure of hydrogels.

The findings in Paper I revealed strong scaling of the mesh size with crosslinker concentration, as confirmed by dynamic swelling, rheometry and diffusion NMR experiments. In general, the mesh sizes obtained using diffusion NMR were larger than the results from the dynamic swelling measurements. The results obtained from dynamic swelling and diffusion NMR were in good agreement with theoretical predictions. However, the results obtained using rheometry revealed possible limitations with regards to application of the rubber elasticity theory, as the mesh sizes calculated from the storage modulus of the hydrogels were significantly different from those obtained using the two other methods. Further investigations are necessary to explain the differences in mesh sizes obtained using rheology and dynamic swelling in hydrogel systems. Additionally, the results of the diffusion NMR experiments showed the dependence of the probe molecular size on the measured mesh size which should be properly addressed when using this method. Furthermore, by following the probe diffusion in various hydrogels, non-uniformity and inefficiency in the crosslinking of the network was detected. Additional diffusion experiments could be performed in order to map the extent of crosslinking efficiency issues in this hydrogel system.

In Paper II, correlation of the chemical shift images with localized self-diffusion measurements gave insight into the structure-dependent diffusional behavior of surfactant molecules in the hydrogel. The combination of the 1D Chemical Shift Imaging (CSI) and slice selec-

tive NMR diffusion methods enabled us to follow the swelling of the hydrogel, as well as the molecular transport in the hydrogel-surfactant system. This NMR protocol may be further implemented in release studies where hydrophobic drug is solubilized in surfactant micelles and embedded in the hydrogel. In addition to application to study various DDS, our experimental approach may be useful in investigating concentration dependent structures at the interfaces between two immiscible liquids. Therefore, further work on developing the experimental part of this NMR protocol could be of interest.

In Paper III, the results reveal correlation between the kinetics of shrinking of the thermosensitive hydrogel system as a result of the VPT, the T_2 relaxation, and the release of the βCD molecules embedded in the hydrogel. Concerning the study of the VPT, it could be beneficial to establish the explanation for the differences between the sensitivity of the water T_2 relaxation measurements and self-diffusion in the collapsing hydrogel. Also, it would be of interest to study the phase transition in various hydrogel-systems as well as under different thermal conditions.

With the studies presented in Papers I-III we were able to establish the relationship between the mesh size of the hydrogel and the crosslinker content, as well as to correlate the structural properties of the hydrogels and the diffusional behavior of such model systems. NMR and MRI techniques were proven to be of great use in improving the experimental procedures to characterize the drug release from hydrogels.

[Conclusions and further work]

Bibliography

[1] J.F. Coelho, P.C. Ferreira, P. Alves, R. Cordeiro, A.C. Fonseca, J.R. Góis, and M.H. Gil. Drug delivery systems: Advanced technologies potentially applicable in personalized treatments. *EPMA journal*, 1(1):164–209, 2010.

[2] A. K. Bajpai, S. K. Shukla, S. Bhanu, and S. Kankane. Responsive polymers in controlled drug delivery. *Prog. Polym. Sci.*, 33(11):1088–1118, 2008.

[3] N.A. Peppas, P. Bures, W. Leobandung, and H. Ichikawa. Hydrogels in pharmaceutical formulations. *Eur. J. Pharm. Biopharm.*, 50(1):27 – 46, 2000.

[4] A.S. Hoffman. Hydrogels for biomedical applications. *Adv. Drug Delivery Rev.*, 54(1): 3–12, 2002.

[5] E. Caló and V.V. Khutoryanskiy. Biomedical applications of hydrogels: A review of patents and commercial products. *Eur. Polym. J.*, 65:252–267, 2015.

[6] Y. Hirokawa and T. Tanaka. Volume phase transition in a nonionic gel. *J. Chem. Phys.*, 81(12):6379–6380, 1984.

[7] M. Shibayama, T. Tanaka, and C.C. Han. Small angle neutron scattering study on poly(n-isopropyl acrylamide) gels near their volume-phase transition temperature. *J. Chem. Phys.*, 97(9):6829–6841, 1992.

[8] M. Pekař. Hydrogels with micellar hydrophobic (nano) domains. *Front. Mater.*, 1:35, 2015.

[9] M.D. Mantle. Nmr and mri studies of drug delivery systems. *Curr. Opin. Colloid Interface Sci*, 18(3):214–227, 2013.

[10] M.D. Mantle. Quantitative magnetic resonance micro-imaging methods for pharmaceutical research. *Int. J. Pharm.*, 417(1-2):173–195, 2011.

[11] S.J. Park and K.S. Kim. Investigation of drug delivery behaviors by nmr spectroscopy. *Choudhary, M.I. (Ed.). Structure–activity relationship studies in drug development by NMR spectroscopy*, 1:36, 2011.

[12] S. Baumgartner, G. Lahajnar, A. Sepe, and J. Kristl. Investigation of the state and dynamics of water in hydrogels of cellulose ethers by 1 h nmr spectroscopy. *AAPS PharmSciTech*, 3(4):86, 2002.

[13] R. Barbieri, M. Quaglia, M. Delfini, and E. Brosio. Investigation of water dynamic behaviour in poly (hema) and poly (hema-co-dhpma) hydrogels by proton t2 relaxation time and self-diffusion coefficient nmr measurements. *Polymer*, 39(5):1059–1066, 1998.

[14] Y.E. Shapiro. Structure and dynamics of hydrogels and organogels: An nmr spectroscopy approach. *Prog. Polym. Sci.*, 36(9):1184–1253, 2011.

[15] E.N. Dunmire, A.M. Plenys, and D.F. Katza. Spectrophotometric analysis of molecular transport in gels. *J. Controlled Release*, 57(2):127–140, 1999.

[16] M.A. Wisniewska and J.G. Seland. Investigating structure-dependent diffusion in hydrogels using spatially resolved nmr spectroscopy. *J. Colloid Interface Sci.*, 533:671–677, 2019.

[17] O. Wichterle and D. Lim. Hydrophilic gels for biological use. *Nature*, 185(4706): 117–118, 1960.

[18] J. Berger, M. Reist, J.M. Mayer, O. Felt, N.A. Peppas, and R. Gurny. Structure and interactions in covalently and ionically crosslinked chitosan hydrogels for biomedical applications. *Eur. J. Pharm. Biopharm.*, 57(1):19–34, 2004.

[19] D. Buenger, F. Topuz, and J. Groll. Hydrogels in sensing applications. *Prog. Polym. Sci.*, 37(12):1678–1719, 2012.

[20] W. Hu, Z. Wang, Y. Xiao, S. Zhang, and J. Wang. Advances in crosslinking strategies of biomedical hydrogels. *Biomater. Sci.*, 7(3):843–855, 2019.

[21] F. Ullah, M.B.H. Othman, F. Javed, Z. Ahmad, and H.M. Akil. Classification, processing and application of hydrogels: A review. *Mater. Sci. Eng. C*, 57:414–433, 2015.

[22] N.A. Peppas. Hydrogels and drug delivery. *Curr. Opin. Colloid Interface Sci*, 2(5): 531–537, 1997.

[23] P.J. Flory and J. Rehner. Statistical mechanics of cross-linked polymer networks II. swelling. *J. Chem. Phys.*, 11(11):521–526, 1943.

[24] K.F. Arndt, F. Krahl, S. Richter, and G. Steiner. *Swelling-Related Processes in Hydrogels*, pages 69–136. Springer Berlin Heidelberg, Berlin, Heidelberg, 2010. ISBN 978-3-540-75645-3.

[25] P.J. Flory and J. Rehner. Statistical mechanics of cross-linked polymer networks i. rubberlike elasticity. *J. Chem. Phys.*, 11(11):512–520, 1943.

[26] L.R.G. Treloar. *The physics of rubber elasticity*. Oxford University Press, USA, 1975.

[27] J. Li and D.J. Mooney. Designing hydrogels for controlled drug delivery. *Nat. Rev. Mater.*, 1(12):16071, 2016.

[28] M.E. Young, P.A. Carroad, and R.L. Bell. Estimation of diffusion coefficients of proteins. *Biotechnology and Bioengineering*, 22(5):947–955, 1980.

[29] W.S. Price. *NMR Studies of Translational Motion*. Cambridge University Press, 2009.

[30] B. Amsden. Solute diffusion within hydrogels. mechanisms and models. *Macromolecules*, 31(23):8382–8395, 1998.

[31] A. Bertz, S. Wöhl-Bruhn, S. Miethe, B. Tiersch, J. Koetz, M. Hust, H. Bunjes, and H. Menzel. Encapsulation of proteins in hydrogel carrier systems for controlled drug delivery: Influence of network structure and drug size on release rate. *J Biotechnol*, 163 (2):243–249, 2013.

[32] N.A. Peppas and E.W. Merrill. Crosslinked poly(vinyl alcohol) hydrogels as swollen elastic networks. *J. Appl. Polym. Sci.*, 21(7):1763–1770, 1977.

[33] M.A. Wisniewska, J.G. Seland, and W. Wang. Determining the scaling of gel mesh size with changing crosslinker concentration using dynamic swelling, rheometry, and PGSE NMR spectroscopy. *J. Appl. Polym. Sci.*, 135(45):46695, 2018.

[34] J. Lei, C. Mayer, V. Freger, and M. Ulbricht. Synthesis and characterization of poly(ethylene glycol) methacrylate based hydrogel networks for anti-biofouling applications. *Macromol. Mater. Eng.*, 298(9):967–980, 2012.

[35] L. Pescosolido, L. Feruglio, R. Farra, S. Fiorentino, I. Colombo, T. Coviello, P. Matricardi, W. E. Hennink, T. Vermonden, and M. Grassi. Mesh size distribution determination of interpenetrating polymer network hydrogels. *Soft Matter*, 8(29):7708, 2012.

[36] M. Wallace, D.J. Adams, and J.A. Iggo. Analysis of the mesh size in a supramolecular hydrogel by pfg-nmr spectroscopy. *Soft Matter*, 9(22):5483, 2013.

[37] D.J. Waters, K. Engberg, R. Parke-Houben, L. Hartmann, C.N. Ta, M.F. Toney, and C.W. Frank. Morphology of photopolymerized end-linked poly(ethylene glycol) hydrogels by small-angle x-ray scattering. *Macromolecules*, 43(16):6861–6870, 2010.

[38] E.M. Saffer, M.A. Lackey, D.M. Griffin, S. Kishore, G.N. Tew, and S.R. Bhatia. Sans study of highly resilient poly(ethylene glycol) hydrogels. *Soft Matter*, 10(12):1905, 2014.

[39] H.M. James and E. Guth. Theory of the increase in rigidity of rubber during cure. *J. Chem. Phys.*, 15(9):669–683, 1947.

[40] Y. Gnanou, G. Hild, and P. Rempp. Molecular structure and elastic behavior of poly(ethylene oxide) networks swollen to equilibrium. *Macromolecules*, 20(7):1662–1671, 1987.

[41] L. Haggerty, J.H. Sugarman, and R.K. Prud'homme. Diffusion of polymers through polyacrylamide gels. *Polymer*, 29(6):1058–1063, 1988.

[42] J. Schurz. Rheology of polymer solutions of the network type. *Prog. Polym. Sci.*, 16(1): 1–53, 1991.

[43] M.C. Koetting, J.T. Peters, S.D. Steichen, and N.A. Peppas. Stimulus-responsive hydrogels: Theory, modern advances, and applications. *Mater. Sci. Eng. R Rep.*, 93:1 – 49, 2015.

[44] J.S. Scarpa, D.D. Mueller, and I.M. Klotz. Slow hydrogen-deuterium exchange in a non-.alpha.-helical polyamide. *J. Am. Chem. Soc.*, 89(24):6024–6030, 1967.

[45] S. Fujishige, K. Kubota, and I. Ando. Phase transition of aqueous solutions of poly(n-isopropylacrylamide) and poly(n-isopropylmethacrylamide). *J. Phys. Chem.*, 93(8): 3311–3313, 1989.

[46] G.A. Vidulich, D.F. Evans, and R.L. Kay. The dielectric constant of water and heavy water between 0 and 40. degree. *J. Phys. Chem.*, 71(3):656–662, 1967.

[47] C. Boutris, E.G. Chatzi, and C. Kiparissides. Characterization of the lcst behaviour of aqueous poly(n-isopropylacrylamide) solutions by thermal and cloud point techniques. *Polymer*, 38(10):2567–2570, 1997.

[48] T.Y. Wu, A.B. Zrimsek, S.V. Bykov, R.S. Jakubek, and S.A. Asher. Hydrophobic collapse initiates the poly(n-isopropylacrylamide) volume phase transition reaction coordinate. *J. Phys. Chem. B*, 122(11):3008–3014, 2018.

[49] A. Fahr and X. Liu. Drug delivery strategies for poorly water-soluble drugs. *Expert Opin. Drug Deliv.*, 4(4):403–416, 2007.

[50] K. Holmberg, B. Jönsson, B. Kronberg, and B. Lindman. *Surfactants and Polymers in Aqueous Solution*. John Wiley & Sons, Ltd, 2nd edition, 2003.

[51] M. Malmsten, editor. *Surfactants and Polymers in Drug Delivery*. CRC Press, 2002.

[52] G. Tiwari, R. Tiwari, and A.K. Rai. Cyclodextrins in delivery systems: Applications. *J. Pharm. Bioallied Sci.*, 2(2):72, 2010.

[53] T. Loftsson and M.E. Brewster. Pharmaceutical applications of cyclodextrins. 1. drug solubilization and stabilization. *J. Pharm. Sci.*, 85(10):1017 – 1025, 1996.

[54] V.J. Stella, V.M. Rao, E.A. Zannou, and V. Zia. Mechanisms of drug release from cyclodextrin complexes. *Adv. Drug Delivery Rev.*, 36(1):3–16, 1999.

[55] K. Sreenivasan. Synthesis and evaluation of β-cyclodextrin-2-hydroxyethyl methacrylate copolymer as a novel adsorbent. *Polym. Int.*, 42(1):22–24, 1997.

[56] T. Nozaki, Y. Maeda, K. Ito, and H. Kitano. Cyclodextrins modified with polymer chains which are responsive to external stimuli. *Macromolecules*, 28(2):522–524, 1995.

[57] J. Li, X. Li, Z. Zhou, X. Ni, and K.W. Leong. Formation of supramolecular hydrogels induced by inclusion complexation between pluronics and α-cyclodextrin. *Macromolecules*, 34(21):7236–7237, 2001.

[58] L.C. Cesteros, C.A. Ramírez, A. Peciña, and I. Katime. Synthesis and properties of hydrophilic networks based on poly(ethylene glycol) andβ-cyclodextrin. *Macromol. Chem. Phys.*, 208(16):1764–1772, 2007.

[59] L. Wei, C. Cai, J. Lin, and T. Chen. Dual-drug delivery system based on hydrogel/micelle composites. *Biomaterials*, 30(13):2606–2613, 2009.

[60] H.D. Wang, L.Y. Chu, X.Q. Yu, R. Xie, M. Yang, D. Xu, J. Zhang, and L. Hu. Thermosensitive affinity behavior of poly (n-isopropylacrylamide) hydrogels with β-cyclodextrin moieties. *Ind. Eng. Chem. Res.*, 46(5):1511–1518, 2007.

[61] F. Bloch, W. W. Hansen, and M. Packard. Nuclear induction. *Phys. Rev.*, 69(3-4): 127–127, 1946.

[62] E.M. Purcell, H.C. Torrey, and R.V. Pound. Resonance absorption by nuclear magnetic moments in a solid. *Phys. Rev.*, 69(1-2):37–38, 1946.

[63] J. Keeler. *Understanding NMR spectroscopy*. John Wiley & Sons, 2nd edition, 2011.

[64] H. Günther. *NMR spectroscopy: basic principles, concepts and applications in chemistry*. John Wiley & Sons, 2013.

[65] M.A. Brown, R.C. Semelka, and B.M. Dale. *MRI: basic principles and applications*. John Wiley & Sons, 2015.

[66] M. A. Bernstein, K. F. King, and X. J. Zhou. *Handbook of MRI pulse sequences*. Elsevier, 2004.

[67] R. Freeman. Shaped radiofrequency pulses in high resolution nmr. *Prog. Nucl. Magn. Reson. Spectrosc.*, 32(1):59–106, 1998.

[68] S. Berger. Nmr techniques employing selective radiofrequency pulses in combination with pulsed field gradients. *Prog. Nucl. Magn. Reson. Spectrosc.*, 30(3-4):137–156, 1997.

[69] P.T. Callaghan. *Translational dynamics and magnetic resonance: principles of pulsed gradient spin echo NMR*, chapter Introductory magnetic resonance, page 130. Oxford University Press, 2011.

[70] E.L. Hahn. Spin echoes. *Phys. Rev.*, 80(4):580, 1950.

[71] E.O. Stejskal and J.E. Tanner. Spin diffusion measurements: Spin echoes in the presence of a time-dependent field gradient. *J. Chem. Phys.*, 42(1):288–292, 1965.

[72] R.W. Brown, Y.C. N. Cheng, E.M. Haacke, M.R. Thompson, and R. Venkatesan. *Magnetic resonance imaging: physical principles and sequence design*. John Wiley & Sons, 2014.

[73] J.N. Dumez. Spatial encoding and spatial selection methods in high-resolution nmr spectroscopy. *Prog. Nucl. Magn. Reson. Spectrosc.*, 109:101–134, 2018.

[74] P. Mansfield and P.K. Grannell. NMR 'diffraction' in solids? *J. Phys. C: Solid State Phys.*, 6(22):L422–L426, 1973.

[75] B.T Doan, S. Meme, and J.C. Beloeil. General principles of mri. In *The Chemistry of Contrast Agents in Medical Magnetic Resonance Imaging*, pages 1–23. John Wiley & Sons, Ltd, 2013.

[76] M.A. Syed, S.V. Raman, and O.P. Simonetti, editors. *Basic Principles of Cardiovascular MRI: Physics and Imaging Techniques*. Springer International Publishing, 2015.

[77] T. R. Brown, B. M. Kincaid, and K. Ugurbil. Nmr chemical shift imaging in three dimensions. *Proc. Natl. Acad. Sci. U.S.A.*, 79(11):3523–3526, 1982.

[78] A. Salvati, I. Lynch, C. Malmborg, and D. Topgaard. Chemical shift imaging of molecular transport in colloidal systems: Visualization and quantification of diffusion processes. *J. Colloid Interface Sci.*, 308(2):542–550, 2007.

[79] J. Hedin, Å. Östlund, and M. Nydén. Uv induced cross-linking of starch modified with glycidyl methacrylate. *Carbohydr. Polym.*, 79(3):606–613, 2010.

[80] Å. Östlund, D. Bernin, L. Nordstierna, and M. Nydén. Chemical shift imaging nmr to track gel formation. *J. Colloid Interface Sci.*, 344(1):238–240, 2010.

[81] P. Knöös, D. Topgaard, M. Wahlgren, S. Ulvenlund, and L. Piculell. Using nmr chemical shift imaging to monitor swelling and molecular transport in drug-loaded tablets of hydrophobically modified poly(acrylic acid): Methodology and effects of polymer (in)solubility. *Langmuir*, 29(45):13898–13908, 2013.

[82] S. Bulut, I. Åslund, D. Topgaard, H. Wennerström, and U. Olsson. Lamellar phase separation in a centrifugal field. a method for measuring interbilayer forces. *Soft Matter*, 6(18):4520, 2010.

[83] D.I. Hoult. Solvent peak saturation with single phase and quadrature fourier transformation. *J. Magn. Reson.*, 21(2):337–347, 1976.

[84] G. Zheng and W.S. Price. Solvent signal suppression in nmr. *Prog. Nucl. Magn. Reson. Spectrosc.*, 56(3):267–288, 2010.

[85] P.A. Bottomley. Spatial localization in nmr spectroscopy in vivo. *Ann. N.Y. Acad. Sci.*, 508(1):333–348, 1987.

[86] J. Frahm, Merboldt. K.D., and W. Hänicke. Localized proton spectroscopy using stimulated echoes. *J. Magn. Reson.*, 72(3):502–508, 1987.

[87] Stephen F Keevil. Spatial localization in nuclear magnetic resonance spectroscopy. *Phys. Med. Biol.*, 51(16):R579, 2006.

[88] E.L. Cussler. *Diffusion: mass transfer in fluid systems*. Cambridge University Press, 2009.

[89] W.S. Price. Pulsed-field gradient nuclear magnetic resonance as a tool for studying translational diffusion: Part i. basic theory. *Concepts Magn. Reson.*, 9(5), 1997.

[90] H. Thérien-Aubin, X.X. Zhu, C.N. Moorefield, K. Kotta, and G.R. Newkome. Effect of ionic binding on the self-diffusion of anionic dendrimers and hydrophilic polymers in aqueous systems as studied by pulsed gradient nmr techniques. *Macromolecules*, 40 (10):3644–3649, 2007.

[91] R. Valiullin. *Diffusion NMR of Confined Systems: Fluid Transport in Porous Solids and Heterogeneous Materials*. Royal Society of Chemistry, 2016.

[92] J. Fisher. *Modern NMR Techniques for Synthetic Chemistry*. CRC Press, 2014.

[93] W.S. Price. Nmr gradient methods in the study of proteins. *Annu. Rep. Prog. Chem., Sect. C: Phys. Chem.*, 96:3–53, 2000.

[94] H. Hervet, L. Léger, and F. Rondelez. Self-diffusion in polymer solutions: A test for scaling and reptation. *Phys. Rev. Lett.*, 42:1681–1684, 1979.

[95] M. Zou, Y.L. Han, L. Qi, and Y. Chen. Fast and accurate measurement of diffusion coefficient by taylor's dispersion analysis. *Chin. Sci. Bull.*, 52(24):3325–3332, 2007.

[96] J. E. Anderson and J. H. Jou. Small-angle neutron scattering studies of diffusion in bulk polymers: experimental procedures. *Macromolecules*, 20(7):1544–1549, 1987.

[97] U. Zettl, S.T. Hoffmann, F. Koberling, G. Krausch, J. Enderlein, L. Harnau, and M. Ballauff. Self-diffusion and cooperative diffusion in semidilute polymer solutions as measured by fluorescence correlation spectroscopy. *Macromolecules*, 42(24):9537–9547, 2009.

[98] R. Liu, X. Gao, J. Adams, and W. Oppermann. A fluorescence correlation spectroscopy study on the self-diffusion of polystyrene chains in dilute and semidilute solution. *Macromolecules*, 38(21):8845–8849, 2005.

[99] M.D. Burke, J.O. Park, M. Srinivasarao, and S.A. Khan. Diffusion of macromolecules in polymer solutions and gels: a laser scanning confocal microscopy study. *Macromolecules*, 33(20):7500–7507, 2000.

[100] T. M. Bender and R. Pecora. Dynamic light scattering measurements of mutual diffusion coefficients of water-rich 2-butoxyethanol/water systems. *J. Phys. Chem.*, 92(6):1675–1677, 1988.

[101] S. Kwak, M.T.P. Viet, and M Lafleur. Self-and mutual-diffusion coefficients measurements by 31p nmr 1d profiling and pfg-se in dextran gels. *J. Magn. Reson.*, 162(1): 198–205, 2003.

[102] M.A. Gagnon and M. Lafleur. Self-diffusion and mutual diffusion of small molecules in high-set curdlan hydrogels studied by 31p nmr. *J. Phys. Chem. B*, 113(27):9084–9091, 2009.

[103] J. Crank. *The mathematics of diffusion*. Oxford university press, 1979.

[104] S. Matsukawa, D. Sagae, and A. Mogi. Molecular diffusion in polysaccharide gel systems as observed by nmr. In Masayuki Tokita and Katsuyoshi Nishinari, editors, *Gels: Structures, Properties, and Functions*, pages 171–176, 2009.

[105] S. Matsukawa and I. Ando. Study of self-diffusion of molecules in a polymer gel by pulsed-gradient spin-echo 1h nmr. 2. intermolecular hydrogen-bond interaction between the probe polymer and network polymer in n, n-dimethylacrylamide- acrylic acid copolymer gel systems. *Macromolecules*, 30(26):8310–8313, 1997.

[106] S. Matsukawa and I. Ando. Study of self-diffusion of molecules in polymer gel by pulsed-gradient spin-echo 1h nmr. 3. stearyl itaconamide/n,n-dimethylacrylamide copolymer gels. *Macromolecules*, 32(6):1865–1871, 1999.

[107] A.H. Muhr and J.M.V. Blanshard. Diffusion in gels. *Polymer*, 23(7):1012–1026, 1982.

[108] A.G. Ogston. The spaces in a uniform random suspension of fibres. *Trans. Faraday Soc.*, 54:1754–1757, 1958.

[109] D. Langevin and F. Rondelez. Sedimentation of large colloidal particles through semidilute polymer solutions. *Polymer*, 19(8):875 – 882, 1978.

[110] D. Zamir, R.C. Wayne, and R.M. Cotts. Anomalous nuclear magnetic resonance linewidth in lithium. *Phys. Rev. Lett.*, 12(12):327–330, 1964.

[111] R.M. Cotts, M.J.R. Hoch, T. Sun, and J.T. Markert. Pulsed field gradient stimulated echo methods for improved nmr diffusion measurements in heterogeneous systems. *J. Magn. Reson.*, 83(2):252 – 266, 1989.

[112] K. Zick. Diffusion nmr user manual (version 003), 2009.

[113] M. Poustchi-Amin, S.A. Mirowitz, J.J. Brown, R.C. McKinstry, and T. Li. Principles and applications of echo-planar imaging: A review for the general radiologist. *RadioGraphics*, 21(3):767–779, 2001.

[114] J. Granot. Selected volume excitation using stimulated echoes (VEST). applications to spatially localized spectroscopy and imaging. *J. Magn. Reson.*, 70(3):488–492, 1986.

[115] J. Frahm, H. Bruhn, M. L. Gyngell, K. D. Merboldt, W. Hänicke, and R. Sauter. Localized proton nmr spectroscopy in different regions of the human brainin vivo. relaxation

times and concentrations of cerebral metabolites. *Magn. Reson. Med.*, 11(1):47–63, 1989.

[116] H.V. Chavda and C.N. Patel. Effect of crosslinker concentration on characteristics of superporous hydrogel. *Int. J. Pharm. Investig.*, 1(1):17, 2011.

[117] M.H. Kabir, K. Ahmed, and H. Furukawa. The effect of cross-linker concentration on the physical properties of poly (dimethyl acrylamide-co-stearyl acrylate)-based shape memory hydrogels. *Microelectron. Eng.*, 150:43–46, 2016.

[118] I. Katime, E. D. de Apodaca, and E. Rodriguez. Effect of crosslinking concentration on mechanical and thermodynamic properties in acrylic acid–co–methyl methacrylate hydrogels. *J. Appl. Polym. Sci.*, 102(4):4016–4022, 2006.

[119] R. Wong, M. Ashton, and K. Dodou. Effect of crosslinking agent concentration on the properties of unmedicated hydrogels. *Pharmaceutics*, 7(3):305–319, 2015.

[120] B. Adrjan, M. Karbarz, W. Koźmiński, and Z. Stojek. Comparison of electrochemical- and nuclear magnetic resonance spectroscopy methods for determination of diffusion coefficients in gel environment. *Electrochim. Acta*, 144:228 – 234, 2014.

[121] A. Pourjavadi, S. Barzegar, and G.R. Mahdavinia. Mba-crosslinked na-alg/cmc as a smart full-polysaccharide superabsorbent hydrogels. *Carbohydr. Polym.*, 66(3):386–395, 2006.

[122] P.J. Flory. *Principles of polymer chemistry*. Cornell University Press, 1953.

[123] L. Jowkarderis and T.G.M. van de Ven. Mesh size analysis of cellulose nanofibril hydrogels using solute exclusion and pfg-nmr spectroscopy. *Soft Matter*, 11(47):9201–9210, 2015.

[124] J.C. Cuggino, C.B. Contreras, A. Jimenez-Kairuz, B.A. Maletto, and C.I. Alvarez Igarzabal. Novel poly(nipa-co-aac) functional hydrogels with potential application in drug controlled release. *Mol. Pharmaceutics*, 11(7):2239–2249, 2014.

[125] X.Z. Zhang, Y.Y. Yang, F.J. Wang, and T.S. Chung. Thermosensitive poly(n-isopropylacrylamide-co-acrylic acid) hydrogels with expanded network structures and

improved oscillating swelling-deswelling properties. *Langmuir*, 18(6):2013–2018, 2002.

[126] C.C. Ruiz. Thermodynamics of micellization of tetradecyltrimethylammonium bromide in ethylene glycol–water binary mixtures. *Colloid Polym. Sci.*, 277(7):701–707, 1999.

I

Journal of Applied Polymer Science

Determining the scaling of gel mesh size with changing crosslinker concentration using dynamic swelling, rheometry, and PGSE NMR spectroscopy

Malgorzata Anna Wisniewska,[1] John Georg Seland,[1] Wei Wang [1,2]
[1]Department of Chemistry, University of Bergen, Bergen, 5007, Norway
[2]Centre for Pharmacy, University of Bergen, Bergen, 5020, Norway
Correspondence to: W. Wang (E-mail: wei.wang@uib.no)

ABSTRACT: We studied the scaling behavior of the mesh size (ξ) of chemically crosslinked poly(*N*-isopropylacrylamide-*co*-acrylic acid) hydrogels with changing crosslinker concentration (C_{cl}) from 0.006 to 0.143 mol L^{-1}. Three experimental methods were employed, namely dynamic swelling, rheometry, and probe diffusion by pulsed gradient spin-echo NMR. The mesh sizes determined by probe diffusion are dependent on the probe size. The scaling model of $\xi \sim (C_{cl})^n$ ($n < 0$) could describe variation of the mesh size, obtained by any of the aforementioned techniques, with the crosslinker concentration. Thus, for hydrogels in equilibrium with water, the obtained values of the scaling exponent (n) are −0.73 ± 0.05 for dynamic swelling, −1.0 ± 0.3 for probe diffusion, and −0.27 ± 0.02 for rheological measurements. We demonstrated that the scaling of the mesh sizes for probe diffusion and dynamic swelling results was in good agreement with theoretical prediction. © 2018 Wiley Periodicals, Inc. J. Appl. Polym. Sci. **2018**, *135*, 46695.

KEYWORDS: rheology; swelling; theory and modeling

DOI: 10.1002/app.46695

INTRODUCTION

In an ideal drug delivery system, drug release is synchronized with the physiological status of a patient in response to changes in a biological environment.[1] Often, motions of drug molecules are restrained by drug carriers in order to reach the first-order release rate.[2] Among the controlled-release systems, hydrogels have drawn considerable attention in recent years.[3–6] In a hydrogel, the release rate is substantially reduced due to restricted diffusion of drug molecules in the tridimensional network. On a macroscopic scale, fractal resistance and tortuosity are much higher in a hydrogel than they are in pure solvents.[7–9]

To understand the restricted diffusion in such drug formulation, the crucial point in establishing a theory is to determine the single characteristic length defined as the average distance between two adjacent crosslinks, also known as the mesh size.[10] The diffusion coefficient (D) of drug molecules (i.e., solutes) can be related to the mesh size (ξ) by

$$\frac{D}{D_0} = \exp\left(-\frac{r_s}{\xi}\right), \quad (1)$$

which indicates that drug release from a hydrogel is determined by the ratio of the solute radius (r_s) and the mesh size (ξ).[11,12] Here, D_0 is the diffusion coefficient of the solute in the absence of restrictions.[13,14] With a certain drug, regardless of the interaction between the drug molecule and the hydrogel, the diffusion of the drug molecules depends only on the mesh size.[2,15,16] Thus, in order to design a formulation for a controlled-release purpose, establishing reliable methods for determining the mesh size, and understanding the differences between the values one gets from different techniques become crucial.[17,18] Poly(*N*-isopropylacrylamide-*co*-acrylic acid) [poly(NIPAM-*co*-AAc)] is a model hydrogel for controlled-release studies due to its thermo- and pH-responsive properties.[19–22] This polymer has been investigated in the forms of macroscopic hydrogels, films, micro- and nanoparticles.[19,20,23–25] The mesh size of hydrogels in the hydrated state can be determined by experimental techniques such as dynamic swelling, inverse size-exclusion chromatography, fluorescence recovery after photobleaching, probe diffusion by pulsed gradient spin-echo (PGSE) NMR, rheometry, and dynamic light scattering.[10,13,14,26–31] In the present study, we used poly(NIPAM-*co*-AAc) as the model hydrogel and focused on the characterization of the mesh size by means of dynamic swelling, rheometry, and PGSE NMR. The difference between the mesh sizes obtained by these methods have been established. Also, it was found that variation of the mesh size (obtained by any of the

Additional Supporting Information may be found in the online version of this article.

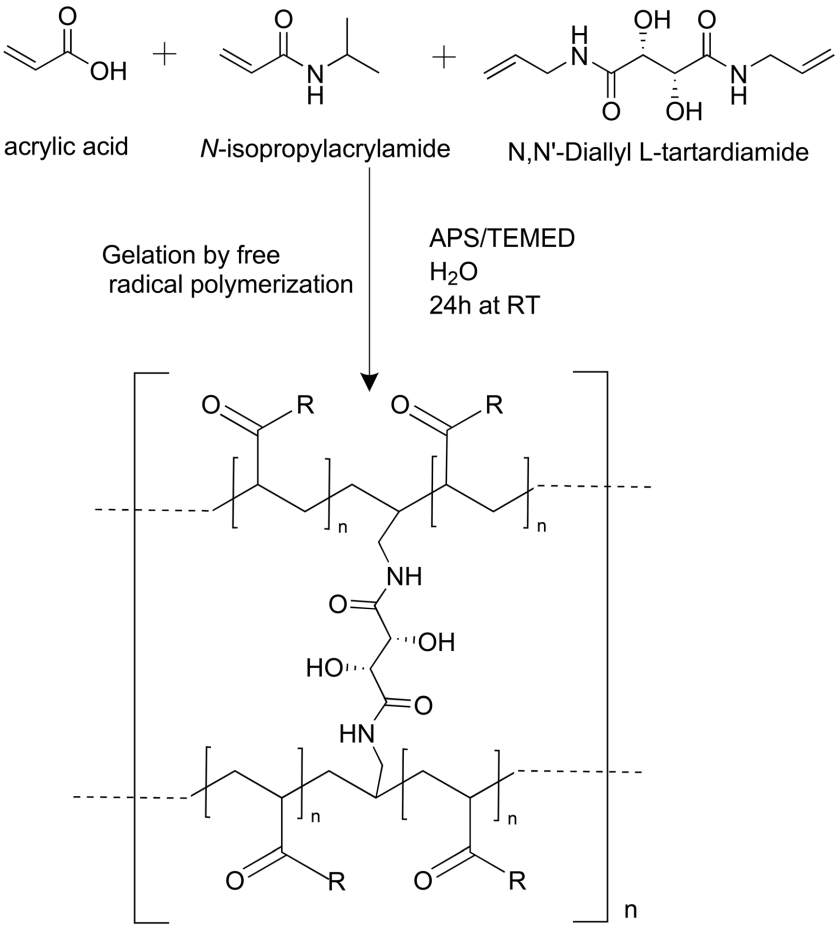

Figure 1. The synthetic route for poly(NIPAM-*co*-AAc) hydrogels. R represents the hydroxyl group in acrylic acid or —NH-CH-$(CH_3)_2$ groups in *N*-isopropylacrylamide.

aforementioned techniques) with the crosslinker concentration could be described by the scaling model of $\xi \sim (C_{cl})^n$. This is the first report dedicated to a thorough investigation and a detailed comparison of the scaling of the mesh size with the crosslinker concentration determined using the aforementioned three different methods.

EXPERIMENTAL

Materials

N-Isopropylacrylamide (NIPAM, >99%), acrylic acid (AAc, 99%, anhydrous, containing 200 ppm hydroquinone monomethyl ether), ammonium persulfate (APS, Bioxtra ≥98.0%), *N*,*N*,*N*′,*N*′-tetramethylethylenediamine (TEMED, ≥99.5%), and (+)-*N*,*N*′-diallyltartramide (DAT, ≥99%) were purchased from Sigma-Aldrich (Oslo, Norway) and used as received. Samples subjected to NMR measurements were prepared using deuterium oxide (99.9 atom % D, Sigma-Aldrich). For the rest of the experiments, Milli-Q water was used. Four types of dextran were purchased from Sigma-Aldrich with average molecular weights of 5, 12, 68 and 513 kDa.

Synthesis of Hydrogels

Hydrogels were prepared by free radical polymerization in aqueous solutions using NIPAM and AAc as monomers, DAT as crosslinker, and a redox couple APS/TEMED as initiator. A mixture of the monomers, DAT, and APS was dissolved in 5 mL of distilled water in a glass vial. The solution was put into an ultrasonic bath for 10 min, followed by 5 min nitrogen bubbling to deoxygenate the solution. After degassing, 12 μL of 6.63 *M* TEMED was added. The reaction was carried out at room temperature for 24 h. The scheme of the reaction route is shown in Figure 1. For preparing the hydrogel, the total concentration of the monomers (NIPAM and AAc) was set at approximately 0.7 mol L^{-1}, and the molar ratio of NIPAM to AAc was 0.95–0.05. One equivalent of TEMED

Table I. Ten Hydrogels Were Synthesized with Different Concentrations of DAT

Sample no.	NIPAM (mol L^{-1})	AAc (mol L^{-1})	DAT (mol L^{-1})	DAT (wt %)
1	0.669	0.033	0.006	0.13
2	0.669	0.033	0.009	0.18
3	0.668	0.032	0.012	0.25
4	0.668	0.032	0.019	0.40
5	0.668	0.032	0.024	0.50
6	0.669	0.033	0.036	0.75
7	0.669	0.033	0.048	1.00
8	0.668	0.035	0.072	1.50
9	0.668	0.032	0.098	2.00
10	0.668	0.033	0.143	3.00

with respect to APS was used. Based on the expected variation of mesh sizes with crosslinker content, the concentration of DAT was varied in a logarithmic manner between 0.006 and 0.143 mol L^{-1}. The conversion of the monomers in the hydrogel was monitored using ^{1}H NMR, and complete conversion (>95%) was achieved for all hydrogels with various amount of crosslinkers.

After the synthesis, the hydrogels were dialyzed for 1 week by changing dialysis medium daily in order to remove unreacted monomers. Afterward, the hydrogels were dried for 3 days at room temperature. The concentrations of the reactants for each sample are listed in Table I.

Determination of the Swelling Behavior of the Hydrogels

The dry hydrogels (approximately 100 mg) were incubated individually in beakers with an excess amount of water. At each time point, water was discarded, and samples were superficially dried with tissue paper, weighed and put into fresh water. The mass swelling ratio (Q_m) of the hydrogels is calculated based on

$$Q_m = \frac{W_s}{W_d}, \tag{2}$$

where W_s is the weight of the swollen hydrogel and W_d is the weight of the dry hydrogel.

Rheological Characterization

Rheological characterization of the hydrogels was carried out on a Kinexus rheometer (Malvern Instruments Ltd, Worcestershire, UK) using cone and plate geometry. All measurements were subjected to a closed environment by using a thermal hood to minimize water loss. Amplitude sweep studies (strain 0.01–10% at constant frequency of 2 Hz) were performed at 298 K in order to determine the linear viscoelastic region. Afterward, frequency sweep tests from 10 to 0.1 Hz at a constant strain ($\gamma_0 = 0.01$) were performed at 298 K to determine the storage modulus (G') and the loss modulus (G'') of hydrogels.

PGSE NMR Characterization

PGSE NMR was carried out on a Bruker Avance III 500 WB spectrometer (Rheinstetten, Germany) operating at 500 MHz for protons, equipped with a commercial NMR probe (diff30) capable of producing magnetic field gradient pulses up to 17 T/m in the z-direction. The measurements were performed at 298 (±1) K using a stimulated echo sequence with bipolar field gradient pulses (diffSteBp).[32,33] For the NMR measurements, the hydrogels were first dried in air. The dried samples were subsequently incubated in 5 mg mL^{-1} dextran solution prepared with D_2O until swelling equilibrium was reached. The samples were then carefully transferred into standard 5 mm NMR tubes. For the diffusion experiments, the signal intensity was recorded as a function of gradient strength (g) at 32 different values between 0.05 and 5.73 T/m. The maximum values of g (g_{max}) were chosen to obtain almost complete attenuation (>90%) of the dextran resonances. The gradient duration time (δ) and the diffusion time (Δ) were fixed at 2 and 50 ms, respectively. Peak area was used to compute diffusion coefficients by using the Stejskal–Tanner equation[34]:

$$\frac{I}{I_0} = e^{-\gamma^2 g^2 \delta^2 \left(\Delta - \frac{\delta}{3}\right) D}, \tag{3}$$

where I/I_0 is the signal attenuation, Δ is the effective diffusion time, D is the diffusion coefficient (m^2 s^{-1}), γ is the gyromagnetic ratio of the observed nucleus (26.7522×10^7 rad T^{-1} s^{-1}), g is the applied gradient amplitude (T m^{-1}), and δ is the effective gradient pulse width. Due to the size distribution of the dextran molecules, the signal attenuations will not be mono-exponential. For diffusion of dextran in a dilute solution, this may be taken into account by fitting the signal attenuations to a distribution of diffusion coefficients.[35] However, for diffusion of dextran in the hydrogels, additional effects from restricted diffusion and trapping of dextran molecules have to be accounted for, and in our opinion, a model based on a distribution of diffusion coefficients would then not give a correct description of the observed behavior. We therefore chose to obtain average diffusion coefficients by fitting the initial slope of the signal attenuation using eq. (3). Four dextrans with different molecular weights (5, 12, 68, and 513 kDa) were used as probes for the measurements.

Theory

Mesh Size Based on Swelling Experiment. In the swelling experiments, Flory's theory was used to determine the mesh size. The mesh size of a swollen hydrogel (ξ^{sw}) is dependent on the root-mean-square end-to-end distance of the polymer subchain between two crosslinking points in the unperturbed state ($\sqrt{\langle r_0^2 \rangle}$) in the following manner:

$$\xi^{sw} = \nu_{2s}^{-\frac{1}{3}} \sqrt{\langle r_0^2 \rangle}, \tag{4}$$

where ν_{2s} is the volume fraction of the polymer, which equals the reciprocal value of the volumetric swelling degree (Q_v^{-1}).

For calculating $\sqrt{\langle r_0^2 \rangle}$, the following expression is used:

$$\sqrt{\langle r_0^2 \rangle} = l \left(\frac{2M_c}{M_0}\right)^{\frac{1}{2}} C_N^{\frac{1}{2}}, \tag{5}$$

where l is the length of a C—C bond (l = 0.154 nm), M_c is the molar mass of the subchain between two crosslinking points, M_0 is the molar mass of the monomer (calculated from the weighted ratio of the two monomers), and C_N is the Flory's characteristic

ratio, which is a measure of the extension of the polymer chain in a disordered condition. Here, C_N is calculated to be 11.46 based on the weight ratio of the monomers in the hydrogel.

Assuming a statistical copolymerization in the synthesis, the molar mass of the subchain between two crosslinking points (M_c) is given by the average molar mass of monomers (M_0) and the degree of crosslinking (d_c) as[36]

$$M_c = \frac{1}{2} M_0 d_c^{-1}, \tag{6}$$

and

$$\mathrm{d}_c = \frac{n_{\mathrm{DAT}}}{n_{\mathrm{NIPAM}} + n_{\mathrm{AAc}} + n_{\mathrm{DAT}}}, \tag{7}$$

where n_{DAT}, n_{NIPAM}, and n_{AAc} are the number of moles of DAT, NIPAM, and AAc, respectively.

The value of the volumetric swelling ratio (Q_v) can be obtained by measuring the increase of the weight of the hydrogel during the swelling process in the following manner:

$$Q_v^{-1} = \frac{\frac{1}{\rho_{\mathrm{pol}}}}{\frac{Q_m}{\rho_{\mathrm{solv}}} + \frac{1}{\rho_{\mathrm{pol}}}}, \tag{8}$$

where Q_m is the mass swelling ratio, and ρ_{solv} and ρ_{pol} are the densities of the solvent and the hydrogel, respectively. For hydrogel swollen in water at 298 K, ρ_{solv} is 1.0 g mL^{-1}, and ρ_{pol} is 1.1 g mL^{-1}. Based on eqs. (4–8), the mesh size of the hydrogels can be obtained by determining the swelling ratio of the hydrogel at each stage. Thus, we have

$$\xi^{\mathrm{sw}} = l\left(\frac{n_{\mathrm{DAT}}}{n_{\mathrm{NIPAM}} + n_{\mathrm{AAc}} + n_{\mathrm{DAT}}}\right)^{-\frac{1}{2}} \left(\frac{Q_m \rho_{\mathrm{pol}}}{\rho_{\mathrm{solv}}} + 1\right)^{\frac{1}{3}}. \tag{9}$$

For a specific hydrogel, all the parameters of eq. (9) are known except Q_m, which can be measured.

Mesh Size Based on Rheological Measurements. The mesh size estimated from rheological measurements is based on the Flory's theory of rubber elasticity of Gaussian chains.[37] According to Flory's theory, the equilibrium shear elastic modulus corresponds to the frequency-independent elastic modulus G' (plateau modulus) in the following manner:

$$G' = A\frac{\rho}{M_c}RT, \tag{10a}$$

$$v_e = \frac{\rho}{M_c}, \tag{10b}$$

where A is the structure factor, ρ is the polymer density, M_c is the number average chain molecular weight, R is the universal gas constant, T is the temperature, and v_e is the number of effective network chains per volume unit of polymer. The structure factor A equals $1 - 2/f$ for a phantom network, where f is the functionality of the crosslinks.[38,39] G' is the plateau value of the storage modulus, which was used as the elastic modulus G, since $G'' \ll G'$.[37,40]

The number of effective network chains per volume unit of polymer v_e is related to the density of effective junctions (n_e) in the following manner[41,42]:

$$v_e = \left(\frac{f}{2}\right) n_e. \tag{11}$$

By using the expression obtained for the elastic modulus in eqs. (10a) and (10b), two different approaches have been adopted for calculation of n_e and ultimately mesh size. In the first approach, the volume element of the hydrogel is considered to be a cube. An estimation for the mesh size can be determined from the average spacing between the neighboring entanglements.[43] The calculation is based on the assumption that these intersections are evenly dispersed and positioned in the center of a cubic shaped volume element (for details see Ref. 43). Considering that all of the cubic elements contribute to the extension of the total volume of the gel, an expression for the length (L) of a side of the cubic element and the mesh size at the initial state ($\xi_{c,i}^{\mathrm{rheo}}$) could be obtained in the following manner:

$$\xi_{c,i}^{\mathrm{rheo}} = \frac{L}{2} = \left(\frac{RT}{G'N_A}\right)^{\frac{1}{3}}, \tag{12}$$

where N_A is the Avogadro's number.

The other approach to characterize the mesh size is to replace the true network with idealized spheres as suggested in the equivalent network theory.[44–46] Radius of such spheres corresponds to the average mesh size, which is comparable to the results determined by the other methods.[44] Based on the definition of crosslinking density, the spherical volume competing for each crosslink can be determined by the following equation:

$$\frac{4}{3}\pi\left(\xi_{s,i}^{\mathrm{rheo}}\right)^3 = \frac{RT}{G'N_A}. \tag{13}$$

Thus, using this approach, the expression for the mesh size at the initial state ($\xi_{s,i}^{\mathrm{rheo}}$) can be written as

$$\xi_{s,i}^{\mathrm{rheo}} = \left(\frac{3}{4\pi}\right)^{\frac{1}{3}} \left(\frac{RT}{G'N_A}\right)^{\frac{1}{3}} = \left(\frac{3}{4\pi}\right)^{\frac{1}{3}} \xi_{c,i}^{\mathrm{rheo}} \cong 0.62\, \xi_{c,i}^{\mathrm{rheo}}. \tag{14}$$

Mesh Size Based on PGSE NMR Measurements. The principle of computing the mesh size by PGSE NMR is different from the other two methods. In hydrogels, the diffusion of probe molecules primarily occurs within the water-filled regions in the space delineated by the polymer chain. Due to a comparably higher fractal resistance and tortuosity, the diffusion of the probe molecule is slower than it is in solution. The mesh size of a hydrogel can be indirectly obtained by comparing the diffusion coefficient of the probe in a gel phase to the diffusion coefficient in a dilute solution using diffusion models. The restricted diffusivity of probe molecules due to the polymer network can be expressed as the diffusion quotient ($\frac{D_g}{D_0}$) where D_g is the diffusion coefficient of the dextran probe trapped in a polymer network and D_0 is the diffusion coefficient of the dextran probe in the absence of a polymer network. According to the hydrodynamic scaling model, the mesh size can be estimated by eq. (1). The hydrodynamic radius of the dextran probe (r_s) can be obtained from the mean-inverse diffusion coefficient measured in a dilute solution by the Stokes–Einstein equation in the following manner[47]:

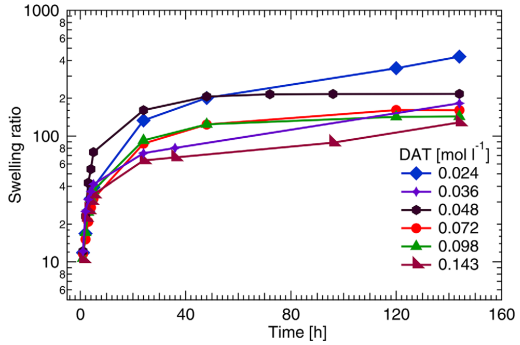

Figure 2. Swelling ratio as a function of time for the samples with different crosslinker concentration. [Color figure can be viewed at wileyonlinelibrary.com]

$$r_s = \frac{k_B T}{6\pi\eta D_0}, \tag{15}$$

where k_B is the Boltzmann's constant, T is the absolute temperature, and η is the viscosity of D_2O (η = 1.0939 mPa s) at 298 K.[48] Thus, using eqs. (1) and (15), one gets the following expression:

$$\xi^{NMR} = \frac{k_B T}{6\pi\eta D_0}\left(\ln\frac{D_0}{D_g}\right)^{-1}. \tag{16}$$

RESULTS

Mesh Sizes Obtained by Dynamic Swelling

The swelling of the hydrogels is driven by the affinity of the polymer and the solvent. When the interaction of polymer–solvent is balanced by the elastic retractive force, the gel swelling process reaches equilibrium after approximately 6 days for all of the hydrogels (Figure 2). The equilibrated volumes of the hydrogels with different crosslinker concentrations were used for obtaining the mesh size using eq. (9). The results are presented in Figure 3

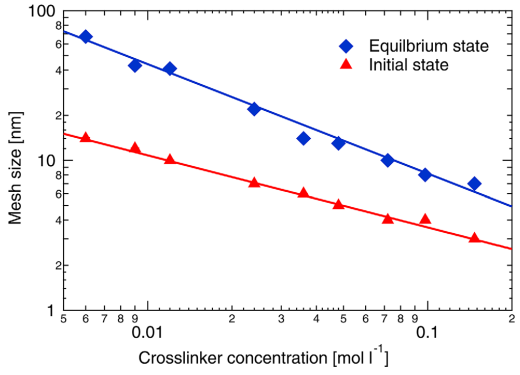

Figure 3. Mesh size of poly(NIPAM-*co*-AAc) determined as a function of crosslinker concentration at the equilibrium state (ξ_{eq}^{sw}) and the initial state (ξ_i^{sw}). The function of $\xi = k(C_{cl})^n$ is fitted to data, which yields the exponent (n) values of $n = -0.73 \pm 0.05$ (for the equilibrium state), and $n = -0.48 \pm 0.05$ (for the initial state). [Color figure can be viewed at wileyonlinelibrary.com]

Table II. The Mesh Sizes at Equilibrium and at the Initial State Retrieved by Means of Dynamic Swelling Is Presented

C_{cl} (mol L^{-1})	Q_{ms}	Q_{mc}	$\sqrt{\langle r_0^2\rangle}$ (nm)	ξ_{eq}^{sw} (nm)	ξ_i^{sw} (nm)
0.006	1502.7	12.8	5.7	67	14
0.009	931.7	12.7	4.7	47	12
0.012	931.7	12.5	4.0	40	10
0.024	428.7	12.0	2.8	22	7
0.036	182.0	12.0	2.4	14	6
0.048	216.5	12.4	2.1	13	5
0.072	163.9	11.9	1.7	10	4
0.098	143.0	11.7	1.5	8	4
0.143	128.3	12.1	1.3	7	3

C_{cl} is the crosslinker concentration in the hydrogels, Q_{ms} is the swelling ratio at equilibrium, Q_{mc} is the swelling ratio after crosslinking, $\sqrt{\langle r_0^2\rangle}$ is the root-mean-square end-to-end distance of the polymer subchain between two crosslinking points in the unperturbed state, ξ_{eq}^{sw} is the mesh size at the equilibrium, and ξ_i^{sw} is the mesh size just after crosslinking.

and Table II. Variation of the mesh size with the crosslinker concentration follows a clear trend, meaning that a higher crosslinker concentration leads to a lower swelling degree (Figure 2), and further results in a smaller mesh size (Figure 3). For example, upon an increase in the crosslinker (DAT) concentration from C_{cl} = 0.006 mol L^{-1} to C_{cl} = 0.098 mol L^{-1}, the obtained mesh size decreased from 65 to 8 nm. The hydrogel with the highest crosslinker concentration of C_{cl} = 0.143 mol L^{-1} had the lowest measured mesh size of 7 nm.

Mesh sizes were also determined for the samples at the initial state just after crosslinking. In this case, the swelling degree at the initial state (Q_{mc}) was used in eq. (9). The results are presented in the Table II and Figure 3. Comparing the mesh sizes at the initial state (ξ_i^{sw}) to the mesh sizes at the equilibrium state (ξ_{eq}^{sw}), one notices a decrease in difference of mesh size at the two states once the crosslinker concentration is increased. With the smallest crosslinking concentration (C_{cl} = 0.006 mol L^{-1}), the mesh size at the equilibrium state is approximately five times larger than the mesh size at the initial state ($\xi_{eq}^{sw} \cong 5\xi_i^{sw}$), whereas for the sample containing C_{cl} = 0.143 mol L^{-1} DAT, the former is only two times larger than the latter ($\xi_{eq}^{sw} \cong 2\xi_i^{sw}$).

Mesh Sizes Obtained by Rheological Measurements

The values of the storage modulus (G') during frequency sweep tests for the fully crosslinked hydrogels with varying crosslinker concentration is presented in Figure 4. The storage moduli of the hydrogels are independent of the frequency, which indicates that hydrogels are mechanically strong and elastic. Thus, the plateau value of the storage modulus (G') was used to compute the mesh size of the hydrogels. The hydrogels containing higher crosslinker concentration exhibited higher G' values. This means that more rigid structures were formed with increasing crosslinker concentration (see Supporting Information Figure S1). The measurement uncertainty is higher for the hydrogels with the specific values of such crosslinker concentrations in parenthesis.

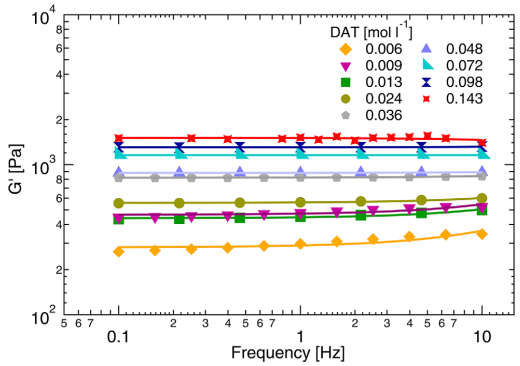

Figure 4. Characterization of the storage modulus as a function of frequency. [Color figure can be viewed at wileyonlinelibrary.com]

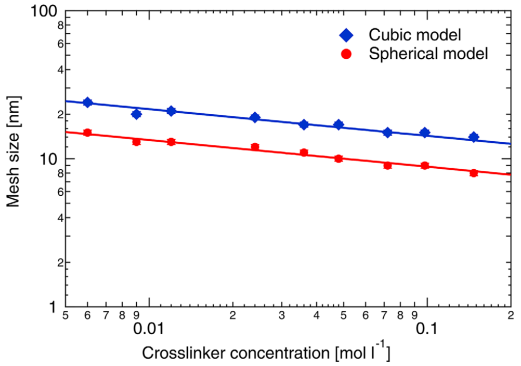

Figure 5. Mesh sizes obtained by the rheological measurements ($\xi_{c,i}^{rheo}$ and $\xi_{s,i}^{rheo}$ for cubic and spherical models, respectively) are presented as a function of crosslinker concentration. The function $\xi = k(C_{cl})^n$ is fitted to data, which yields the exponent (n) value of $n = -0.18 \pm 0.02$. [Color figure can be viewed at wileyonlinelibrary.com]

The theoretical functionality of the crosslinker (f) is 4 as each DAT molecule can react with four polymeric segments. Thus, for the hydrogels in the initial state, the combination of Eqs. (10a), (10b), and (11) leads to the following expression:

$$G' = n_e RT. \quad (17)$$

To calculate the density of the rheologically active junctions using eq. (17), we assumed that each crosslinker molecule forms only one crosslink. The results are presented in Table III and Supporting Information Figure S2. The values of n_e are within 2% of the theoretical crosslinker concentration for the sample with 0.006 M DAT and only 0.5% for the sample with 0.143 M DAT (see Supporting Information Table S1). This means that the efficiency of the crosslinker to form the junction decreases when more crosslinker was added.

As described in the Theory section, two models were used to obtain the mesh sizes for the hydrogels with different crosslinker concentrations. In Table III and Figure 5, the values of the mesh sizes determined by these two models ($\xi_{c,i}^{rheo}$ and $\xi_{s,i}^{rheo}$) are summarized. The active crosslinked intersections in the hydrogel network can be estimated by applying the classical theory of rubber elasticity [eqs. (10a) and (10b)], which indicates that increasing the number density of active intersections results in an increase of G'. Also, an increase in the number of active intersections results in a reduction in the molar mass of the subchain between two crosslinking points (M_c). Thus, the hydrogel networks with higher crosslinker concentration exhibit a smaller average mesh size.

In the rheology measurements, the hydrogels were synthesized in the compartment of rheometer suggesting that the mesh size obtained by the rheological measurements ($\xi_{c,i}^{rheo}$ and $\xi_{s,i}^{rheo}$) are comparable to the mesh size at the initial state in the dynamic swelling (ξ_i^{sw}). The mesh size assuming a spherical volume element ($\xi_{s,i}^{rheo}$) is approximately 38% lower than the mesh size assuming a cubic volume element ($\xi_{c,i}^{rheo}$).

Table III. Comparison Between the Mesh Size Determined from Rheological Measurements Assuming a Cubic-Shaped Volume Element [$\xi_{c,i}^{rheo}$; eq. (12)] and a Spherical Volume Element [$\xi_{s,i}^{rheo}$; eq. (13)]

C_{cl} (mol L^{-1})	G' (Pa)	n_e (mol m^{-3})	$\xi_{c,i}^{rheo}$ (nm)	$\xi_{s,i}^{rheo}$ (nm)
0.006	297	0.12	24	15
0.009	480	0.19	20	13
0.012	445	0.18	21	13
0.024	562	0.23	19	12
0.036	822	0.33	17	11
0.048	883	0.36	17	10
0.072	1160	0.47	15	9
0.098	1310	0.53	15	9
0.143	1660	0.67	14	8

n_e represents the density of effective junctions.

Mesh Size Obtained by PGSE NMR Spectroscopy

The ^{1}H NMR spectra for the dextrans are identical due to the same chemical structure of the monomer. Three peaks of the

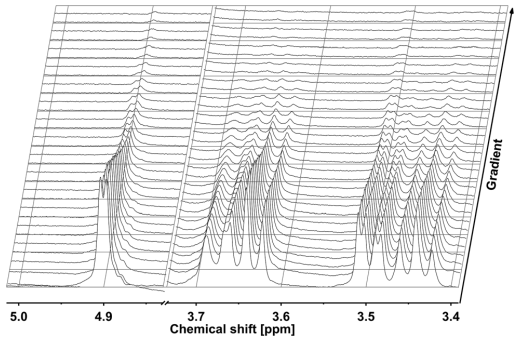

Figure 6. ^{1}H NMR signal decay for 5 kDa dextran in hydrogel.

Table IV. Diffusion Coefficients of Dextrans Used in the Aqueous Solutions D_0 Obtained by Fitting eq. (3) to NMR Data, and the Corresponding Hydrodynamic Radii r_s Obtained Using eq. (15)

M_w (kDa)	$D_0 \times 10^{11}$ (m^2 s^{-1})	r_s (nm)
5	12.33 ± 0.02	1.6 ± 0.1
12	8.2 ± 0.1	2.4 ± 0.1
68	4.5 ± 0.1	4.5 ± 0.1
513	1.45 ± 0.02	13.8 ± 0.3

dextran are not overlapped with the peaks of poly(NIPAM-*co*-AAc) hydrogels; therefore, they are used for the analysis. These peaks were assigned to the chemical shift of OH (4.91 ppm) and CH_2 (3.66 and 3.47 ppm) groups. PGSE NMR spectra of the dextran (5 kDa) are shown in Figure 6. The integrals of the CH_2 resonances were used for determining the diffusion coefficients of the probes in the hydrogels (D_g). For more detailed information, we refer to Supporting Information Figures S3–S7 and Supporting Information Table S2.

The sizes of the dextrans were determined by measuring the probe diffusion in pure D_2O. Table IV reports the diffusion coefficients of dextrans (D_0) together with their hydrodynamic radii (r_s).[49] The results are in good agreement with the data reported by Wallace *et al.*[13] and Jowkarderis and van de Ven.[14] The mesh sizes for each hydrogel can be calculated using eq. (1). The results are presented in Table V and Figure 7. The difference between D_0 and D_g increased with increases in the crosslinking concentration and the size of the dextrans. The results of the probe diffusion measurements indicate that the diffusion quotient ($\frac{D_g}{D_0}$) decreases exponentially with increasing dextran size (r_s), as described in eq. (1) (see Supporting Information Figure S8). For each hydrogel, the diffusion quotient ($\frac{D_g}{D_0}$) was fitted to eq. (1) varying the dextran size, which yields one value of the mesh size for each crosslinker concentration (see Supporting Information Figure S8).[50] For the two lowest DAT concentration measured, values of $\frac{D_g}{D_0}$ were similar for all of the dextran probes used. Thus, the values of ξ^{NMR} were estimated to be 104 and 103 nm, for the samples with crosslinker concentrations of 0.006 and 0.009 mol L^{-1}, respectively. For the four dextran probes used, for the crosslinker concentrations above 0.009 mol L^{-1}, the differences in values of $\frac{D_g}{D_0}$ were more pronounced. For the sample featuring C_{cl} = 0.036 mol L^{-1}, the value of $\frac{D_g}{D_0}$ was 0.88 for the 5 kDa dextran and 0.36 for the 513 kDa dextran, which corresponds to ξ^{NMR} values of 18 nm (for 5 kDa dextran) and 35 nm (for 513 kDa dextran). This indicates that the diffusivity of the 513 kDa dextran is significantly restricted by the hydrogel network, whereas the 5 kDa dextran is relatively free to move within the pores. The value of ξ^{NMR} decreased from 8.9 nm (for C_{cl} = 0.072 mol L^{-1}) to 7.0 nm (for C_{cl} = 0.143 mol L^{-1}). Entrapment of the dextran molecules in the gel network was observed in the signal echo decay for 68 and 513 kDa dextrans in the hydrogels with 0.072 and 0.143 mol L^{-1} DAT. Therefore, it was not possible to obtain meaningful diffusion coefficients for these situations. Thus, the mesh size (ξ^{NMR}) for these hydrogels is estimated based on the dextran 5 and 12 kDa probes, only.

Table V. For Poly(NIPAM-*co*-AAc) Hydrogels, Average Mesh Sizes Measured Using PGSE NMR (ξ^{NMR})

C_{cl} (mol L^{-1})	$\frac{D_{g,d1}}{D_{0,d1}}$	$\frac{D_{g,d2}}{D_{0,d2}}$	$\frac{D_{g,d3}}{D_{0,d3}}$	$\frac{D_{g,d4}}{D_{0,d4}}$	ξ^{NMR} (nm)
0.006	0.96	0.82	0.93	0.92	104 ± 80
0.009	0.90	0.94	0.91	0.91	103 ± 54
0.012	0.98	0.93	0.71	0.79	41 ± 14
0.024	0.96	0.90	0.71	0.45	27 ± 6
0.036	0.88	0.78	0.63	0.36	12 ± 2
0.048	0.84	0.78	0.67	0.46	9.6 ± 0.2
0.072	0.85	0.75	—	—	8.9 ± 0.7
0.143	0.79	0.71	—	—	7.0 ± 0.1

The crosslinker concentrations in the hydrogel is represented by C_{cl}, $\frac{D_{g,d1}}{D_{0,d1}}$, $\frac{D_{g,d2}}{D_{0,d2}}$, $\frac{D_{g,d3}}{D_{0,d3}}$, and $\frac{D_{g,d4}}{D_{0,d4}}$ represent the diffusion quotients for dextrans with molecular weight of 5, 12, 68, and 513 kDa, respectively; ξ^{NMR} is the value of the mesh size obtained by using different dextrans.

DISCUSSION

In Figures 3, 5, and 7, we present the scaling of the mesh size with crosslinker concentration determined using the three aforementioned methods. The results can be put into two categories in terms of the swelling state of the hydrogels. In the first one, the mesh sizes were obtained immediately after the crosslinking, namely the initial state. This includes the results obtained immediately after crosslinking using rheometry ($\xi^{rheo}_{c,i}$ and $\xi^{rheo}_{s,i}$) and dynamic swelling (ξ^{sw}_i). In the second category, we consider the mesh sizes when the hydrogels are in equilibrium with the solvent (i.e., water), including the mesh sizes obtained by dynamic swelling in equilibrium (ξ^{sw}_{eq}) and probe diffusion using PGSE NMR (ξ^{NMR}). In Figures 3, 5, and 7, variations of the mesh sizes with crosslink concentrations are presented in log–log plots. Regardless of the method used, the mesh sizes exhibit strong power-law decay with the increase of the crosslinker

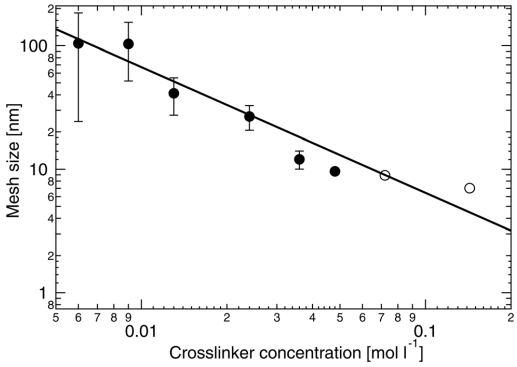

Figure 7. The mesh size obtained from PGSE NMR experiments (ξ^{NMR}) by using dextrans with different molecular weight as probes. The function $\xi = k(C_{cl})^n$ is fitted to data, which yields the exponent (n) value of $n = -1.0 \pm 0.3$. The last two data points marked by hollow circles were not used for the fitting of the power law function.

concentration. Therefore, the function $\xi = k(C_{cl})^n$ is used to determine the scaling exponent (n).

For the hydrogels in the initial state, the value of n varies with the methods. As can be seen in Figures 3 and 5, the values of the scaling exponent were $n = -0.48 \pm 0.05$ (dynamic swelling) and $n = -0.18 \pm 0.02$ (rheological measurements). In the following discussion, first we will convert the mesh sizes determined by rheometry (obtained for hydrogels in the initial state) to the mesh sizes for the case of analogous (in terms of crosslinker concentrations) hydrogels in equilibrium with water. This is followed by a comparison between the mesh sizes obtained by different methods. Second, we will make a comparison between our experimental results and the theoretical scaling of ξ on the degree of crosslinking d_c. At the end, the subjects of crosslinking nonuniformity and inefficiency of the network will be discussed.

Mesh Size When the Hydrogels Are in Equilibrium with Water

The swelling process corresponds to an isotropic expansion of the network. The dependence of the stored energy on strain is the same form for the hydrogel both in the initial state and in the equilibrium. If G'_i and G'_{eq} are the respective moduli in the initial state and at the equilibrium, then one has[40]

$$G'_{eq} = \nu_{2s}^{\frac{1}{3}} G'_i, \tag{18}$$

where ν_{2s} holds the same meaning as in eq. (4). Now using the values of (i) the storage modulus obtained from rheometry (which was at the initial state), (ii) ν_{2s} from the dynamic swelling experiments, and (iii) eqs. (12) and (14), the aim is to get the mesh sizes for analogous equilibrated swollen gels obtained during swelling measurements ($\xi^{rheo}_{c,eq}$ and $\xi^{rheo}_{s,eq}$). The results are presented in Figure 8 together with the mesh size obtained by the other methods.

Figure 8 shows that the mesh size is strongly model dependent. Based on the data, ξ^{NMR} and ξ^{sw}_{eq} show the highest values at the two lowest crosslinker concentrations. For these concentrations, the values of $\xi^{rheo}_{c,eq}$ and $\xi^{rheo}_{s,eq}$ are lower than ξ^{NMR} and ξ^{sw}_{eq}. The difference between the mesh sizes obtained using these methods decreased with the increment of the crosslinker concentration. However, for the most crosslinked hydrogels $\xi^{rheo}_{c,eq}$ and $\xi^{rheo}_{s,eq}$ are larger than ξ^{NMR} and ξ^{sw}_{eq}.

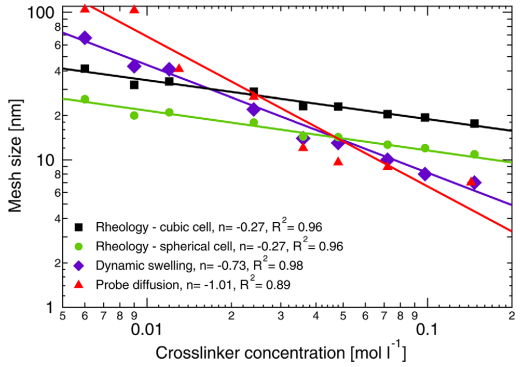

Figure 8. Comparison of the mesh sizes at equilibrium obtained using dynamic swelling, rheometry and probe diffusion PGSE NMR experiments. The function $\xi = k(C_{cl})^n$ was fitted to data. [Color figure can be viewed at wileyonlinelibrary.com]

Scaling of Mesh Size on Crosslinker Concentration

The relationship between mesh size and polymer concentration has been thoroughly discussed in the theoretical understanding of gelation process. In a physical gel, mesh size relates to polymer concentration by[37]

$$\xi \approx \sqrt{\langle r^2 \rangle} \left(\frac{c_p}{c^*}\right)^{-\nu/(3\nu-1)}, \tag{19}$$

where c_p is polymer concentration, c^* is the overlapping concentration, and ν is the Flory exponent ($\nu = 1/2$ in Θ solvents, 3/5 in good solvents). For a certain polymer solution, when the overlapping concentration is constant, the mesh size scales with polymer concentration with a power of −3/4 in a good solvent and −1 in a Θ solvent. However, in a chemically crosslinked gel, the relationship presented in eq. (19) becomes uncertain. According to the results presented in Figure 8, the mesh size decreases although the total polymer concentration is kept constant. This indicates that the relationship between mesh size and polymer concentration diverges from the classical theory. Since the scaling of mesh size with changing crosslinker concentration is not directly manifested in eq. (19), we use the Flory approximation to evaluate the fractal dimension of the crosslinker density.

In the percolation model,[51] the mesh size evolves with $|p - p_c|^{\beta}$ where p is the probability of bond formation, p_c is the critical value of p at the gel threshold, and β is the space dimension. The critical length (p_c) has been interpreted in two equivalent ways, using either sol or gel phase. In the dynamic swelling experiment, the former interpretation is applied, as shown in the following equation:

$$\xi = \nu_{2s}^{-\frac{1}{3}} \sqrt{\langle r_0^2 \rangle} \sim d_C^{-7}/10. \tag{20}$$

This equation is obtained from eq. (4) utilizing three equations, namely (i) the Flory–Rehner equation [eq. (21)], (ii) eq. (22) [from eq. (21) using the fact that M_c is inversely proportional to the crosslinker density $M_c \sim d_c^{-1}$], and (iii) eq. (23) [from eq. (5)]:

$$\nu_{2s} \sim Q_v^{-1} \sim M_c^{-3}/5, \tag{21}$$

$$\nu_{2s} \sim d_c^3/5, \tag{22}$$

$$\sqrt{\langle r_0^2 \rangle} \sim M_c^1/2 \sim d_c^{-1}/2. \tag{23}$$

Equation (20) shows that the mesh size of a hydrogel decreases with the crosslinker density by the power of −0.7. Equation (7) shows that if the total concentration of the monomers is constant, d_c is proportional to the crosslinker concentration (C_{cl}), which gives the following expression:

$$\xi \sim (C_{cl})^{-0.7}. \tag{24}$$

Thus, eq. (24) provides the general form of the scaling relationship between ξ and C_{cl}.

The experimental results show a fairly consistent agreement with theory, where scaling exponents of −0.73 and −1.0 were obtained for, respectively, dynamic swelling and probe diffusion experiments. Clearly, the scaling exponent obtained using dynamic swelling is very close to the theoretical value given in eq. (24), while the absolute value obtained in the probe diffusion experiments is too high. As seen in Figure 8, the deviation between these two methods is more pronounced for the two largest mesh sizes, where the probe diffusion experiments result in significantly higher values. Probe diffusion experiments are very sensitive to the size of the diffusing molecules,[13] and it is possible that the size of the dextran molecules used in our study are too small to properly detect the largest mesh sizes in samples with smallest degree of crosslinking, which may lead to an overestimation of the mesh size. Furthermore, an even larger difference in the scaling exponent is found for the rheological measurements, where for both of the approaches the scaling exponents (n) was −0.27. As shown in Figure 8, $\xi_{c,eq}^{rheo}$ and $\xi_{s,eq}^{rheo}$ are smaller than ξ_{eq}^{sw} at low crosslinker concentrations, but due to a lower scaling exponent, they crossover ξ_{eq}^{sw} at higher crosslinker concentrations. Some previous studies of hydrogel systems have shown similar mesh sizes obtained using rheology and swelling experiments,[52,53] while others have shown significant differences, which was explained by a possible failure of the rubber elasticity theory.[54] Further investigations are necessary in order to explain the differences in mesh sizes obtained using rheology and dynamic swelling in hydrogel systems.

Crosslinking Efficiency

In this study, the hydrogels were prepared by free radical copolymerization of monomers. The resulting network contains local highly crosslinked domains, which affect the physical properties of hydrogels, such as their swelling, elastics, and permeability properties.[55] In the rheometry section, we reported low crosslinking efficiency (see Supporting Information Table S1). This low crosslinking efficiency indicates that during the gelation process some crosslinker molecules participated in the formation of elastically inactive forms such as loops, trapped entanglements and dangling chains.[39,42,56,57] Moreover, the distribution of the crosslinker may be nonuniform, and therefore the spatial distribution of the pores may differ for the samples with the same chemical content.[58] Crosslinking nonuniformity and inefficiency increase with crosslinker concentration.[59] In all of the samples, there is most likely a group of large pores in the hydrogel network, which is accessible to all dextran probes. Within these pores, the diffusivity of the probe molecules is not significantly restricted. However, there are also regions with a denser network with smaller pores, where the diffusion of the probe is strictly limited. The analysis of diffusion PGSE NMR for the 513 kDa dextran in the most crosslinked gels supports this hypothesis. For the hydrogel with the crosslinker concentration of C_{cl} = 0.143 mol L^{-1}, the ratio of the dextran size (for 513 kDa molecule) and the mesh size was r_s/ξ^{NMR} = 1.97, which suggests entrapment of the probe molecule within the polymer network. However, the measured value of $\frac{D_{\xi,d4}}{D_{0,d4}}$ (0.46) for the high crosslinker concentration was higher the values for the less crosslinked sample (see Table V), which implies that the mobility of the dextran actually increased. This result indicates that pores with sizes much larger than the value of ξ^{NMR} exist, where the dextran molecule can almost freely diffuse. Consequently, the diffusion in these large pores has a great influence on the measured diffusion coefficient. For the same average mesh size, the extent of this restriction in diffusion increases with increasing molecular size of the probe.[60] Since the crosslinking nonuniformity and inefficiency of the network increase with crosslinker concentration, probe molecules with different sizes experience different network restrictions. This is in agreement with our PGSE NMR results, where for the two least crosslinked hydrogels, the mesh sizes calculated for all of the probes are very similar (see Supporting Information Table S2).

CONCLUSIONS

In summary, in order to investigate the mesh size of poly(NIPAM-*co*-AAc) hydrogels with different crosslinker concentrations at initial state (just after crosslinking) and equilibrium state (with water) three different methods were employed, namely dynamic swelling (ξ_i^{sw} and ξ_{eq}^{sw}), rheometry ($\xi_{c,i}^{rheo}$, $\xi_{s,i}^{rheo}$, $\xi_{c,eq}^{rheo}$, and $\xi_{s,eq}^{rheo}$) and probe diffusion PGSE NMR (ξ^{NMR}). The results show that the mesh size decreases with increasing crosslinker concentration in the hydrogels. More specifically, while at low crosslinking concentrations $\xi_{c,eq}^{rheo}$ and $\xi_{s,eq}^{rheo}$ were found to be smaller than ξ_{eq}^{sw} and ξ^{NMR}, at high concentrations they were found to be larger than ξ_{eq}^{sw} and ξ^{NMR}. The mesh sizes obtained by the probe diffusion (ξ^{NMR}) were generally larger than the mesh sizes measured by dynamic swelling (ξ_i^{sw} and ξ_{eq}^{sw}), in particular for the samples with low degrees of crosslinking and thus the largest mesh sizes. A possible explanation could be that the dextran molecules used in our study are too small to properly detect the largest mesh sizes. We also analyzed the effect of probe molecular size (r_s) on the measured mesh size. The probe diffusion gave also indication about a certain degree of crosslinking nonuniformity and inefficiency of the network. Although the mesh sizes exhibited a model-dependent nature, it was found that they exhibited a strong scaling behavior with respect to crosslinker concentrations. The results were fitted using the function $\xi = k(C_{cl})^n$, which gave exponent values of −0.73 ± 0.05 for the dynamic swelling experiments (close to the theoretical prediction), −1.0 ± 0.3 for the probe diffusion, and −0.27 ± 0.02 for the rheology measurements.

REFERENCES

1. Caló, E.; Khutoryanskiy, V. V. *Eur. Polym. J.* **2015**, *65*, 252.
2. Lin, C. C.; Metters, A. T. *Adv. Drug Deliv. Rev.* **2006**, *58*, 1379.
3. Ahmed, E. M. *J. Adv. Res.* **2015**, *6*, 105.
4. Liu, J. *Soft Matter* **2011**, *7*, 6757.
5. Satarkar, N. S.; Biswal, D.; Hilt, J. Z. *Soft Matter* **2010**, *6*, 2364.
6. Wang, W.; Sande, S. A. *Langmuir* **2013**, *29*, 6697.
7. Korsmeyer, R. W.; Gurny, R.; Doelker, E.; Buri, P.; Peppas, N. A. *Int. J. Pharm.* **1983**, *15*, 25.
8. Siepmann, J.; Peppas, N. A. *Adv. Drug Deliv. Rev.* **2001**, *48*, 139.

9. Siepmann, J.; Siepmann, F. *J. Control. Release* **2012**, *161*, 351.
10. Canal, T.; Peppas, N. A. *J. Biomed. Mater. Res.* **1989**, *23*, 1183.
11. Ogston, A. G. *Trans. Faraday Soc.* **1958**, *54*, 1754.
12. Langevin, D.; Rondelez, F. *Polymer* **1978**, *19*, 875.
13. Wallace, M.; Adams, D. J.; Iggo, J. A. *Soft Matter* **2013**, *9*, 5483.
14. Jowkarderis, L.; van de Ven, T. G. M. *Soft Matter* **2015**, *11*, 9201.
15. Stringer, J. L.; Peppas, N. A. *J. Control. Release* **1996**, *42*, 195.
16. Bell, C. L.; Peppas, N. A. *Biomaterials* **1996**, *17*, 1203.
17. Peppas, N.; Huang, Y.; Torres-Lugo, M.; Ward, J.; Zhang, J. *Annu. Rev. Biomed. Eng.* **2000**, *2*, 9.
18. Kim, S. W.; Bae, Y. H.; Okano, T. *Pharm. Res.* **1992**, *9*, 283.
19. Zhang, J.; Chu, L. Y.; Li, Y. K.; Lee, Y. M. *Polymer* **2007**, *48*, 1718.
20. Hu, J.; Zheng, S.; Xu, X. *J. Polym. Res.* **2012**, *19*, 9988.
21. Cuggino, J. C.; Contreras, C. B.; Jimenez-Kairuz, A.; Maletto, B. A.; Igarzabal, C. I. A. *Mol. Pharm.* **2014**, *11*, 2239.
22. Zhang, X. Z.; Yang, Y. Y.; Wang, F. J.; Chung, T. S. *Langmuir* **2002**, *18*, 2013.
23. Burmistrova, A.; Richter, M.; Uzum, C.; Klitzing, R. v. *Colloid Polym. Sci.* **2011**, *289*, 613.
24. Si, T.; Wang, Y.; Wei, W.; Lv, P.; Ma, G.; Su, Z. *React. Funct. Polym.* **2011**, *71*, 728.
25. Elashnikov, R.; Radocha, M.; Rimpelova, S.; Svorcik, V.; Lyutakov, O. *RSC Adv.* **2015**, *5*, 86825.
26. Zhou, Y.; Li, J.; Zhang, Y.; Dong, D.; Zhang, E.; Ji, F.; Qin, Z.; Yang, J.; Yao, F. *J. Phys. Chem. B* **2017**, *121*, 800.
27. Barretta, P.; Bordi, F.; Rinaldi, C.; Paradossi, G. *J. Phys. Chem. B* **2000**, *104*, 11019.
28. Wang, W.; Sande, S. A. *Polym. J.* **2015**, *47*, 302.
29. Wang, W.; Sande, S. A. *Eur. Polym. J.* **2014**, *58*, 52.
30. Xie, H.; Asad Ayoubi, M.; Lu, W.; Wang, J.; Huang, J.; Wang, W. *Sci. Rep.* **2017**, *7*, 8459.
31. Xie, H.; Wang, J.; Wang, W. *ChemistrySelect* **2017**, *2*, 9330.
32. Cotts, R. M.; Hoch, M. J. R.; Sun, T.; Markert, J. T. *J. Magn. Reson.* **1989**, *83*, 252.
33. Wu, D. H.; Chen, A. D.; Johnson, C. S. *J. Magn. Reson. A* **1995**, *115*, 260.
34. Stejskal, E. O.; Tanner, J. E. *J. Chem. Phys.* **1965**, *42*, 288.
35. Guo, X.; Laryea, E.; Wilhelm, M.; Luy, B.; Nirschl, H.; Guthausen, G. *Macromol. Chem. Phys.* **2017**, *218*, 1600440.
36. Tung, L. H.; Elias, H. G. Fractionation of Synthetic Polymers; M. Dekker: New York, **1977**.
37. Flory, P. J. Principles of Polymer Chemistry; Cornell University Press: Ithaca, NY, **1953**.
38. Nie, J.; Du, B.; Oppermann, W. *Macromolecules* **2005**, *38*, 5729.
39. Nie, J.; Du, B.; Oppermann, W. *Macromolecules* **2004**, *37*, 6558.
40. Treloar, L. R. G. Physics of Rubber Elasticity; OUP: Oxford, UK, **1975**.
41. Kulicke, W. M.; Nottelmann, H. ACS Publications, **1989**; p 15.
42. Calvet, D.; Wong, J. Y.; Giasson, S. *Macromolecules* **2004**, *37*, 7762.
43. Haggerty, L.; Sugarman, J.; Prudhomme, R. *Polymer* **1988**, *29*, 1058.
44. Pescosolido, L.; Feruglio, L.; Farra, R.; Fiorentino, S.; Colombo, I.; Coviello, T.; Matricardi, P.; Hennink, W. E.; Vermonden, T.; Grassi, M. *Soft Matter* **2012**, *8*, 7708.
45. Hild, G. *Prog. Polym. Sci.* **1998**, *23*, 1019.
46. Schurz, J. *Prog. Polym. Sci.* **1991**, *16*, 1.
47. Edward, J. T. *J. Chem. Educ.* **1970**, *47*, 261.
48. Kestin, J.; Imaishi, N.; Nott, S. H.; Nieuwoudt, J. C.; Sengers, J. V. *Phys. A* **1985**, *134*, 38.
49. Braeckmans, K.; Peeters, L.; Sanders, N. N.; De Smedt, S. C.; Demeester, J. *Biophys. J.* **2003**, *85*, 2240.
50. Sandrin, D.; Wagner, D.; Sitta, C. E.; Thoma, R.; Felekyan, S.; Hermes, H. E.; Janiak, C.; de Sousa Amadeu, N.; Kuhnemuth, R.; Lowen, H.; Egelhaaf, S. U.; Seidel, C. A. M. *Phys. Chem. Chem. Phys.* **2016**, *18*, 12860.
51. de Gennes, P.-G. Scaling Concepts in Polymer Physics; Cornell University Press: Ithaca, NY, **1979**.
52. Kirchhof, S.; Abrami, M.; Messmann, V.; Hammer, N.; Goepferich, A. M.; Grassi, M.; Brandl, F. P. *Mol. Pharm.* **2015**, *12*, 3358.
53. Adrus, N.; Ulbricht, M. *React. Funct. Polym.* **2013**, *73*, 141.
54. Lei, J.; Mayer, C.; Freger, V.; Ulbricht, M. *Macromol. Mater. Eng.* **2013**, *298*, 967.
55. Di Lorenzo, F.; Seiffert, S. *Polym. Chem.* **2015**, *6*, 5515.
56. Kizilay, M. Y.; Okay, O. *Polymer* **2003**, *44*, 5239.
57. Lindemann, B.; Schröder, U. P.; Oppermann, W. *Macromolecules* **1997**, *30*, 4073.
58. Ikkai, F.; Shibayama, M. *J. Polym. Sci. Part B: Polym. Phys.* **2005**, *43*, 617.
59. Travas-Sejdic, J.; Easteal, A. *J. Polymer* **2000**, *41*, 2535.
60. Yamane, Y.; Ando, I.; Buchholz, F. L.; Reinhardt, A. R.; Schlick, S. *Macromolecules* **2004**, *37*, 9841.

Supporting Information for

Determining the scaling of gel mesh size with changing crosslinker concentration using dynamic swelling, rheometry, and PGSE NMR spectroscopy

Malgorzata Anna Wisniewska[a], John Georg Seland[a] and Wei Wang*†[a,b]

[a]Department of Chemistry, University of Bergen, Bergen 5020, Norway [b]Centre for Pharmacy, University of Bergen, Bergen 5020, Norway

1 Rheometry

The values of the frequency-independent elastic modulus G' were calculated according to Equations 10a and 10b.

*E-mail: wei.wang@uib.no
†Tel: +47 55 58 33 55

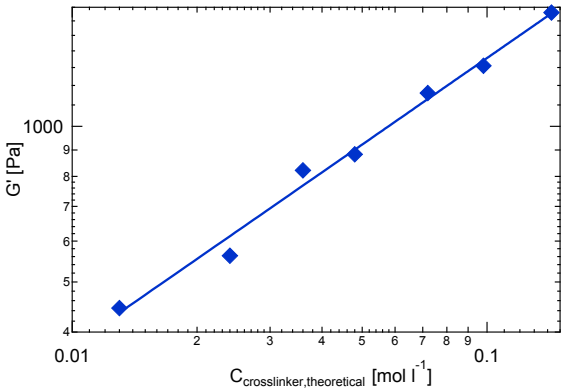

Figure S1: Plateau values of G'as a function of crosslinker concentration. Data fitted with a function of $G' = k(C_{cl})^n$, which yields the exponent (n) value of n = 0.55.

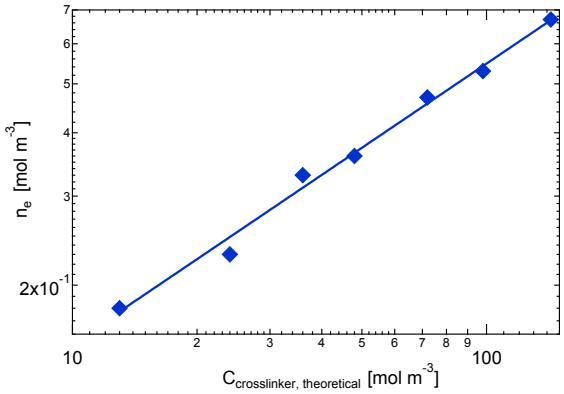

Figure S2: The values of the network junction density (n_e) as a function of the theoretical crosslinker concentration. Data fitted with a function of $n_e = k(C_{crosslinker,theoretical})^n$, which yields the exponent (n) value of n = 0.55.

Table S1: The theoretical crosslinking concentration C_{cl}, the density of effective junctions n_e and measured percentage of efficiency of the crosslinker

C_{cl} [mol m^{-3}]	n_e [mol m^{-3}]	% efficiency
6	0.12	2.00
9	0.19	2.15
12	0.18	1.38
24	0.23	0.95
36	0.33	0.92
48	0.36	0.74
72	0.47	0.65
98	0.53	0.54
143	0.67	0.47

2 PGSE NMR Measurements

All PGSE NMR experiments were recorded on Bruker Avance III 500 WB using diffSteBp pulse sequence. The intensity data were processed and fitted to Equation S1 using Bruker Topspin software package (version 3.5) and Igor Pro 6.37 software.

$$\frac{I}{I_0} = e^{-\gamma^2 g^2 \delta^2 (\Delta - \frac{\delta}{3}) D} \tag{S1}$$

Hydrodynamic radius of each dextran probe was estimated using Equation S2.

$$r_s = \frac{k_B T}{6\pi\eta D_0} \tag{S2}$$

Figure S3 shows the echo amplitude as a function of gradient strength for all dextran probes in aqueous solutions with fit to Equation S1.

For the free solutions, $\ln(\frac{I}{I_0})$ is linearly dependent on the parameter $\gamma^2 g^2 \delta^2 (\Delta - \frac{\delta}{3})$ with the negative slope being the self-diffusion coefficient. The resulting Stejskal-Tanner

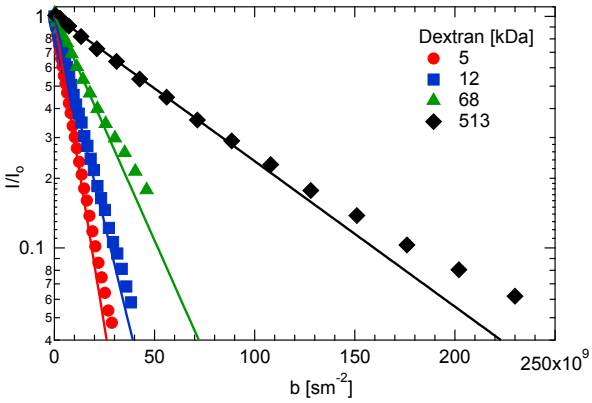

Figure S3: Normalized echo attenuations for the diffusion of the -CH_2 group of the dextrans, where $b = \gamma^2 g^2 \delta^2 (\Delta - \frac{\delta}{3})$. Lines represent the fitting of the data to Equation S1.

plots of the echo intensities of the signals from dextran 5 kDa, 12 kDa, 68 kDa and 513 kDa probes are shown in Figure S4, Figure S5, Figure S6 and Figure S7. In the free solutions, the intensities of the NMR signals follow a fast decay. Significant differences can be observed for the NMR signals of dextran 1 and dextran 2 in the presence of the polymer network. Here, two slopes corresponding to a fast and a slow intensity decay can be observed. The slow decay indicates severe restriction of the probe diffusion. The slope of the slow decay becomes flatter with the increasing crosslinker concentration. The corresponding diffusion coefficients, obtained by fitting the data using Equation S1, are listed in Table S2. The diffusion coefficients for the hydrogel samples stated in Table S2 were calculated based on the fast decays of the signal intensities.

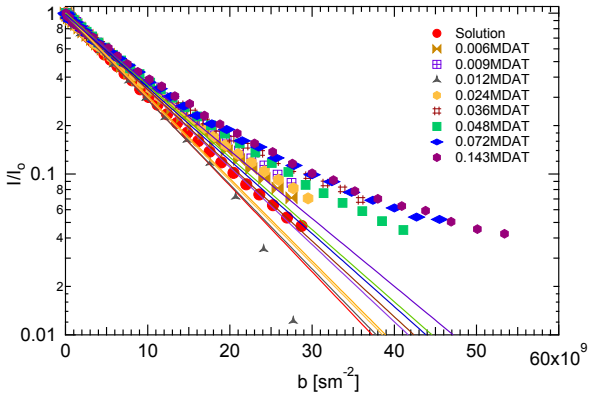

Figure S4: Normalized echo attenuations for the diffusion of the -CH_2 group of dextran 5 kDa, where $b = \gamma^2 g^2 \delta^2 (\Delta - \frac{\delta}{3})$. The solid lines represent the fitting of the data to Equation S1.

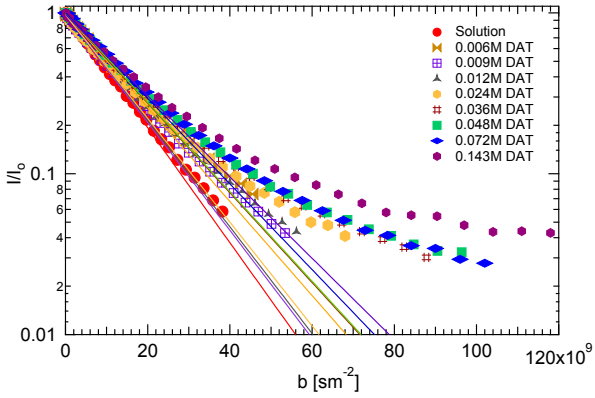

Figure S5: Normalized echo attenuations for the diffusion of the -CH_2 group of dextran 12 kDa, where $b = \gamma^2 g^2 \delta^2 (\Delta - \frac{\delta}{3})$. The solid lines represent the fitting of the data to Equation S1.

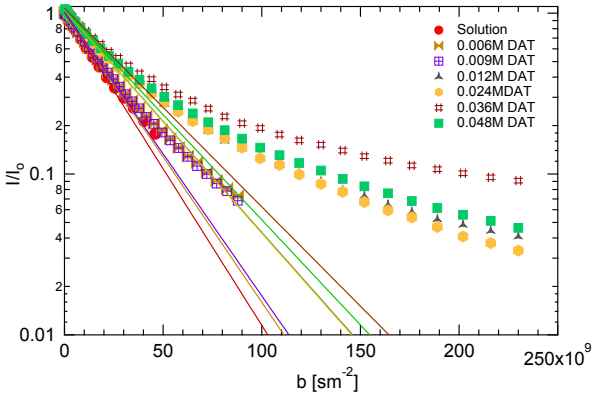

Figure S6: Normalized echo attenuations for the diffusion of the -CH_2 group of dextran 68 kDa, where $b = \gamma^2 g^2 \delta^2 (\Delta - \frac{\delta}{3})$. The solid lines represent the fitting of the data to Equation S1.

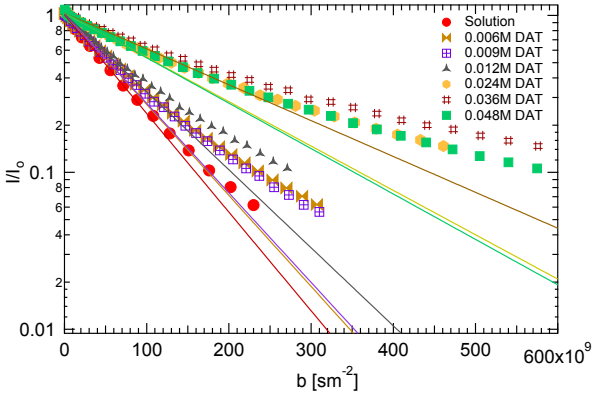

Figure S7: Normalized echo attenuations for the diffusion of the -CH_2 group of dextran 513 kDa, where $b = \gamma^2 g^2 \delta^2 (\Delta - \frac{\delta}{3})$. The solid lines represent the fitting of the data to Equation S1.

Table S2: Diffusion coefficients of dextran 5 kDa, 12 kDa, 68 kDa and 513 kDa in poly(NIPAM-*co*-AAc) hydrogels as measured by PGSE NMR. C_{cl} [mol l^{-1}] represents the crosslinker concentrations in the hydrogel; $D_{g,d1}$, $D_{g,d2}$, $D_{g,d3}$ and $D_{g,d4}$ [m^2 s^{-1}] represent the diffusion coefficients for dextran 5 kDa, 12 kDa, 68 kDa and 513 kDa, respectively

C_{cl}	$D_{g,d1} \times 10^{11}$	$D_{g,d2} \times 10^{11}$	$D_{g,d3} \times 10^{11}$	$D_{g,d4} \times 10^{11}$
Free solution	12.33±0.02	8.2±0.1	4.5±0.1	1.45±0.02
0.006	11.81±0.03	6.7±0.2	4.16±0.08	1.33±0.03
0.009	11.06±0.02	7.7±0.3	4.1±0.2	1.31±0.02
0.012	12.09±0.04	7.6±0.3	3.18±0.07	1.14±0.03
0.024	11.90±0.03	7.4±0.3	3.19±0.08	0.65±0.02
0.036	10.85±0.04	6.4±0.1	2.8±0.1	0.53±0.02
0.048	10.33±0.01	6.40±0.07	3.01±0.07	0.67±0.04
0.072	10.46±0.03	6.1±0.1	3.41±0.04	0.85±0.05
0.143	9.7±0.4	5.6±0.2	3.65±0.04	0.94±0.03

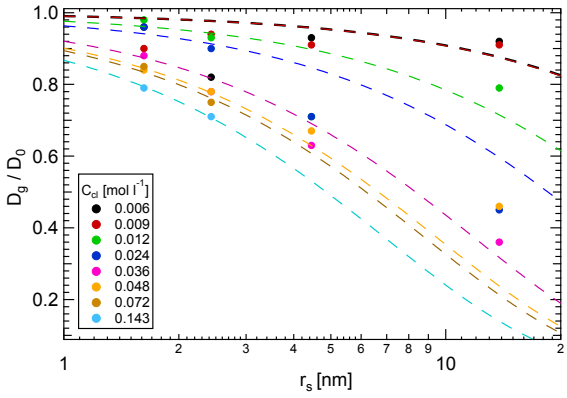

Figure S8: Diffusion quotients (D_g/D_0) of dextrans 5 kDa, 12 kDa, 68 kDa and 513 kDa in poly(NIPAM-*co*-AAc) hydrogels with various crosslinker concentrations. The dashed lines represent the fit to the model function in Equation 1.

II

Journal of Colloid and Interface Science 533 (2019) 671–677

Contents lists available at ScienceDirect

Journal of Colloid and Interface Science

journal homepage: www.elsevier.com/locate/jcis

Regular Article

Investigating structure-dependent diffusion in hydrogels using spatially resolved NMR spectroscopy

Malgorzata Anna Wisniewska *, John Georg Seland

Department of Chemistry, University of Bergen, Bergen 5007, Norway

GRAPHICAL ABSTRACT

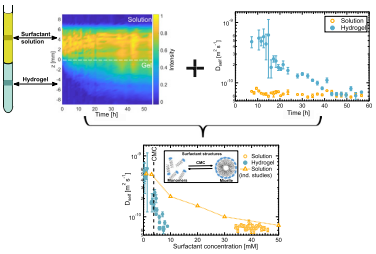

ARTICLE INFO

Article history:
Received 11 July 2018
Revised 28 August 2018
Accepted 29 August 2018
Available online 30 August 2018

Keywords:
Drug delivery
Diffusion
Slice selection NMR
1D chemical shift imaging

ABSTRACT

Hypothesis: Incorporation of the drug-loaded surfactant micelles into polymer hydrogels is a common method used to achieve controlled drug delivery. The characterization of the diffusion processes in drug delivery systems is critical in order to tune the drug loading and release.

Experiments: We present a simple and efficient NMR protocol to investigate the transport of the surfactant molecules in hydrogels on micro- and macroscale under non-equilibrium conditions. Our experimental protocol is based on a combination of ^{1}H 1D NMR chemical shift imaging and slice-selective diffusion experiments, which enables determination of the mutual and self-diffusion coefficients of the surfactant in the non-equilibrium hydrogel-based system within the same short time frame.

Findings: Our results show that the self-diffusion coefficient of the positively charged surfactant in the hydrogel (D_s^{gel}) decreases with the increasing surfactant concentration until it reaches a plateau value of $6.6 \pm 0.5 \times 10^{-11}$ m^2 s^{-1}. The surfactant self-diffusion in the solution (D_s^{sln}) remains constant over the experiment with an average value of $6.7 \pm 0.3 \times 10^{-11}$ m^2 s^{-1}. The surfactant mutual diffusion coefficient obtained from 1D chemical shift imaging in this hydrogel system (D_m) is $7.7 \pm 0.5 \times 10^{-11}$ m^2 s^{-1}. Correlation of the localized D_s to the 1D chemical shift images gives insight into the structure-dependent diffusional behavior of surfactant molecules in the hydrogel. This NMR protocol will be of great value in studies of concentration dependent structures on the interfaces between two immiscible liquids.

1. Introduction

In drug delivery, one of the common strategies to achieve a controlled release of a hydrophobic drug is to enclose a substance of interest in surfactant micelles, which can be embedded in a

* Corresponding author.
E-mail address: malgorzata.wisniewska@uib.no (M.A. Wisniewska).

https://doi.org/10.1016/j.jcis.2018.08.112
0021-9797/

hydrogel [1,2]. Poly(*N*-isopropylacrylamide) [poly(NIPAM)] is a model hydrogel for controlled release studies due to its thermo-responsive properties [3]. This polymer has been investigated in the forms of macroscopic hydrogels, films, micro- and nanoparticles [4–8]. As drug delivery systems, hydrogels have been limited to carry hydrophilic drugs, where the loading and releasing of the drug is rather inefficient. The formation of surfactant micelles allows either for the incorporation of drug molecules in the hydrophobic microdomain of the micelle core or condensation on the surface [9]. Micelles and vesicles of cationic surfactants have received much interest as carriers for chemotherapeutic agents bearing carboxylate groups due to possible drug complexation by anion binding [10,11]. The detailed knowledge of transport and release of surfactant molecules is essential to optimize the design of a drug delivery matrix. In this context, the measurement of diffusion coefficients represents one of the main approaches to better understand molecular mobility of the surfactant molecules. Diffusion measurements can be used to quantify and to predict the release rates of entrapped drugs from given matrices, and to provide structural information about the hydrogel network [12]. In hydrogels, there are two distinct types of transport mechanisms characterized on different length and time scales: self-diffusion and mutual diffusion. The first type occurs in the absence of a concentration gradient and is caused by Brownian motions [13]. Self-diffusion coefficients (D_s) can be measured on a millisecond time scale, using pulsed-field gradient NMR [14], fluorescence correlation spectroscopy [15] or fluorescence recovery after photobleaching [16]. On the other hand, mutual diffusion occurs in the presence of a concentration gradient and can be described by Fick's laws [17,18]. Mutual diffusion coefficients (D_m) are measured on time scales ranging from minutes to hours or days, using UV/VIS absorption spectroscopy [19], quasielastic light scattering spectroscopy [20], holographic interferometry [21], NMR imaging [22] or fluorescence correlation spectroscopy [23]. Moreover, mutual diffusion associated with the release or uptake involves the crossing of the solution/hydrogel interface, a phenomenon not experienced by the analyte during the self-diffusion measurements [24]. Here, we present a combination of 1D Chemical Shift Imaging (1D CSI) and Slice-Selective Diffusion (SSD) experiments for studying both mutual and self-diffusion in one experimental protocol. The 1D CSI method with submillimeter spatial resolution in one dimension can be used to obtain time-resolved information about the spatial distribution of surfactant molecules in a hydrogel system [25]. Kwak et al. demonstrated the potential of the ^{31}P 1D profiling for investigation of the macroscale mutual diffusion by recording the concentration profiles of the phosphate ions in dextran gels [26]. The important advantage of using the 1D CSI method is that the concentration profiles of all different chemical species in the sample can be obtained simultaneously in a single experiment. This method has previously been used to characterize the diffusion processes of several different pharmaceutical molecules in colloidal gels [27]. The dissolution behaviors and molecular transport in polymer tablets have also been studied by applying 1D CSI [28,29]. The SSD method can be used to determine self-diffusion coefficients in specific positions of the model system. Moreover, the combination of the two pulse sequences in one experimental protocol allows measurements of both diffusion coefficients on the same sample, under the same experimental conditions [24,26].

The main purpose of this work is to design a single NMR experimental protocol, which covers the diffusion processes in the model drug delivery system on microscopic and macroscopic scales. We demonstrate the usefulness of a method which combines 1D CSI and SSD NMR to study surfactant diffusion in poly (NIPAM) hydrogels under non-equilibrium conditions.

2. The method

^{1}H 1D CSI NMR [25,27] and SSD [30] experiments were combined in one experimental protocol to investigate the mutual and self-diffusion processes of the surfactant molecules in hydrogels under non-equilibrium conditions. In the experimental setup (Fig. 1), the surfactant diffusion occurs from the solution to the gel. The initial concentration of the surfactant in the gel (C_{gel}) is zero. As the access to the bottom phase and the edges of the hydrogel is limited by the walls of the NMR tube, only the upper face of the hydrogel was exposed to the surfactant solution over the hydrogel. Thus, the surfactant diffusion was restricted to one dimension only, which simplifies both the setup of the experiments and the evaluation of the results.

2.1. Chemical shift imaging

From the 1D CSI experiment, the concentrations of various molecules can be determined as functions of position and time.

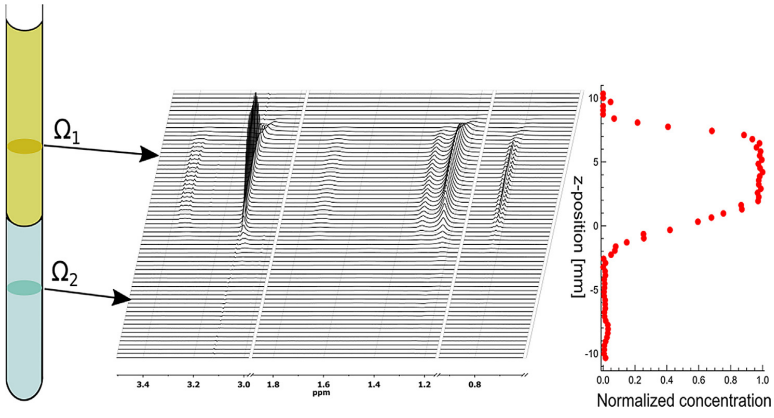

Fig. 1. Illustration of the experimental setup. The interface between surfactant solution and gel was aligned with the center of the radiofrequency (rf) coil (z = 0). Ω_1 and Ω_2 represent the position of the slices at which the self-diffusion spectra were obtained. Ω_1 corresponds to the slice in the solution whereas Ω_2 corresponds to the slice in the gel. The position- resolved chemical shift image recorded at the beginning of the experiment (t = 0 h) is presented in the middle. The corresponding concentration profile of a C_{14}TAB signal is shown to the right.

Using Fick's second law of diffusion for the case of the one-dimensional free diffusion into a semi-infinite slab, surfactant mutual diffusion coefficient, D_m, can be determined [17,22]:

$$\frac{\partial C}{\partial t} = D_m\left(\frac{\partial^2 C}{\partial z^2}\right), \quad (1)$$

where C is the concentration, t is the time, and z is the position. When no initial surfactant concentration is present in the gel, Fick's second law of diffusion can be rewritten [18]:

$$\frac{C_{gel}}{C_0} = erfc\frac{z}{2\sqrt{D_m t}}. \quad (2)$$

Concentration profiles were phase-corrected and normalized to the initial concentration of the surfactant in the solution, C_0. By fitting the experimentally obtained concentration profiles using Eq. (2), D_m can be estimated. An example of the obtained concentration profiles is shown in Fig. 1, where the peak intensity is plotted against sample heights (z-position). The Field of View (FOV) along the z-axis was calculated using:

$$FOV = \frac{2\pi N_{slices}}{2\gamma G_{max}\delta}, \quad (3)$$

where N_{slices} is the amount of slices recorded along z-axis, γ is the gyromagnetic ratio ($\gamma_{^1H} = 2.675 \times 10^8$ rad s^{-1} T^{-1}), G_{max} is the maximum strength of the magnetic field gradient, and δ is the length of the gradient pulse. The spatial resolution in the z-direction was calculated by dividing the FOV by N_{slices}.

2.2. Slice- selective diffusion NMR

Slice-selective diffusion experiments [31] were accomplished by applying a sine-shaped 180° radiofrequency (RF) pulse with variable frequency offsets (Ω) in the presence of a magnetic field gradient. By simultaneously applying a magnetic field gradient (G_z), all spins experience a frequency offset that depends on the vertical position (z) from the center of the gradient coil:

$$\Omega = \gamma G_z z. \quad (4)$$

Hence, a soft pulse with a bandwidth ($\Delta\Omega$) that is employed at this offset can selectively excite a horizontal slice of the sample centered at z with a thickness that is obtained by:

$$\Delta z = \frac{\Delta\Omega}{\gamma G_z}. \quad (5)$$

3. Materials and methods

3.1. Materials

N-isopropylacrylamide (NIPAM, >99%), ammonium persulfate (APS, BioXtra, 98%), N,N,N,N-tetramethylethylenediamine (TEMED, ⩾99%), (+)-N,N-diallyltartramide (DAT, ⩾99%), tetradecyltrimethylammonium bromide (C_{14}TAB) were purchased from Sigma-Aldrich, and used as received. Samples were prepared using deuterium oxide (99.9 atom% D, Sigma-Aldrich).

3.2. Methods

3.2.1. Hydrogel preparation

Hydrogel was prepared by free radical polymerization in aqueous solutions using NIPAM as monomer, DAT as crosslinker, and a redox couple APS/TEMED as initiator. A mixture of NIPAM, DAT and APS, was dissolved in 5 ml of distilled water in a glass vial. The solution was put into an ultrasonic bath for 10 min, followed by 5 min nitrogen bubbling to deoxygenate the solution. After that, 12 µl of 6.63 M TEMED was added. The reaction was carried out at room temperature for 24 h. In hydrogel preparation, the total concentration of the monomer was fixed at 0.7 mol L^{-1}. One equivalent of TEMED with respect to APS was used. Crosslinker concentration was fixed to 0.024 mol L^{-1}. After the synthesis, the hydrogel was dialyzed extensively for one week by changing dialysis medium daily in order to remove unreacted monomers. The hydrogel was then dried for 3 days at room temperature. The dried sample was subsequently incubated in excess amount of D_2O until swelling equilibrium was reached. The average mesh size, determined from the swelling experiment, was determined to be 11 nm (ESI).

3.2.2. Surfactant/hydrogel sample

Based on the article by Kwak et al. [26], where the differences between D_m values obtained from the release and penetration experiments with large and small reservoirs were studied, we decided to use the simplified penetration experiment and confine the reservoir to the same volume as the hydrogel. The experimental setup was designed to meet the conditions of the diffusion model derived for two semi-infinite media (Fig. 1). Hydrogel of known mass was placed in the bottom of the 5 mm o.d. NMR tube. The 50 mM surfactant (C_{14}TAB) solution was added as shown in Fig. 1 and the NMR tube was placed in the spectrometer defining the starting point of the experiment (t_0). The hydrogel and the solution lengths were both 22 mm. The sample was positioned so that the interface between surfactant solution and hydrogel was at the center of the gradient and RF coils (z = 0 mm). The sample temperature was maintained at 298 K.

3.2.3. NMR experiments

All the NMR experiments were performed on a Bruker Avance III 500 WB MHz NMR spectrometer equipped with a Bruker DIFF-30 gradient probe capable of delivering gradients of strength 17 T/m in the z-direction.

Spatially resolved ^{1}H NMR spectra were acquired with a 1D CSI pulse sequence [25,27], shown in Fig. 2a, with the following

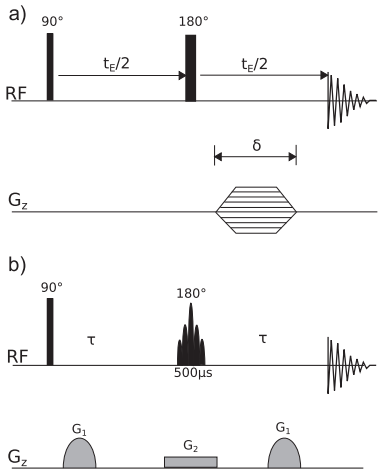

Fig. 2. NMR pulse sequences for the 1D CSI (a) and the SSD (b) experiments. In (a) the 90° and 180° RF pulses produce a spin echo at time t_E. A magnetic field gradient pulse of length δ and strength G encodes the signal with respect to position. Signal acquisition starts at the echo maximum. The spin system returns to equilibrium during a delay t_R between each repetition of the pulse sequence (not shown in the figure). In (b) the 180° pulse is sine shaped and has duration of 500 µs. The two G_1 gradients are for diffusion weighting, whereas G_2 gradient is used for spatial encoding.

parameters: t_E = 0.9 ms, t_R = 4 s, δ = 0.13 ms. G_z was incremented from −0.28 to 0.28 T/m in 64 steps. With these particular parameters the field of view is 20.65 mm, and the spatial resolution in the z-direction is 323 μm. With four transients per gradient increment, a z-resolved chemical shift image was recorded in less than 20 min.

SSD experiments were performed using the pulse sequence shown in Fig. 2b. A sine-shaped 180° pulse (Sinc3.1000) with duration of 500 μs was used for slice selection, and the strength of the gradient, $G_2$was 0.2 T/m. For localized diffusion of the C_{14}TAB species in the solution, four scans were collected for each experiment with Ω_1 = 50 kHz, whereas eight scans were recorded for the diffusion of the species localized in the hydrogel with Ω_2 = −50 kHz. Ω_1 and Ω_2 correspond to the single slices (1 mm thick) located at 5.87 mm and −5.87 mm from the center of the RF coil, respectively.

Due to the shape of the RF coil, the signal decreases in intensity in the edges of the chemical shift images (Fig. 1, 8 mm > z > 7 mm). At the positions 10 mm > z > 8 mm and −10 mm < z < −8 mm the intensity of the signal is 0 because the measured volume is outside of the RF coil.

4. Results and discussion

4.1. Concentration profiles

In Fig. 3 the NMR spectrum obtained from z = 0 mm position of the chemical shift image recorded at the end of the experiment is presented. The peaks for the hydrogel (P1-P4) and C_{14}TAB (S1-S5) are labeled in the spectrum.

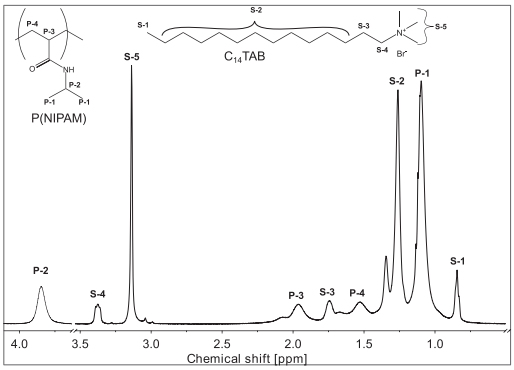

Fig. 3. ^{1}H spectrum of the hydrogel in equilibrium with C_{14}TAB, at z = 0 mm at the end of the experimental time.

Fig. 4 shows examples of chemical shift images recorded at the beginning (t = 0 h) and at the end (t = 55 h) of the experiment. For t = 0 h, the surfactant peaks are present in the solution (8 mm > z > 0 mm) but absent in the hydrogel (−8 mm < z < 0 mm). In the chemical shift image recorded after 55 h, the surfactant peaks are also present in the hydrogel, indicating diffusion of C_{14}TAB from the solution to the polymer network.

Fig. 5 shows the integrals of the polymer and surfactant peaks at the beginning and at the end of the diffusion experiment. For the C_{14}TAB signal at t = 0 h the decrease in signal intensity can be observed at 1 mm > z > −2 mm. This is most likely due to the uneven interface and the fact that the first chemical shift image was recorded after approximately 20 min from the injecting the surfactant solution on top of the hydrogel, and therefore a possible diffusion of the surfactant to the hydrogel in the interface area. As described earlier, the decrease in signal intensities is observed in the edges of the RF coil (8 mm > z > 7 mm and −8 mm < z < −7 mm). Chemical shift images were recorded for 55 h. At the end of the experiment, change in the position of the interface was observed.

4.1.1. Hydrogel

Fig. 6a shows the evolution of the signals from the hydrogel network during penetration of the C_{14}TAB solution. Over the whole experimental time, the polymer peak increased in intensity from 0 mm to 4.8 mm, indicating swelling of the polymer network upon interaction with C_{14}TAB molecules. During the experiment, the initial border of the hydrogel has been moved from 2 mm to 4 mm in the +z direction. This swelling influenced the average mesh size which increased from 11 nm (at t = 0 h) to 12 nm (at t = 55 h).

4.1.2. Surfactant

Over the course of the experiment (Fig. 6b), the C_{14}TAB signal in solution decreases (z values from 0 to 8 mm), with a corresponding increase in the gel (z values from 0 to −8 mm). This indicates diffusion from solution to the polymer network as the system moves to equilibrium. The time evolution of the signal intensity from C_{14}TAB to the left of the interface is used for the calculations of D_m. The signal integrals have been converted into molar concentration using a known initial C_{14}TAB concentration (50 mM) as an internal reference. Fitting the experimental data between 0 h and 55 h to Eq. (2) resulted in $D_m = 7.7 \pm 0.5 \times 10^{-11}$ m^2 s^{-1} (Fig. S1, ESI). Due to the changes in the interface between the hydrogel and the surfactant solution, the quality of the fitting by the model in Eq. (2) is reduced in the end of the experiment. We intend to examine this matter in future research.

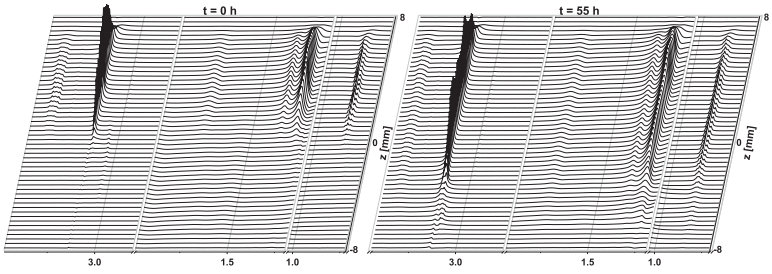

Fig. 4. ^{1}H Chemical shift images recorded at t = 0 h and t = 55 h after the addition of the 50 mM C_{14}TAB on top of the hydrogel. Slices located at the position of −8 mm < z < 0 mm correspond to the hydrogel phase, whereas spectra located at 8 mm > z > 0 mm correspond to the solution phase.

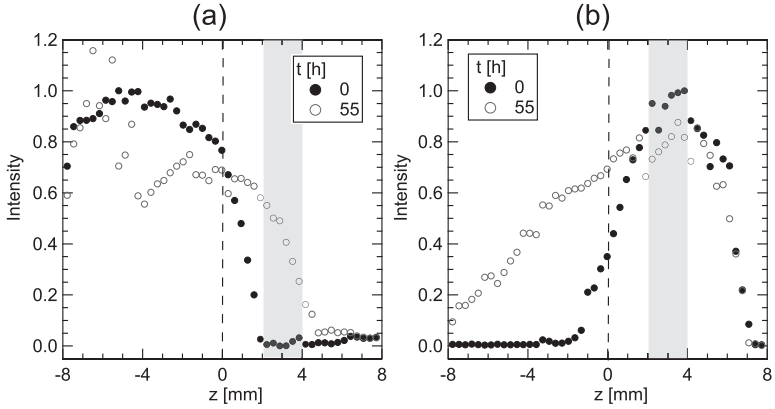

Fig. 5. The measured peak integrals of the polymer (a) and C_{14}TAB (b) signals obtained via integration, plotted as function of the vertical position in the NMR tube. The zero position (z = 0 mm, dashed line) represents the center of the RF coil. The change in the initial border of the hydrogel is highlighted in gray. The estimated error in the signal intensity was ±5%.

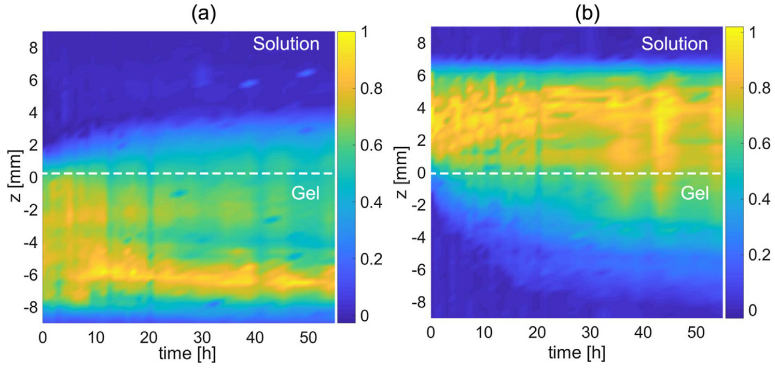

Fig. 6. Experimental results for the hydrogel-surfactant system. (a) Polymer and (b) C_{14}TAB peak areas obtained via integration, plotted as functions of the vertical position in the NMR tube. The dashed line indicated the position of the initial interface. The color scale shows the intensity.

4.2. Self-diffusion studies

The frequency offsets of the slice-selective pulses, Ω_1 and Ω_2, were chosen such that the self-diffusion was measured respectively in the solution and in the hydrogel. Fig. 7 presents the evolution of the C_{14}TAB self-diffusion coefficients in the solution (Ω_1) and hydrogel (Ω_2). As expected, the self-diffusion of C_{14}TAB in the solution (D_s^{sln}) remains constant at an average level of $6.7 \pm 0.3 \times 10^{-11}$ m^2 s^{-1}, indicating that the C_{14}TAB concentration in the solution is still above CMC. The C_{14}TAB self-diffusion in the hydrogel (D_s^{gel}) decreased during the experiment, with the initial fast decrease during the first 25 h. The D_s^{gel} reaches a plateau after 45 h with a value of around $6.6 \pm 0.5 \times 10^{-11}$ m^2 s^{-1}. The C_{14}TAB concentration in the two slices was retrieved from the 1D CSI experiments. The concentration profiles were normalized with respect to the initial concentration of C_{14}TAB, using the maximum intensity of the profile. Thus, relating the localized values of D_s to the concentration data gives valuable insight into the structure-dependent transport properties.

In the hydrogel, the initial D_s^{gel} is more than 5 times higher than D_s^{gel} measured in the same position at the end of the experiment. As it is visualized in Fig. 8, the C_{14}TAB diffuses first into the hydrogel in the form of monomers, and subsequently, after reaching the critical micelle concentration (CMC = 3.81 mM) in the gel phase, self-assembles into the micelles [32]. Fig. 8 shows that at the end of the experiment, the C_{14}TAB concentration in the Ω_2 position is 4–5 times lower than from the position located at Ω_1. The diffusion in the hydrogel thus decreases due to the increasing C_{14}TAB concentration. Self-diffusion coefficients of the self-assembled micelles in poly (NIPAM) hydrogel are about $1.8 \pm 0.2 \times 10^{-10}$ m^2 s^{-1} to $6.1 \pm 0.8 \times 10^{-11}$ m^2 s^{-1}. Considering surfactant monomers and micelles as spherical bodies, the hydrodynamic radius of C_{14}TAB micelles (R_h) was calculated from the D_s using the Stokes-Einstein equation [33]:

$$D = \frac{k_B T}{6\pi\eta R_h}, \tag{6}$$

where k_B is a Boltzmann's constant, T is the absolute temperature and η is the viscosity of D_2O (η = 0.0010939 Pa s) at 298 K [34]. The estimated hydrodynamic radius of C_{14}TAB in the monomeric form is 0.4 ± 0.1 nm. Thus, the surfactant monomers are around 28 times smaller than the hydrogel's initial average mesh size, which implies that they can diffuse freely in the hydrogel network.

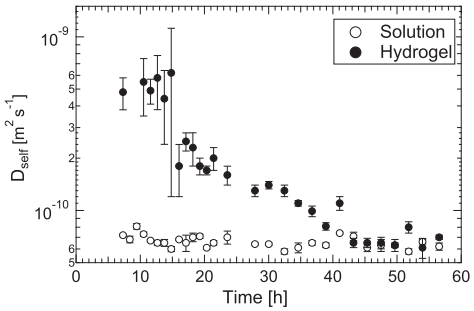

Fig. 7. The diffusion coefficient of the surfactant in solution (slice located at +5.87 mm from the center of the RF coil) and in hydrogel (slice located at −5.87 mm from the center of the RF coil) shown as a function of the experiment time.

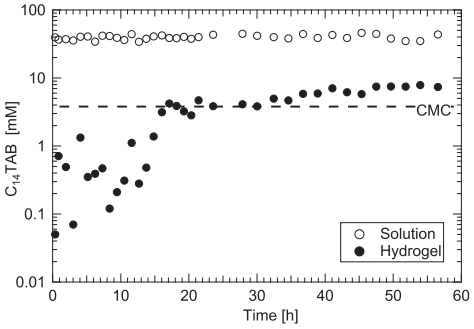

Fig. 8. The C_{14}TAB concentration in solution (average value obtained from three positions located within the Ω_1 slice) and in hydrogel (average value obtained from three positions located within the Ω_2 slice) shown as a function of the experiment time.

At the end of the experiment, the estimated hydrodynamic radius of the micelle both in the solution and in the hydrogel was 3.0 ± 0.2 nm, which is around 4 times smaller than the initial hydrogel mean mesh size. An independent self-diffusion study of the C_{14}TAB in solution as a function of concentration shown in Fig. 9 is in a close agreement with the D_s^{sln} values (for experimental details, please see ESI) proving the validity of the SSD measurements. The values of D_s^{gel} for concentrations lower than CMC are similar to those obtained in solutions confirming that the monomer diffusion in the polymer network is unrestricted, and indicating that there are no significant interactions with the hydrogel. However, after reaching CMC in the hydrogel, D_s^{gel} values are 2–4 times lower than those in the solution for the same C_{14}TAB concentrations indicating that the mobility of the surfactant micelles is hindered due to the obstruction from the polymer network. Moreover, the presence of the hydrogel enhances the interactions between micelles comparable to those in a solution with effectively higher surfactant concentrations [35]. As hydrophobic drugs will be entrapped in the lipophilic core of the surfactant micelles, the diffusion of such drugs will be equal to the diffusion of the micelle and thus equally hindered by the polymer network.

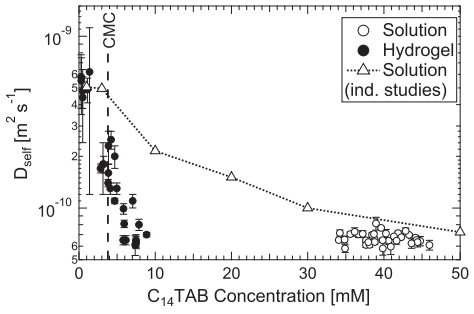

Fig. 9. The self-diffusion coefficient of the surfactant in solution (slice located at +5.87 mm from the center of the RF coil) and in gel (slice located at −5.87 mm from the center of the RF coil) shown as a function of the surfactant concentration. The D_s^{sln} values from independent diffusion studies are shown for comparison (empty triangles). The dotted line is drawn to guide the eye.

The combination of 1D CSI and SSD into one experimental protocol enables a detailed comparison of mutual and self-diffusion processes in hydrogel systems. For our experimental series of surfactant diffusion into the hydrogel, the final value of $\frac{D_s^{gel}}{D_m^{ger}}$ was around 0.8. This result suggests that the time and space sampled during SSD experiments are sufficient to adequately describe the mutual diffusion of the investigated system. As shown above, the localized self-diffusion measurements provide a more detailed picture of the release process than the 1D CSI alone, allowing the identification of both surfactant forms (monomers or micelles) as well as a description of their interactions within the polymer network.

In addition to quantitative screening of drug delivery systems, the presented NMR protocol may be implemented in studies of concentration dependent structures on the interfaces between two immiscible liquids for application in improved oil recovery [36], liquid-liquid extraction [37], monitoring the formation and stability of emulsions [38], and dissolution kinetics [37]. Our experimental approach enables monitoring of both swelling and solute diffusion which can be used to analyze homogeneity of alignment media such as lyotropic liquid crystalline and stretched polymer gels [39,30]. Combined 1D CSI and SSD NMR experiment can be used to perform NMR titrations and *in situ* monitoring of the chemical reactions through providing information about mechanisms as well as stoichiometry of complexes and products [40,41].

5. Conclusion

The swelling and molecular transport in the hydrogel-surfactant system formulations designed for controlled drug release in water are highly complex processes. 1D CSI NMR and PFG-NMR are complementary techniques for studies of these processes because of the differences in length and time scales. We have demonstrated that the combination of the 1D CSI NMR and SSD NMR methods provides detailed information on the diffusion processes as well as on the structure of the surfactant in the non-equilibrium hydrogel-based system. Important applications in areas such as drug delivery are strongly affected by rates of micellar diffusion in polymeric gels, which are determined by the hydrodynamic and electrostatic micelle-micelle and micelle-gel interactions, as well as the thermodynamic relations that govern micelle formation. When applied to drug delivery systems, the experimental protocol presented in this paper will give a detailed description of the local dynamic processes, as it gives a unique opportunity to follow the development of the local transport processes during drug release. Compared with previously reported approaches to study self- and mutual diffusion processes [24,26], our experimental protocol provides information about the structure-dependent diffusional behavior in a simple and straightforward manner. The presented NMR protocol may be

implemented in studies of concentration dependent structures on the interfaces between two immiscible liquids for application in improved oil recovery [36], liquid-liquid extraction [37], monitoring the formation and stability of emulsions [38], and dissolution kinetics [37]. In future research, we will study the diffusional behavior of liposomes incorporated in biopolymer-based hydrogel system.

Appendix A. Supplementary material

Supplementary data associated with this article can be found, in the online version, at https://doi.org/10.1016/j.jcis.2018.08.112.

References

[1] Y. Kapoor, A. Chauhan, J. Colloid Interface Sci. 322 (2008) 624–633, https://doi.org/10.1016/j.jcis.2008.02.028.
[2] M. Pekař, Front. Mater. 1 (2015), https://doi.org/10.3389/fmats.2014.00035.
[3] D. Schmaljohann, Adv. Drug Delivery Rev. 58 (2006) 1655–1670, https://doi.org/10.1016/j.addr.2006.09.020.
[4] J. Hu, S. Zheng, X. Xu, J. Polym. Res. 19 (2012) 9988, https://doi.org/10.1007/s10965-012-9988-0.
[5] J. Zhang, L.-Y. Chu, Y.-K. Li, Y.M. Lee, Polymer 48 (2007) 1718–1728, https://doi.org/10.1016/j.polymer.2007.01.055.
[6] A. Burmistrova, M. Richter, C. Uzum, R.v. Klitzing, Colloid Polym. Sci. 289 (2011) 613–624, https://doi.org/10.1007/s00396-011-2383-2.
[7] T. Si, Y. Wang, W. Wei, P. Lv, G. Ma, Z. Su, React. Funct. Polym. 71 (2011) 728–735, https://doi.org/10.1016/j.reactfunctpolym.2011.04.003.
[8] R. Elashnikov, M. Radocha, S. Rimpelova, V. Svorcik, O. Lyutakov, RSC Adv. 5 (2015) 86825–86831, https://doi.org/10.1039/C5RA13972D.
[9] M.J. Rosen, J.T. Kunjappu, Characteristic Features of Surfactants, Wiley Online Library, 2012.
[10] L. Casal-Dujat, P.C. Griffiths, C. Rodriguez-Abreu, C. Solans, S. Rogers, L. Perez-Garcia, J. Mater. Chem. B 1 (2013) 4963–4971, https://doi.org/10.1039/C3TB20289E.
[11] M. Paulsson, K. Edsman, Pharm. Res. 18 (2001) 1586–1592, https://doi.org/10.1023/A:1013086632302.
[12] B. Amsden, Macromolecules 31 (1998) 8382–8395, https://doi.org/10.1021/ma980765f.
[13] R.J. Bearman, J. Phys. Chem. 65 (1961) 1961–1968, https://doi.org/10.1021/j100828a012.
[14] S. Matsukawa, H. Yasunaga, C. Zhao, S. Kuroki, H. Kurosu, I. Ando, Prog. Polym. Sci. 24 (1999) 995–1044, https://doi.org/10.1016/S0079-6700(99)00022-2.
[15] N. Fatin-Rouge, K.J. Wilkinson, J. Buffle, J. Phys. Chem. B 110 (2006) 20133–20142, https://doi.org/10.1021/jp060362e.
[16] M.D. Burke, J.O. Park, M. Srinivasarao, S.A. Khan, Macromolecules 33 (2000) 7500–7507, https://doi.org/10.1021/ma000786l.
[17] J. Crank, The Mathematics of Diffusion, Oxford University Press, 1979.
[18] E.L. Cussler, Diffusion: Mass Transfer in Fluid Systems, second ed., Cambridge University Press, 1997.
[19] V.F. Felicetta, A.E. Markham, Q.P. Peniston, J.L. McCarthy, J. Am. Chem. Soc. 71 (1949) 2879–2885, https://doi.org/10.1021/ja01176a089.
[20] G.D.J. Phillies, G.B. Benedek, N.A. Mazer, J. Chem. Phys. 65 (1976) 1883–1892, https://doi.org/10.1063/1.433282.
[21] W.J. Musnicki, N.W. Lloyd, R.J. Phillips, S.R. Dungan, J. Colloid Interface Sci. 356 (2011) 165–175, https://doi.org/10.1016/j.jcis.2010.12.067.
[22] B.J. Balcom, A.E. Fischer, T.A. Carpenter, L.D. Hall, J. Am. Chem. Soc. 115 (1993) 3300–3305, https://doi.org/10.1021/ja00061a031.
[23] J. Labille, N. Fatin-Rouge, J. Buffle, Langmuir 23 (2007) 2083–2090, https://doi.org/10.1021/la0611155.
[24] M.-A. Gagnon, M. Lafleur, J. Phys. Chem. B 113 (2009) 9084–9091, https://doi.org/10.1021/jp811105p.
[25] T.R. Brown, B.M. Kincaid, K. Ugurbil, Proc. Natl. Acad. Sci. USA 79 (1982) 3523–3526, https://doi.org/10.1073/pnas.79.11.3523.
[26] S. Kwak, M.T.P. Viet, M. Lafleur, J. Magn. Reson. 162 (2003) 198–205, https://doi.org/10.1016/s1090-7807(03)00047-8.
[27] A. Salvati, I. Lynch, C. Malmborg, D. Topgaard, J. Colloid Interface Sci. 308 (2007) 542–550, https://doi.org/10.1016/j.jcis.2006.11.035.
[28] P. Knöös, D. Topgaard, M. Wahlgren, S. Ulvenlund, L. Piculell, Langmuir 29 (2013) 13898–13908, https://doi.org/10.1021/la4024458.
[29] P. Knöös, M. Wahlgren, D. Topgaard, S. Ulvenlund, L. Piculell, J. Phys. Chem. B 118 (2014) 9757–9767, https://doi.org/10.1021/jp501288u.
[30] A.-C. Pöppler, S. Frischkorn, D. Stalke, M. John, ChemPhysChem 14 (2013) 3103–3107, https://doi.org/10.1002/cphc.201300609.
[31] K. Zick, Diffusion, NMR User Manual, fourth ed., Bruker Corporation, 2016.
[32] C.C. Ruiz, Colloid Polym. Sci. 277 (1999) 701–707, https://doi.org/10.1007/s003960050443.
[33] J.T. Edward, J. Chem. Educ. 47 (1970) 261, https://doi.org/10.1021/ed047p261.
[34] J. Kestin, N. Imaishi, S. Nott, J. Nieuwoudt, J. Sengers, Phys. A 134 (1985) 38–58, https://doi.org/10.1016/0378-4371(85)90155-4.
[35] D.D. Kong, T.F. Kosar, S.R. Dungan, R.J. Phillips, AIChE J. 43 (1997) 25–32.
[36] L.S. de Lara, M.F. Michelon, C.R. Miranda, J. Phys. Chem. B 116 (2012) 14667–14676, https://doi.org/10.1021/jp310172j.
[37] C. Mantel, P.-A. Bayle, S. Hediger, C. Berthon, M. Bardet, Magn. Reson. Chem. (2010) n/a–n/a, https://doi.org/10.1002/mrc.2628.
[38] M.-T. You, Z.-L. Wei, J. Yang, X.-H. Cui, Z. Chen, Chin. Phys. B 27 (2018) 028201, https://doi.org/10.1088/1674-1056/27/2/028201.
[39] P. Trigo-Mourio, C. Merle, M.R.M. Koos, B. Luy, R.R. Gil, Chem. Eur. J. 19 (2013) 7013–7019, https://doi.org/10.1002/chem.201300254.
[40] Y. Mitrev, S. Simova, D. Jeannerat, Chem. Commun. 52 (2016) 5418–5420, https://doi.org/10.1039/c6cc01853j.
[41] T. Niklas, D. Stalke, M. John, Chem. Commun. 51 (2015) 1275–1277, https://doi.org/10.1039/C4CC08329F.

Supporting Information for

Investigating Structure-dependent Diffusion in Hydrogels Using Spatially Resolved NMR Spectroscopy

Malgorzata Anna Wisniewska*, John Georg Seland

Department of Chemistry, University of Bergen, Bergen 5007, Norway

1. The hydrogel mesh size determination

The average mesh size of the pNIPAM hydrogel was determined from the Flory's theory. The mesh size of a swollen hydrogel (ξ^{sw}) is dependent on the root-mean-square end-to-end distance of the polymer subchain between two crosslinking points in the unperturbed state ($\sqrt{r_0^2}$):

$$\xi^{sw} = \nu_{2s}^{-\frac{1}{3}} \sqrt{r_0^2}, \tag{S1}$$

where ν_{2s} is the volume fraction of the polymer, which equals the reciprocal value of the volumetric swelling degree (Q_v^{-1}). For calculating $\sqrt{r_0^2}$, the following expression is used:

$$\sqrt{r_0^2} = l(\frac{2M_c}{M_0})^{\frac{1}{2}} C_N^{\frac{1}{2}}, \tag{S2}$$

where l is the length of a C-C bond (l = 0.154 nm), M_c is the molar mass of the subchain between two crosslinking points, M_0 is the molar mass of the monomer (M_0 = 113.16 $gmol^{-1}$), and C_N is the Flory's characteristic ratio, which is a measure of the extension of the polymer chain in a disordered condition (For NIPAM C_N = 11.7 [1]). Assuming a statistical copolymerization in the synthesis, the molar mass of the subchain between two crosslinking points (M_c) is given by the average molar mass of monomers (M_0) and the degree of crosslinking (d_c) as

$$M_c = \frac{1}{2} M_0 d_c^{-1}, \tag{S3}$$

and

$$d_c = \frac{n_{DAT}}{n_{DAT} + n_{NIPAM}}, \tag{S4}$$

*Corresponding author

where n_{DAT} and n_{NIPAM} are the number of moles of DAT and NIPAM, respectively. The value of the volumetric swelling ratio (Q_v) can be obtained by measuring the increase of the weight of the hydrogel during the swelling process in the following manner:

$$Q_v^{-1} = \frac{\frac{1}{\rho_{pol}}}{\frac{Q_m}{\rho_{solv}} + \frac{1}{\rho_{pol}}}, \tag{S5}$$

where Q_m is the mass swelling ratio, and ρ_{solv} and ρ_{pol} are the densities of the solvent and the hydrogel, respectively. For hydrogel swollen in water at 298 K, ρ_{solv} is 1.0 gmL^{-1}, and ρ_{pol} is $1.1gmL^{-1}$. The mass swelling ratio (Q_m) of the hydrogels is calculated based on:

$$Q_m = \frac{W_s}{W_d}, \tag{S6}$$

where Ws is the weight of the swollen hydrogel and Wd is the weight of the dry hydrogel.

Based on eqs.(S1-S6), the mesh size of the hydrogel can be obtained by determining the swelling ratio (Q_m) of the hydrogel.

Table S1: The values for the number of moles of DAT,n_{DAT} and NIPAM,n_{NIPAM}, and the mass swelling ratio,Q_m used for the mesh size calculation

parameter	value
n_{DAT} (mol)	0.129×10^{-3}
n_{NIPAM} (mol)	3.509×10^{-3}
Q_m (a.u.)	50.8

2. Mutual diffusion coefficient (D_m) determination

3. C_{14}TAB self-diffusion studies in solutions

The independent C_{14}TAB self-diffusion studies in solutions with varying concentration were performed on a Bruker AVANCE DRX 600 MHz NMR spectrometer equipped with a a triple resonance cryoprobe head with gradient unit. The measurements were performed at 298 (± 1) K using a stimulated echo sequence with the longitudinal eddy current delay and bipolar sine shaped gradient pulses, and two spoiling gradients (ledbpgp2s). The signal intensity was recorded as a function of gradient strength (g) at 16 different values between 0.68 and 32.35 G/cm. The maximum values of g (gmax) were chosen to obtain almost complete attenuation (>90%) of the C_{14}TAB resonances. The gradient duration time (δ) and the diffusion time (Δ) were 1.5-2 ms and 100-200 ms, respectively.

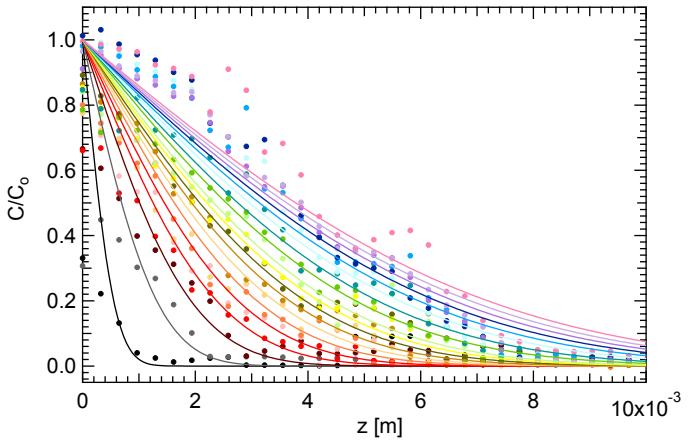

Figure S1: Time-development of the normalized concentration profiles of C_{14}TAB in the hydrogel fitted with Equation 2. The resulting D_m is 7.7 $\pm 0.5 \times 10^{-11} m^2 s^{-1}$.

References

[1] T. Trongsatitkul, B. M. Budhlall, Microgels or microcapsules? role of morphology on the release kinetics of thermoresponsive PNIPAm-co-PEGMa hydrogels, Polym. Chem. 4 (2013) 1502–1516.

Graphic design: Communication Division, UiB / Print: Skipnes Kommunikasjon AS

uib.no

ISBN: 9788230857656 (print)
9788230840320 (PDF)